A Scintillation-Detection-Type Non-Destructive 2-D Beam Profile Monitor Using a Gas Sheet

A dissertation submitted in partial fulfillment of the requirements

for the degree of PhD in Engineering

Ippei Yamada

Graduate School of Science and Engineering

Doshisha University

November 2021

Abstract

This dissertation describes establishment of a non-destructive beam spatial profile diagnostic method for a high-intensity, low-energy ion beam. A monitor injecting a locally concentrated gas like a thin sheet has been developed. The gas sheet injected into a beam line produces photons by beam-gas interaction. The spatial distribution of the produced photons being in proportion to the beam spatial profile is detected as a two-dimensional image with a CCD camera coupled to an image intensifier. The 2-D beam profile can be obtained from the luminous intensity spatial distribution of the captured image. However, the luminous intensity distribution does not directly correspond to the beam profile because the gas density distribution and the sensitivity distribution of the photon detector converts the beam profile signal into the image. A proper analysis method to reconstruct the beam profile from the image by solving the conversion is indispensable to establish the profile diagnostic method based on beam-gas interaction. The influence of the gas sheet injection on the beam should be also clarified to evaluate the non-destructiveness of the developed monitor.

Formation of the gas sheet is based on vacuum engineering which is characterized by the collisionless approximation and the cosine law for reflection on a wall. To design a gas sheet generator, a gas flow simulation code based on the Boltzmann equation optimized for molecular flow calculation was developed. On the basis of the simulation, the gas sheet generator was designed as a 100 mm-long, 50 mm-wide and 0.1 mm-thin rectangular conduit. The vacuum pumps to evacuate the injected gas were chosen by a calculation of the gas density distribution on the beam line. In addition, a cover chamber surrounding the gas sheet generator was designed to cut the unnecessary components of the gas sheet distribution in advance. The cover chamber has a 50 mm$\times$0.5 mm rectangular slit and a pump to evacuate the molecules reflected on the slit plate. The gas flow simulation estimated that the cover chamber reduces the gas flux injected into the beam line chamber by 72%. The characteristics of the gas pressure, the gas flux and the conductance of the developed gas sheet monitor system was experimentally measured. The gas flux introduced into the beam line chamber was reduced by 77% with the cover chamber, and the result agreed with the simulation. The conductance of the gas sheet generator which is constant in molecular flow region largely changed with the generator inlet gas pressure. The gas density spatial distribution became broad against increase of the generator inlet pressure. From these measurement results,

it was clarified that intermolecular collisions are not negligible in the main pressure range where the generator is utilized as the gas sheet monitor and the conduit length determines the fully-collisionless pressure region.

To quantitatively reconstruct a beam profile from a captured 2-D image, the principle of beam profile measurement with the gas sheet monitor was formulated. The conversion process of a beam profile signal into an image includes the three kinds of the point-spread effects due to the motion of excited molecules, the out-of-focus effect of the optical lens, and the spatial resolution reduction in the image intensifier. These effects can be described by change of coordinate with integrals. The correlation between the beam profile signal and the luminous intensity distribution of the obtained image was devised as a triple-integral equation with a response function describing the gas sheet monitor; the profile reconstruction is realized by solving the integral equation with the measured response function. The response function measurement method was devised based on the integral equation, and the response function was measured by injecting a 3 keV thin electron beam into the gas sheet monitor.

The effectivenesses of the developed gas sheet monitor and the profile reconstruction method were demonstrated through the 3 MeV, 60 mA H^- beam profile measurement at the J-PARC RFQ test stand. The beam-induced photon signal was successfully obtained with the wide range of the gas-sheet-generator inlet pressure from 0.1 Pa to 1 kPa. The 1 kPa injection realized the beam profile measurement with only 1 beam pulse of 50 μs corresponding to 1.7×10^{13} H^- particles. The 0.1 Pa injection realized the highly non-invasive measurement at the beam line pressure of 1.4×10^{-6} Pa against the base pressure of 1.2×10^{-6} Pa. Two kinds of the methods to reconstruct the beam profile from the obtained 2-D image were devised: the simplified fast method for a beam operation and the exact method for a beam dynamics study. The simplified method assumes the response function as the ideal gas sheet described as a delta function, and the integral equation can be simplified as just the change of coordinate. An analytical evaluation of the error in the reconstructed profile due to ignoring the response function indicated that the reconstructed profile is 24% broader than the true beam profile in the vertical direction. The reconstructed J-PARC H^- beam profile in the vertical direction was 20% broader than the one measured by a wire-scanner monitor which is an ordinary profile monitor. On the other hand, the exact method took the measured response function into account and solving the integral equation to reconstruct the beam profile. In this exact reconstruction method, the accuracy of the response function measurement affects the reconstructed profile. The estimation based on assumptions of analytical

functions indicated that a thick electron beam for the response function measurement makes the reconstructed profile thin as compared with the true one. The reconstructed 2-D profile of the J-PARC H^- beam was thinner than the profile measured with the wire-scanner monitor as expected. Since the error is caused by utilizing the wrong point-spread effects in the reconstruction analysis, the approximation ignoring the point-spread effects was performed. The approximation improved the error and reconstructed the profile agreeing well with the one obtained by the wire-scanner monitor. Thus, it was demonstrated that the two kinds of the quantitative profile reconstruction methods give the beam profile within the range of the possible error. The methods to improve the profile reconstruction accuracy without the approximation by constructing an accurate response function were also proposed.

To evaluate the non-destructiveness of the gas sheet monitor, the electron stripping ratio of the H^- beam and change of the phase space distribution due to gas sheet injection were measured. The electron stripping ratio defined as a beam current reduction linearly increased against a rise in the gas sheet flux. This result was consistent with the theoretical estimation based on the electron stripping cross section within the factor of 3. As for change of the phase space distribution, the gas sheet injection decreased the beam emittance. The emittance reduction means an improvement of the beam quality and was explained by the space-charge neutralization effect. Thus, the gas sheet injection does not always have an adverse influence on the beam, and a new advantage of the photon-detection-based profile measurement was found.

Finally, this dissertation presents an application of the gas sheet monitor. The time evolution of the beam profile was measured to investigate the beam-loading effect which is the significant problem making the beam unstable in a high-intensity particle accelerator. It was clarified that the gas sheet monitor can measure the time evolution of the beam profile in a beam pulse and the beam-loading effect affects the beam profile and makes the beam profile unstable.

Contents

List of Figures

List of Tables

Chapter 1

Introduction

A high-energy particle accelerator recently tends to be high intensity or high luminosity to realize a high accurate particle/nuclear experiment. One of the most critical problems limiting the beam intensity is a beam loss causing an activation of nuclear radiation of the accelerator systems. Since the allowable amount of the beam loss is constant independently of the beam intensity, a stable operation is required, particularly in a high-intensity accelerator. To minimize the beam loss by controlling the accelerator components, monitoring the beam conditions, such as the beam center position, the beam energy, the beam spatial distribution, the beam emittance, and the beam current, is indispensable. A monitor measuring the amount of the beam loss is also important to safely operate the accelerator. Diagnostic of a high-intensity beam parameter requires a non-destructive or non-invasive type of monitor because a destructive one causes a beam loss and an activation of itself by interaction with the beam. Non-destructive monitors for the beam position, the beam energy, the beam current, and the beam loss have been utilized in many accelerators [1–5]. However, as for monitors measuring the beam spatial distribution and the beam emittance, destructive types are still utilized [6–9]. In the Japan Proton Accelerator Research Complex (J-PARC), the wire-scanning type monitor is ordinary utilized to measure the one-dimensional beam distributions and the beam emittanaces [6]. Since the wire breaks due to the energy deposition from the beam, the beam pulse length must be shortened compared with the standard length, and the beam distribution of the maximum power operation has not been measured. To solve this issue, a non-destructive beam profile monitor based on beam-gas interaction measuring a beam spatial distribution in a transverse plane perpendicular to the beam axis has been being developed in many institutes [10–25]. The monitor detects a density spatial distribution of ions, electrons or photons produced by beam-gas interaction, and

the beam profile is reconstructed from the spatial distribution of the produced particles. The monitor can be classified by 2×2 types: residual gas or gas injection and charged-particle detection or photon detection.

The residual gas type of monitor is more non-destructive than the gas injection type, and its system structure is more simple. The monitor is suitable for use in a ring accelerator because the beam flight length is extremely long in a ring accelerator and the beam becomes easily unstable if an extra gas exists. Charged-particle detection is efficient in the signal intensity as compared with photon detection because the electric guide field enables collection of the most of the produced particles. An important issue of the charged-particle-detection monitor is the error in the measured beam profile due to different reasons: a wakefield of the beam, Coulomb interaction among the produced particles, and inhomogeneity of the electric field for collecting the produced particles [10]. Hochadel *et al.* [11] and Harada *et al.* [12] developed the multi-electrode system for producing a uniform electric field to avoid the distortion of the measured beam profile. Vilsmeier *et al.* [10] and Bartkoski *et al.* [13] utilized the electrons with a guiding magnetic field.

On the other hand, photon detection solves the issue of the profile distortion caused by the ambient electromagnetic field while it sacrifices the signal intensity [14–16]. As compared with the efficient collection of the charged particles, optical lenses can gather only 10^{-2}-10^{-4} part of the total produced photons due to the solid-angle limitation. To increase the signal intensity, monitors injecting pencil- or sheet-shaped gas have been developed [17–20]. Zhang *et al.* [17, 18] and Tzoganis *et al.* [19] obtained two-dimensional electron-beam-induced signal using a supersonic sheet-shaped gas jet in the Cockcroft Institute. Their gas jet is formed by an adiabatic expansion around atmospheric pressure based on fluid dynamics. Multi-step pumping is required to form the pencil- or sheet-shaped gas jet and to decrease the gas pressure in the chambers from atmospheric pressure to ultra-high vacuum. The gas flow simulation model is complicated due to such a wide pressure range. Their gas-jet monitor consists of six chambers including three pre-pumping chambers. The gas density of the jet reached 3×10^{-5} Pa equivalent at 0.5 MPa injection. In Heavy Ion Medical Accelerator (HIMAC), Hashimoto *et al.* [20, 21] developed an oxygen-gas jet monitor consisting of five chambers including three pre-pumping chambers and successfully detected a signal induced by HIMAC beam. They realized the gas sheet jet of 1×10^{-4} Pa at 0.6 MPa injection with the idea of the focusing magnet for the oxygen gas sheet. In J-PARC, Ogiwara produced a gas sheet based on rarefied gas dynamics [22, 23]. The advantage

of his gas sheet is that the monitor system consisting of his gas sheet generator tends to be simple because the generator inlet gas pressure is smaller than the one of the gas jet monitors. The gas sheet density can be easily controlled in a wide range because the gas density spatial distribution does not depend on the difference in the upstream and downstream pressures of the generator while the gas jet distribution depends on the difference.

As described above, while there are a lot of previous studies for the non-destructive profile monitor development and the demonstration of its performance, a method to quantitatively reconstruct the beam profile from the obtained data is not well established. The obtained data do not directly correspond to the beam profile because the data are affected by the gas-density spatial distribution of not only the sheet gas but also the background gas and the sensitivity spatial distribution of the photon detector system. Therefore, a proper analysis method to reconstruct the beam profile by inversely solving the conversion from the profile to the obtained data is indispensable to utilize the gas-injection-type monitors. Another important issue to utilize the gas-injection-type monitor is an influence on a beam due to gas injection into a beam line. While the gas-injection-type monitor has advantages in signal intensity and two-dimensional measurement as compared with a residual-gas-type monitor, the gas injection may affect the beam condition by scattering of the beam with gas or electromagnetic interaction between the beam and the produced plasma. However, evaluation of the gas injection effect on a beam is also insufficient.

In this study, a gas sheet beam profile monitor shown in Fig. 1.1 was developed to establish a whole non-destructive beam profile diagnostic method by solving the above problems. The gas sheet monitor injects a sheet-shaped gas, and the produced photons are detected as a two-dimensional image. The reason detecting the produced photons is that the photon detection is more non-destructive because no electrodes and no magnets are needed for constructing the monitor system and the profile reconstruction for photon detection is easier because the electromagnetic potential has smaller influence on the photon signal conversion. The profile reconstruction method was proposed by formulating the process of the signal conversion. To demonstrate the effectivenesses of the developed monitor and the profile reconstruction method, the monitor was installed in the J-PARC test stand. To evaluate the non-destructiveness of the gas sheet monitor, a beam current reduction and change of the phase space distribution of the beam due to the gas sheet injection were investigated.

This dissertation discusses the following 9 contents to establish the non-destructive

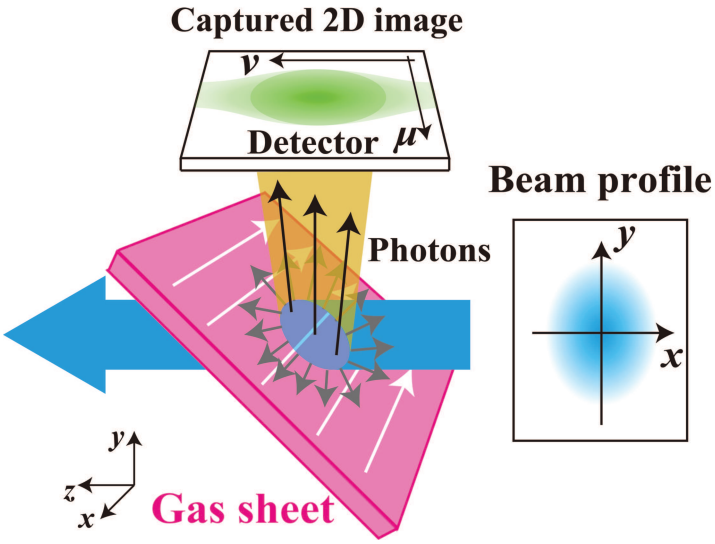

Figure 1.1: A schematic diagram of a gas sheet beam profile monitor. The density distribution of the injected gas is concentrated like a thin sheet to enable measurements of the transverse beam profile in two dimensions without significant increase of the beam line gas pressure.

profile diagnostic method. Chapter 2 describes the principles to form a gas sheet and to measure a beam profile with the gas sheet monitor. Chapter 3 presents the design of the gas sheet monitor in particular the gas sheet generator based on a gas flow simulation. Chapter 4 describes the evaluation of the developed gas sheet monitor for beam profile reconstruction. Chapter 5 provides the experimental result of the high-intensity H^- beam profile measurement at the J-PARC Linac based test stand. Chapter 6 gives the profile reconstruction procedure and the reconstruction result with the estimation of the error in the reconstructed profile. In Chapter 7 the destructiveness of the gas sheet monitor is discussed based on a beam current reduction and change of the phase space distribution of the beam. In Chapter 8 the time evolution measurement of a beam profile is presented as an applied profile measurement using the gas sheet monitor. Finally, the conclusion of this study is provided in Chapter 9.

References

[1] H. J. Kwon, H. S. Kim, K. T. Seol, J. Y. Ryu, J. H. Jang, and Y. S. Cho, "Design and fabrication of the beam position monitor for the pefp linac", Nuclear Engineering and Technology **45**, 523–528 (2013).

[2] M. Wendt, *Bpm systems: a brief introduction to beam position monitoring*, 2020.

[3] A. Dhavale, H. Tyagi, S. Acharya, R. Tiwari, H. Sarukte, U. Yerge, D. Bhattacharjee, and K. Dixit, "Development of fast current transformer (FCT) for beam diagnostics", India: Raja Ramanna Centre for Advanced Technology (2018).

[4] K. Yamamoto, "Signal response of the beam loss monitor as a function of the lost beam energy", in *Proceedings of the International Beam Instrumentation Conference IBIC2015*, (Melbourne, Australia, 2015), MOPB021.

[5] K. Satou, T. Toyama, N. Kamikubota, S. Yamada, and S. Yoshida, "Development of wide dynamic range beam loss monitor system for J-PARC main ring", Journal of Physics: Conference Series **874**, 012087 (2017).

[6] A. Miura, K. Hasegawa, T. Miyao, T. Maruta, Y. Liu, and K. Horioka, "Beam profile monitor for intense, negative hydrogen-ion beams in the J-PARC Linac", Journal of the Korean Physical Society **69**, 1005–1013 (2016).

[7] Q. Z. Xing, L. Du, X. L. Guan, C. X. Tang, M. W. Wang, X. W. Wang, and S. X. Zheng, "Transverse profile tomography of a high current proton beam with a multi-wire scanner", Phys. Rev. Accel. Beams **21**, 072801 (2018).

[8] L. Yu, J. Zhao, Y. Sui, and D. Zhu, "Design and application of double-slit emittance meter for c-ads proton beams", in *Proceedings of the International Particle Accelerator Conference IPAC2016*, (Busan, Korea, 2016), MOPMB034.

[9] Y. Morita, M. Fukuda, T. Yorita, H. Kanda, K. Hatanaka, Y. Yasuda, M. Nakao, K. Kamakura, S. Hara, H. W. Koay, K. Takeda, T. Hara, and K. Omoto, "Developments of real-time emittance monitors", Review of Scientific Instruments **91**, 043303 (2020).

[10] D. Vilsmeier, M. Sapinski, and R. Singh, "Space-charge distortion of transverse profiles measured by electron-based ionization profile monitors and correction methods", Phys. Rev. Accel. Beams **22**, 052801 (2019).

[11] B. Hochadel, F. Albrecht, M. Grieser, D. Habs, D. Schwalm, E. Szmola, and A. Wolf, "A residual-gas ionization beam profile monitor for the Heidelberg Test Storage Ring TSR", Nucl. Instrum. Meth. Phys. Res. A **343**, 401–414 (1994).

[12] H. Harada, K. Yamamoto, and M. Yoshimoto, in *Proceedings of the International Particle Accelerator Conference 2012*, (New Orleans, Louisiana, USA, 2012), MOPPR029.

[13] D. A. Bartkoski, C. Deibele, and Y.Polsky, "Design of an ionization profile monitor for SNS accumulator ring", Nucl. Instrum. Meth. Phys. Res., A **767**, 379 (2014).

[14] T. Tsang, D. Gassner, and M. Minty, "Residual gas fluorescence monitor for relativistic heavy ions at RHIC", Phys. Rev. Accel. Beams **16**, 102802 (2013).

[15] F. Becker, C. Andre, P. Forck, and D. H. H. Hoffmann, in *8th European Workshop on Beam Diagnostics and Instrumentation for Particle Accelerators(DIAPAC)*, (Venice, Italy, 2017), MOO3A02.

[16] C. Andre, P. Forck, R. Haseitl, A. Reiter, R. Singh, and B. Walasek-Hoehne, in *Proceedings of 3rd the International Beam Instrumentation Conference 2014*, (Monterey, CA, USA, 2014), TUPD05.

[17] H. D. Zhang, E. Martin, V. Tzoganis, C. P. Welsch, N. S. Chritin, E. B. Diaz, O. R. Jones, G. Schneider, R. Veness, P. Forck, and S. Udrea, in *Proceedings of the International Particle Accelerator Conference 2017*, (Copenhagen, Denmark, 2017), MOPAB139.

[18] H. D. Zhang, A. Salehilashkajani, C. P. Welsch, M. Ady, J. Glutting, O. R. Jones, T. Marriott-Dodington, S. Mazzoni, A. Rossi, G. Schneider, R. Veness, and P. Forck, "Development of supersonic gas-sheet-based beam profile monitors", in *Proceedings of the International Particle Accelerator Conference IPAC2019*, (Melbourne, Australia, 2019), WEPGW096 (2019).

[19] V. Tzoganis, H. D. Zhang, A. Jeff, and C. P. Welsch, "Design and first operation of a supersonic gas jet based beam profile monitor", Phys. Rev. Accel. Beams **20**, 062801 (2017).

[20] Y. Hashimoto, T. Fujisawa, T. Morimoto, Y. Fujita, T. Honma, S. Muto, K. Noda, Y. Sato, and S. Yamada, "Oxygen gas-sheet beam profile monitor for the synchrotron and storage ring", Nucl. Instrum. Meth. Phys. Res. A **492**, 74–90 (2002).

[21] T. Fujisawa, Y. Hashimoto, T. Morimoto, and Y. Fujita, "Multipole magnets to focus an O_2 sheet beam for a nondestructive beam-profile monitor", Nucl. Instrum. Meth. Phys. Res. A **506**, 50 (2003).

[22] N. Ogiwara, in *Proceedings of the International Particle Accelerator Conference IPAC2016*, (Busan, Korea, 2016), WEOBB03.

[23] N. Ogiwara, Y. Hori, I. Yamada, Y. Hikichi, J. Kamiya, and M. Kinsho, in *Proceedings of the International Particle Accelerator Conference IPAC2019*, (Melbourne, Australia, 2019), WEPGW037.

[24] J. Kamiya, N. Ogiwara, A. Miura, M. Kinsho, and Y. Hikichi, "Non-destructive 2-d beam profile monitor using gas sheet in J-PARC LINAC", Journal of Physics: Conf. Series **1067**, 0720006 (2018).

[25] J. Kamiya, K. Okabe, M. Kinsho, K. Moriya, I. Yamada, N. Ogiwara, Y. Hikichi, and K. Wada, "Evaluation of 2-d transverse beam profile monitor using gas sheet at J-PARC LINAC", Journal of Physics: Conf. Series **1350**, 012149 (2019).

Chapter 2

Principle of Gas Sheet Monitor

2.1 Gas sheet formation

An ensemble of gas molecules follows the Boltzmann equation (or kinetic equation):

$$\frac{\partial}{\partial t}f(\boldsymbol{x},\boldsymbol{v};t)+\boldsymbol{v}\cdot\frac{\partial}{\partial \boldsymbol{x}}f(\boldsymbol{x},\boldsymbol{v};t)+\frac{\boldsymbol{F}}{m}\cdot\frac{\partial}{\partial \boldsymbol{v}}f(\boldsymbol{x},\boldsymbol{v};t)=\left.\frac{\partial f}{\partial t}\right|_{\text{coll}} \tag{2.1}$$

where $\boldsymbol{x},\boldsymbol{v}$ are the position vector and the velocity vector of molecules, t is the time, $f(\boldsymbol{x},\boldsymbol{v};t)$ is the velocity-distribution function, $\boldsymbol{F}$ is force acting on the molecules, m is the molecular mass, and the right-hand-side term describes the time rate of change in distribution function due to intermolecular collisions. Formation of a gas sheet corresponds to eliminating the collision term which causes spread of the velocity-distribution function and shaping the velocity-distribution function, particularly in velocity space. A method to eliminate the collision term and shape the velocity-distribution function depends on the gas flow models which are classified by the range of Knudsen number K_{n} defined as a ratio of the mean-free path length λ of gas molecules to the characteristic length L of the flow channel,

$$K_{\text{n}}=\frac{\lambda}{L}. \tag{2.2}$$

$$\begin{cases} K_{\text{n}}>0.3 & : \text{Molecular flow} \\ 0.01<K_{\text{n}}<0.3 & : \text{Intermediate flow} \\ K_{\text{n}}<0.01 & : \text{Viscous flow} \end{cases} \tag{2.3}$$

Some scientists including Putignano created a gas sheet based on a viscous flow model of fluid dynamics [26]. Molecules injected into a gas jet nozzle over an atmospheric pressure are accelerated and cooled by free expansion. Cooling due to expansion

arranges both of the directions and magnitudes of the molecular velocity vectors, and intermolecular collisions become negligible. Shaping the velocity-distribution function to create a gas sheet can be realized by skimmers placed downstream the nozzle. Zhang *et al.* created a 2 mm-thick 8 mm-wide gas sheet jet using three skimmers having a rectangular aperture [18]. As another way to create a sheet shape and increase the gas density, Hashimoto *et al.* utilized focusing magnets with oxygen gas; they introduced an external force $\boldsymbol{F}$ in Eq. (2.1) [20].

In this study, a gas sheet is formed based on vacuum engineering or rarefied gas dynamics with the molecular flow model. In the molecular flow region, intermolecular collisions are negligible because mean-free path of gas molecules is enough longer than the characteristic length of a chamber. Therefore, the collision term in Eq. (2.1) can be set to zero. Any external or internal forces are not utilized to create the gas sheet in this study, and the force term is also set to zero. Equation (2.1) becomes the following simple form:

$$\frac{\partial}{\partial t} f(\boldsymbol{x}, \boldsymbol{v}; t) + \boldsymbol{v} \cdot \frac{\partial}{\partial \boldsymbol{x}} f(\boldsymbol{x}, \boldsymbol{v}; t) = 0. \tag{2.4}$$

Gas molecules in the molecular flow region are subject to Eq. (2.4). Another important factor to characterize the molecular flow is the reflection process on a wall: a boundary condition. When a molecule approaches to a wall, the molecule is adsorbed on the wall surface. After a certain period of time, the molecule is desorbed independently of the incident conditions; the reflection process is considered to be a stochastic process. The reflection (or desorption) angle is not determined isotropically or specularly but assigned by the cosine law. This surface collision process is explained as follows. Even if a volume with an ensemble of gas molecules in a thermal equilibrium is separated into two volumes with a plate as shown in Fig. 2.1a, the molecules in the both volumes are considered to be in the thermal equilibrium as same as the condition without the separation plate. The states of the molecules in the two volumes does not change even if an aperture of the area S is made on the separation plate as shown in Fig. 2.1b. Probability of a molecule passing through the aperture of the area S is described as

$$\frac{S \cos\theta}{4\pi r^2} \tag{2.5}$$

where r is the distance between the aperture and the molecular position and θ is the angle with respect to the normal direction of the aperture. Reflections of the two molecules like in the case of Fig. 2.1a is statistically same as that a molecule exits from the left-hand-side volume through the aperture and another molecule enters from

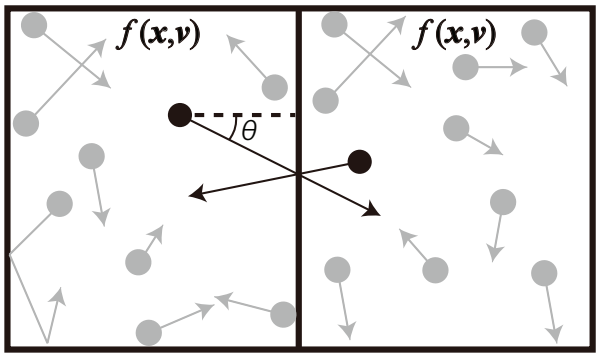

(a)

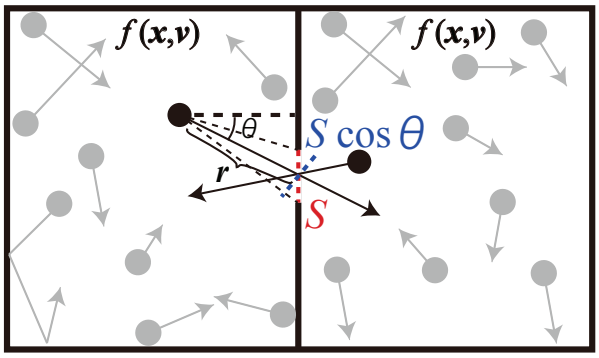

(b)

Figure 2.1: Probability of the reflection angle on a wall is subject to the cosine law. (a) Motion of molecules in two separated volumes does not change (b) when an aperture is made on the plate because the distribution functions must not differ in the same thermal equilibrium; processes of (a) reflection and (b) passing an aperture are statistically same.

the right-hand-side volume into the left-hand-side volume like in the case of Fig. 2.1b because the distribution functions must not differ in the same thermal equilibrium. The probability-distribution function of the reflection angle can be described by the form Eq. (2.5) and is proportional to $\cos\theta$. Therefore, the velocity-distribution function of the molecules passing through the aperture or reflected on a wall is subject to the cosine law.

The velocity-distribution function of the molecules in the left-hand-side volume shown in Fig. 2.2 is defined as $f(\boldsymbol{x}, \boldsymbol{v})$. In a thin half shell of the diameter r with thickness dr whose center is at the aperture center, molecules which can enter the aperture are described as

$$\frac{1}{2}\, 4\pi r^2 \mathrm{d}r\, f(\boldsymbol{x}, \boldsymbol{v})\, \frac{S\cos\theta}{4\pi r^2}. \tag{2.6}$$

The velocity-distribution function of the molecules entering the aperture $f'(\boldsymbol{v})$ during

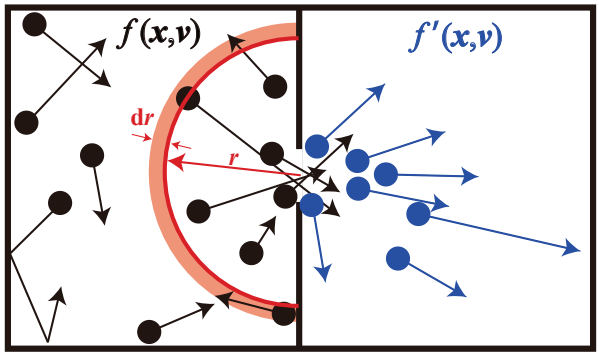

(a)

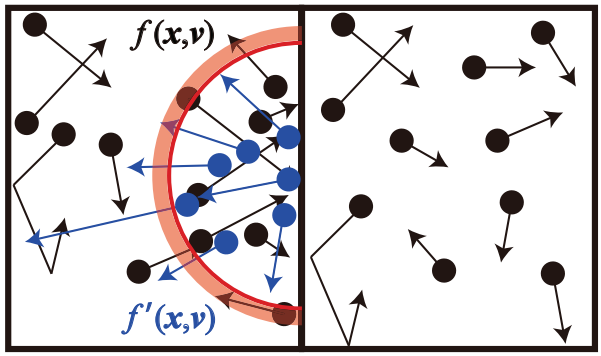

(b)

Figure 2.2: A physical picture of (a) process of passing an aperture and (b) reflection process.

a time Δt can be described by integrating Eq. (2.6) with respect to r:

$$f'(\boldsymbol{v}) \equiv \int_0^{v\Delta t} \frac{1}{2}\, S\, \cos\theta\, f(\boldsymbol{x}, \boldsymbol{v}) \mathrm{d}r \tag{2.7}$$

where $v = \|\boldsymbol{v}\|$. This formula defines the the velocity-distribution function only in the velocity space, and this formula also describes the velocity-distribution function of the reflected molecules on a wall in area S. The velocity-distribution function $f'(\boldsymbol{x}, \boldsymbol{v})$ of the molecules passing the aperture in the position space depends on the distribution of the incident molecules $f(\boldsymbol{x}, \boldsymbol{v})$. On the other hand, for the reflected molecules the velocity-distribution function in the position space is independent of the incident one because the reflection process including the staying time on the surface is stochastic and a huge number of reflections occur constantly, and it should be calculated from the distribution function $f'(\boldsymbol{v})$ and the time Δt. If the velocity-distribution function $f(\boldsymbol{x}, \boldsymbol{v})$ is uniform in the position space, Eq. (2.7) becomes

$$f'(\boldsymbol{v}) = \frac{1}{2}\, S\, v \cos\theta\, f(\boldsymbol{v})\Delta t = \frac{1}{2}\, S\, \boldsymbol{v} \cdot \boldsymbol{n}\, f(\boldsymbol{v})\Delta t \tag{2.8}$$

where $\boldsymbol{n}$ is the normal unit vector of the aperture. In the case that the Maxwell-Boltzmann distribution is considered as the velocity-distribution function constructed by N_{mol} molecules

$$f(\boldsymbol{v}) = N_{\mathrm{mol}} \left(\frac{m}{2\pi k_B T_{th}} \right)^{\frac{3}{2}} \exp\left(-\frac{m\boldsymbol{v}^2}{2k_B T_{th}} \right) \tag{2.9}$$

or

$$f(v) = 4\pi v^2 N_{\mathrm{mol}} \left(\frac{m}{2\pi k_B T_{th}} \right)^{\frac{3}{2}} \exp\left(-\frac{mv^2}{2k_B T_{th}} \right), \tag{2.10}$$

the velocity-distribution function of the molecules reflected on a wall or passing an aperture $f'(\boldsymbol{v})$ can be described as follows with normalizing:

$$f'(\boldsymbol{v}) = \frac{1}{2\pi} N_{\mathrm{mol}} \left(\frac{m}{k_B T_{th}} \right)^{2} \boldsymbol{v} \cdot \boldsymbol{n} \, \exp\left(-\frac{m\boldsymbol{v}^2}{2k_B T_{th}} \right) \tag{2.11}$$

or

$$f'(v) = \frac{1}{2} N_{\mathrm{mol}} \left(\frac{m}{k_B T_{th}} \right)^{2} v^3 \exp\left(-\frac{mv^2}{2k_B T_{th}} \right), \tag{2.12}$$

where k_B is the Boltzmann constant and T_{th} is temperature of the molecules. Thus, motion of molecules in the molecular flow region can be described by the simplified Boltzmann equation Eq. (2.4) with the boundary condition being subject to transform of the velocity-distribution function Eq. (2.7). This fact indicates that shaping the velocity-distribution function to form a gas sheet is realized with slits to extract a part of the velocity-distribution function or a gas conduit to re-distribute the velocity-distribution function. A long gas conduit having a thin cross section shown in Fig. 2.3a is utilized to increase the number of reflections in the thickness direction. When a molecule obtains a large reflection angle which is given with a low probability, the molecule can pass the conduit; the velocity-distribution function of the molecules passing the conduit is shaped by aligning the velocity vectors of the molecules. Even if the long gas conduit is utilized and forms a sheet, the tail part of the velocity-distribution function in the velocity space perpendicular to the normal direction of the conduit exit surface still exists due to the finite length or the finite thickness of the conduit. To extract the core part of the gas sheet, usage of a slit should be considered as shown in Fig. 2.3b.

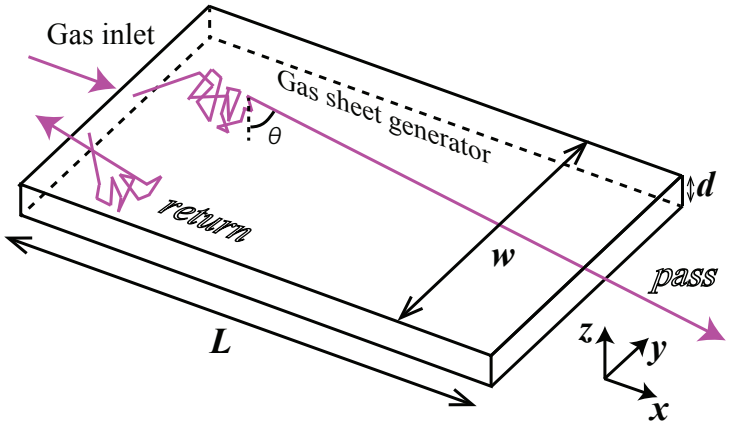

(a)

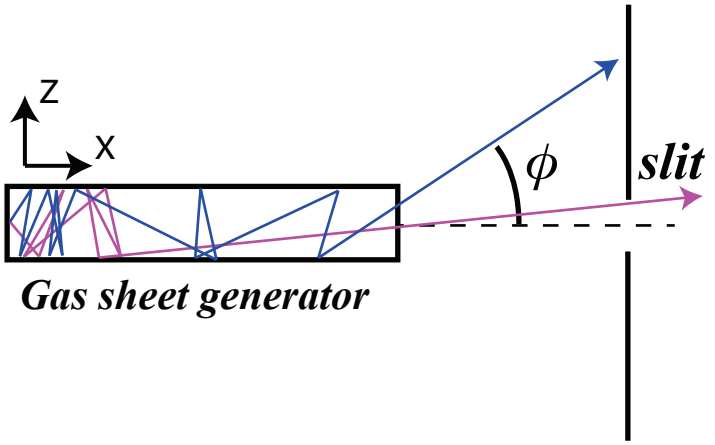

(b)

Figure 2.3: A gas sheet generator is a long gas conduit having a thin cross section.

2.2 Formulation of gas sheet monitor

Figure 2.4 shows the principle of the beam profile measurement with the gas sheet monitor which consists of a gas sheet injected along x axis and a photon detector system facing toward y direction. The photon detector system consists of an optical system, an image intensifier, and a charge-coupled devise (CCD). The figure also shows a beam passing through the gas sheet along z axis. The Cartesian coordinate system is defined against the laboratory frame with time t, and the origin of the spatial coordinate is defined at the center of the interaction point of the beam (axis) and the gas sheet (flow axis). The three-dimensional beam profile is defined as $f(x, y, t; z)$ because the beam in an accelerator is generally bunched; the longitudinal profile is described as the time structure of the beam bunch. The z dependance means change of the 3-D profile due to an internal or external force against the traveling direction. When the beam passes through the gas sheet monitor, the beam excites not only the sheet-gas molecules but also the background gas molecules whose density spatial distributions are defined as $n(x, y, z; t)$ with the photon-emission excitation cross section σ:

$$n^*(x, y, z, t) = \sigma\ n(x, y, z; t)\ f(x, y, t; z) \tag{2.13}$$

where $n^*(x, y, z, t)$ is the spatial density distribution of the excited molecules. The excited molecules move with the thermal velocity in a lifetime of the excited state. If the excited molecules are ions like $N_2{}^+$, electromagnetic potentials induced by the beam particles and the produced ions/electrons also affect the trajectories of the molecules. After the lifetime photons emitted from the excited molecules are focused onto an image intensifier with the optical lens. The image intensifier transforms the photon signal into the electron signal and amplifies the intensity of the signal with a built-in multi-channel plate (MCP) having an amplification-efficiency spatial distribution. The secondary electrons create an image by striking a phospher screen. A CCD camera captures an output image of the image intensifier with the detection-efficiency spatial distribution. In this profile-measurement process, the signal spatial distribution broadens due to three different factors: motion of the excited molecules, out-of-focus effect of the optical system, and spatial resolution reduction in the image intensifier. The distribution spreads can be described by changing the coordinate system as shown in Fig. 2.5. A point ${}^1x_1$ in a ${}^1x$ space spreads and forms a distribution $\mathrm{d}h_2({}^2x)$ in a ${}^2x$ space according to a point-spread function $T({}^2x;{}^1x)$. A function $h_2({}^2x)$ in the ${}^2x$ space constructed by a function $h_1({}^1x)$ in the ${}^1x$ space can be described by integral of $h_1({}^1x)$

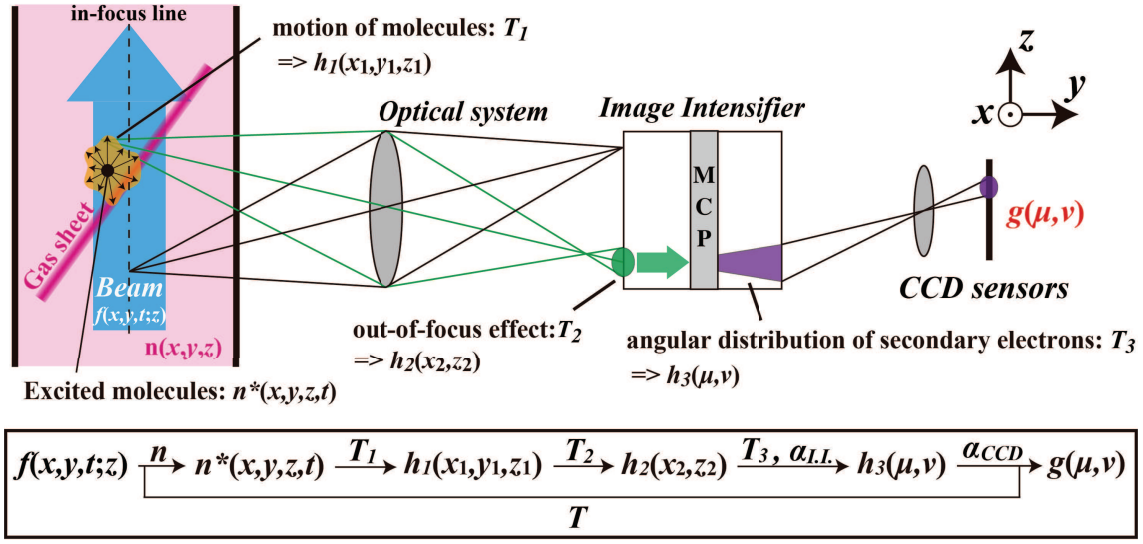

Figure 2.4: The constituents of the response function. The gas sheet flows along x direction and a photon detector system faces toward y direction. The photon detector system consists of a set of optical lenses, an image intensifier, and a CCD camera. The beam profile signal is converted into a 2-D image on the CCD camera by the gas density spatial distribution n, the motion of the excited molecules T_1, the out-of-focus effect of the optical system T_2, the amplification efficiency spatial distribution of the image intensifier $\alpha_{I.I.}$, the resolution reduction due to the image intensifier T_3, and the detection efficiency spatial distribution of the CCD camera α_{CCD}.

multiplied by the point-spread function $T({}^2x;{}^1x)$ with respect to ${}^1x$. Therefore, the excited molecules $n^*(x,y,z,t)$ distributing in the (x,y,z) coordinate spreads and forms a distribution $h_1({}^1x,{}^1y,{}^1z)$ in a $({}^1x,{}^1y,{}^1z)$ coordinate with a point-spread function $T_1({}^1x,{}^1y,{}^1z;x,y,z)$:

$$h_1({}^1x,{}^1y,{}^1z) = \int\int T_1({}^1x,{}^1y,{}^1z;\ x,y,z)\ n^*(x,y,z,t)\ \mathrm{d}^3x\ \mathrm{d}t. \tag{2.14}$$

The time integration describes measurement by capturing an image. Here, an approximation in time is introduced. If the gas sheet is introduced continuously, the gas density spatial distribution is considered to be constant in time. The travel distances of the excited molecules depend on the data-capture time because the excited-state lifetime of each molecule is different. Since the time dependence of the beam profile shorter than the lifetime cannot be quantified, the measurement time Δt is assumed longer than the typical lifetime of the excited molecules. The typical lifetime is generally in the order of nano-seconds, and this approximation does not require a special treatment. Thus, the amount of the distribution spread due to the motion of the excited molecules can

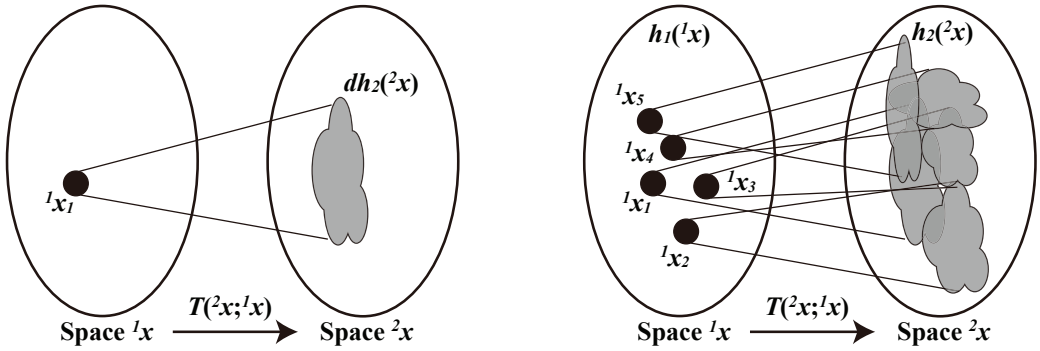

(a) (b)

Figure 2.5: A concept of the point-spread function: (a) for a point in the x space, (b) for all points in the x space.

be regarded as constant in time. Time dependence will not appear, and the integration in time is performed in advance:

$$h_1({}^1x,{}^1y,{}^1z) = \sigma \int T_1({}^1x,{}^1y,{}^1z;\ x,y,z)\ n(x,y,z)\ F(x,y;z)\,\mathrm{d}^3x \tag{2.15}$$

where $F(x,y;z)$ describes the integral of the 3-D beam profile $f(x,y,t;z)$ with respect to time t in Δt. In general, since an image of a region far from a focal point blurs, the out-of-focus effect has to be taken into account. This effect can be described as that the produced photon spatial distribution corresponding to $h_1({}^1x,{}^1y,{}^1z)$ is transformed by a point-spread function $T_2({}^2x,{}^2z;{}^1x,{}^1y,{}^1z)$ into a distribution $h_2({}^2x,{}^2z)$ whose coordinate system is defined on the input surface of the image intensifier,

$$h_2({}^2x,{}^2z) = \int T_2({}^2x,{}^2z;\ {}^1x,{}^1y,{}^1z)\ h_1({}^1x,{}^1y,{}^1z)\,\mathrm{d}^3({}^1x). \tag{2.16}$$

This transformation includes the effect due to the solid angle depending on the distance between the lens and the light source. The spatial-resolution reduction in the image intensifier is caused in the process of the electron transformation from the MCP to the phosphor screen. The electrons have an angular distribution at the exit of the MCP, and the spatial distribution broadens at the phosphor screen. This phenomenon can be described as transformation from $h_2({}^2x,{}^2z)$ into $h_3(\mu,\nu)$ using a point-spread function $T_3(\mu,\nu;\ {}^2x,{}^2z)$:

$$h_3(\mu,\nu) = \int T_3(\mu,\nu;\ {}^2x,{}^2z)\ \alpha_{I.I.}({}^2x,{}^2z)\ h_2({}^2x,{}^2z)\,\mathrm{d}^2({}^2x), \tag{2.17}$$

where $\alpha_{I.I.}({}^2x,{}^2z)$ is the amplification-efficiency spatial distribution of the MCP, and the (μ,ν) coordinate is defined on the output surface of the image intensifier and the surface of the CCD sensors. The luminous-intensity spatial distribution $g(\mu,\nu)$ of the captured image with the CCD camera can be described with the detection-efficiency spatial distribution $\alpha_{CCD}(\mu,\nu)$ as follows:

$$g(\mu,\nu) = \alpha_{CCD}(\mu,\nu)\ h_3(\mu,\nu). \tag{2.18}$$

Thus, the principle formula of the beam profile measurement with the gas sheet monitor can be derived by integrating Eqs. (2.15)-(2.18). The order of the integrals is changeable because the order of each phenomenon is expressed not by the order of integrals but by the combination of the variables in each point-spread function. The functions except the beam profile $F(x,y;x)$ can be described as a function $T(\mu,\nu;x,y,z)$ from Eqs. (2.15)-(2.18):

$$\begin{aligned} T(\mu,\nu;x,y,z) = \sigma\, n(x,y,z)\ \alpha_{CCD}(\mu,\nu) \int\int T_3(\mu,\nu;\ {}^2x,{}^2z)\ \alpha_{I.I.}({}^2x,{}^2z) \\ T_2({}^2x,{}^2z;\ {}^1x,{}^1y,{}^1z)\ T_1({}^1x,{}^1y,{}^1z;\ x,y,z)\ \mathrm{d}^3({}^1x)\ \mathrm{d}^2({}^2x). \end{aligned} \tag{2.19}$$

Finally, the correlation between the beam profile $F(x,y;z)$ of the time resolution Δt and the obtained image $g(\mu,\nu)$ is derived as a simple integral equation with the function $T(\mu,\nu;x,y,z)$:

$$g(\mu,\nu) = \int \mathrm{d}^3x\, T(\mu,\nu;x,y,z)\ F(x,y;z). \tag{2.20}$$

This equation means that an input beam profile signal F is converted into an output image g through a function T; the function T can be regarded as a response function of the gas sheet monitor. There remain some phenomena which are not precisely described and separated from the main constituent components explained above, the phenomena can be included in the response function $T(\mu,\nu;x,y,z)$ as they can be written as the same form as Eqs. (2.15)-(2.18).

References

[18] H. D. Zhang, A. Salehilashkajani, C. P. Welsch, M. Ady, J. Glutting, O. R. Jones, T. Marriott-Dodington, S. Mazzoni, A. Rossi, G. Schneider, R. Veness, and P. Forck, "Development of supersonic gas-sheet-based beam profile monitors", in *Proceedings of the International Particle Accelerator Conference IPAC2019*, (Melbourne, Australia, 2019), WEPGW096 (2019).

[20] Y. Hashimoto, T. Fujisawa, T. Morimoto, Y. Fujita, T. Honma, S. Muto, K. Noda, Y. Sato, and S. Yamada, "Oxygen gas-sheet beam profile monitor for the synchrotron and storage ring", Nucl. Instrum. Meth. Phys. Res. A **492**, 74–90 (2002).

[26] M. Putignano, "Supersonic Gas-Jet Based Beam Profile Monitor", University of Liverpool, Ph.D. dissertation (2012).

Chapter 3

Design of Gas Sheet Monitor

3.1 Gas species

Gas species for the sheet should be chosen considering the following four factors: the photon emission cross section, the excited-state lifetime, the main wavelength, and the influence on vacuum. The most important factor to choose the sheet-gas species is the photon emission cross section because one of the issues to realize beam profile measurement based on beam-induced photon detection is that the signal intensity tends to be low as compared with the ion/electron detection. The excited-state lifetime is also important because the excited molecules/ions can move with the thermal velocity and the excited ions are accelerated in local electromagnetic potentials during the lifetime; these motions reduce the accuracy of beam profile measurement. In particular, the contribution of the electromagnetic potentials is complicated and is difficult to be exactly compensated. The main wavelength in the produced photons determines the photon detector system including optical lenses. The optical system for visible light is easier to construct and adjust than the ones for the other wavelength lights. Ease of evacuating the injected gas should be also taken into account not to disturb the vacuum condition of the beam line. Considering these factors, nitrogen and noble gases are the candidates to create a gas sheet. The photon emission cross section is considered to be proportional to the amount of the energy deposition due to beam-gas interaction. The amount of the energy deposition can be described by the Bethe-Bloch formula [27], and the formula indicates that a heavier gas induces a large amount of the energy deposition; xenon has the largest cross section in noble gases except Rn and Og. Nitrogen has the three-times larger emission cross section in the visible wavelength range as compared with xenon [28]. The total emission cross section of nitrogen is 1.3×10^{-18} cm^2 for pro-

ton beam injection of 3 MeV equivalent. The main wavelength is considered as 391.4 nm which is emitted by the process of $B^2\Sigma_u{}^+(\nu = 0) \rightarrow X^2\Sigma_g{}^+(\nu = 0)$ as shown in Fig. 3.1 [15, 28–32]. The emission cross sections of nitrogen, neon, argon, and xenon in the visible wavelength range were measured as the luminous intensity of the captured image with the gas sheet monitor and 3 MeV H^- beam, and is shown in Table 3.1. (The details of the gas sheet monitor including the photon detector system and the H^- beam will be described in Section 3.2, Section 3.3 and Section 5.1.) Although these results does not indicate the precise ratios of the photon-emission cross section due to the detection efficiency with respect to wavelength, its tendency against gas species helps to choose the gas species in addition to some literatures. The lifetime of 58 ns for nitrogen longer than the one of 6 ns for xenon is a demerit to utilize nitrogen gas [28]. In this dissertation, the gas sheet monitor system was optimized for nitrogen gas because the emission cross section is the top priority to demonstrate the effectiveness of the gas sheet monitor.

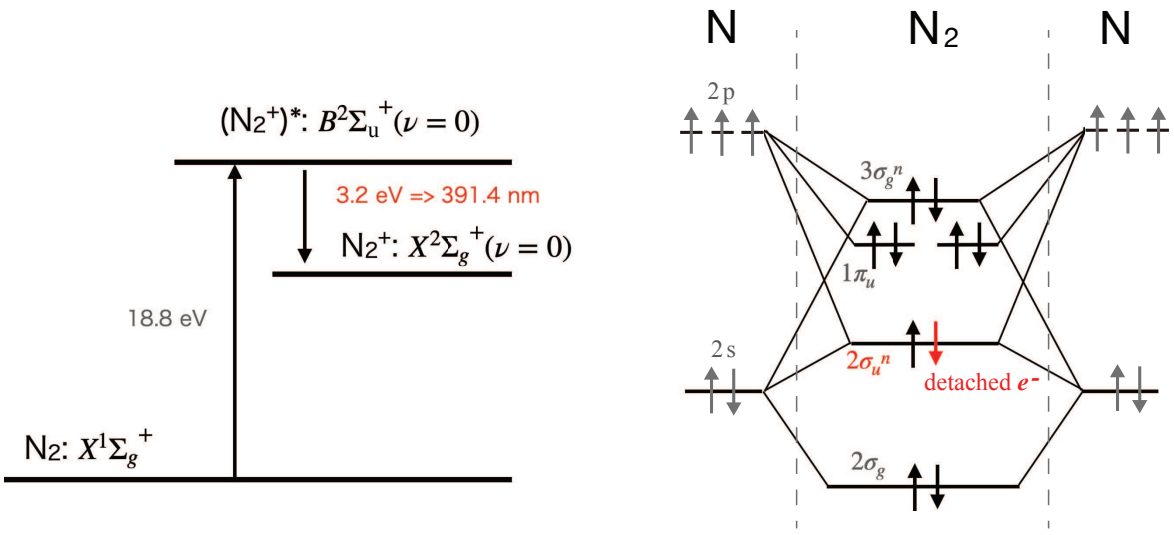

Figure 3.1: The main photon emission process for nitrogen gas.

Table 3.1: The luminous intensities of the captured image against N_2, Ne, Ar and Xe injection in the condition where the gas densities are the same.

Gas species	relative luminous intensity
N_2	1
Ne	0.15
Ar	0.25
Xe	0.36

3.2 Gas sheet generator and vacuum system

3.2.1 Gas flow simulation in molecular flow

As described in Chapter 2.1, the gas flow in the molecular flow region can be calculated with the simplified Boltzmann equation and the boundary condition being subject to the cosine law. However, solving the Boltzmann equation takes a high cost of computer resources due to the heavy load for treating the six-dimensional velocity-distribution function. According to the method of characteristics, solving a partial differential equation (PDE) is equivalent to finding a characteristic curve which transforms the PDE to an ordinary differential equation (ODE) and solving the ODE along the characteristic curve. The characteristic curve of the Boltzmann equation is the equation of motion. Since the intermolecular interactions are negligible, the equation of motion for each molecules can be solved individually. Therefore, in the molecular flow region, the method to solve the equation of motion is useful and often utilized as a Monte-Carlo simulation code, such as the Molflow+ code developed in CERN [33]. In this dissertation, the Monte-Carlo method was employed to design a gas sheet generator.

A gas sheet generator is developed as a rectangular conduit of the length L, the width w and the thickness d as shown in Fig. 3.2. The initial conditions of the molecular position (y, z) at $x = 0$ and the molecular velocity vector $(v_x, v_y, v_z) \rightarrow (v, \theta, \phi)$ are defined as follows. The initial position in the y-z plane is defined in the inlet surface with two uniform random numbers. The initial scalar velocity of the test particles are determined by the rejection sampling method according to the Maxwell-Boltzmann velocity distribution function for entering an aperture derived in Chapter 2.1:

$$f'(v) = \frac{1}{2} N_{\mathrm{mol}} \left(\frac{m}{k_B T_{th}} \right)^2 v^3 \exp\left(-\frac{m v^2}{2 k_B T_{th}} \right). \tag{2.12}$$

In the rejection sampling method, a uniform random number u_2 is compared with the function $f'(u_1)$ where u_1 is another uniform random number. If the random number u_2 is smaller than $f'(u_1)$, the number u_1 is adopted as the velocity: $v = u_1$. Otherwise, the uniform numbers u_1, u_2 are re-calculated and re-evaluated. The azimuthal angle ϕ in the y-z plane are determined randomly. The angle θ with respect to the x axis is defined to be subject to the cosine law based on the inverse sampling method [34, 35]. In the inverse sampling method, a non-uniform random number ξ being subject to a probability density distribution $p(\xi)$ can be correlated with a uniform random number

u in the range of [0,1] through the cumulative distribution function $P(\xi)$:

$$u = P(\xi) = \int_0^{\xi} p(t)\mathrm{d}t \tag{3.1}$$

The non-uniform random number ξ can be given with the inverse function of the cumulative distribution function:

$$\xi = P^{-1}(u) \tag{3.2}$$

If the cumulative distribution function and its inverse function can be analytically calculated, this method is faster than the rejection sampling method. In the present case, the probability distribution function is described as $p(\theta, \phi) = \cos\theta$, and the integral variable is a solid angle $\omega(\theta, \phi)$,

$$P(\theta) = \int_0^{\Omega} \mathrm{d}\omega\ p(t, \phi) \tag{3.3}$$

$$= \int_0^{\theta} \mathrm{d}t \int_0^{2\pi} \mathrm{d}\phi\ \cos t\ \sin t \tag{3.4}$$

$$= \frac{1}{2}(1 - \cos^2\theta) \tag{3.5}$$

From $u = P(\theta)$, the angle θ or the probability distribution function $p(\theta)$ can be described with the uniform random number u:

$$\theta = \cos^{-1}\left(\sqrt{1-u}\right) \tag{3.6}$$

or

$$p(\theta) = \cos\theta = \sqrt{1-u} \tag{3.7}$$

where the coefficient 1/2 of the cumulative distribution function $P(\theta)$ is normalized because the coefficient just restricts the range of the uniform random number.

The boundary conditions at $y = \pm\, w/2$ and $z = \pm\, d/2$ are the reflection being subject to the cosine law as described in Chapter 2.1. In the reflection process, the scalar velocity is assumed unchanged because the gas and the conduit temperatures are same and reflection does not change the thermal equilibrium condition. (In reality, the scalar velocities of the individual molecules change but the velocity-distribution function does not change.) The angles ϕ, θ are changed by the same way determining the initial conditions. If a test particle reaches to $x = 0$ or L, calculation of the particle is terminated and a counter of *return* or *pass* is increased, and calculation of the next

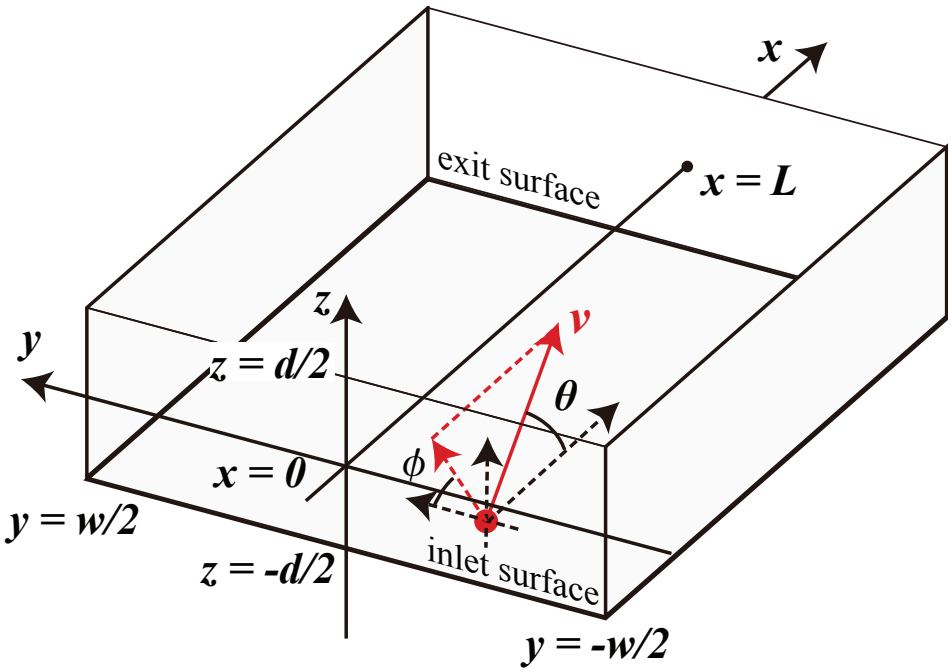

Figure 3.2: The geometry of the gas flow simulation. The gas sheet generator is a rectangular conduit of the length L, the width w and the thickness d. The angle θ is defined with respect to the normal direction of the surface where the test particle is reflected. The angle ϕ is defined on the reflection surface.

particle is started. The ratio of the numbers of particles passing the conduit to the particles injected in the conduit is defined as a transmission probability $K_{\rm cc}$ called the Clausing coefficient. This value gives a conductance C of the conduit which is one of the useful index evaluating the conduit:

$$C = C_0 K_{\rm cc} = \frac{1}{4} A \bar{v}\, K_{\rm cc} \tag{3.8}$$

where A is the area of the inlet surface, $\bar{v}$ is the mean speed in the upstream volume of the inlet surface, and C_0 is the conductance of the inlet-surface aperture.

After calculations of all injection test particles, the gas density spatial distribution is calculated with a small volume placed at a point where the density is needed as shown in Fig. 3.3. A mean time of flight τ in the volume is described with a particle flight length δs in the volume:

$$\tau = \frac{1}{N_{\rm test}} \sum_{i=1}^{N_{\rm test}} \frac{\delta s_i}{v_i} \tag{3.9}$$

where $N_{\rm test}$ is the number of the test particles entering the volume. Since all particles entering the volume do not pass through the volume in a same time, the gas density in

the volume is defined as a mean density against time:

$$n_{\text{test}} = \tau \frac{N_{\text{test}}}{\delta x\, \delta y\, \delta z} \tag{3.10}$$

This gas density is for the test molecules and is converted to the real density by gas flux whose unit is $\text{Pa}\,\text{m}^3/\text{s}$. The gas flux of 1 $\text{Pa}\,\text{m}^3/\text{s}$ corresponds to 2.65×10^{20} molecules/s according to the equation of state $p = nk_BT_{\text{th}}$. Since this gas flow simulation can be regarded as a calculation of a steady state gas flow in a unit time, a ratio of the calculation condition Q of the real gas flux to the number of the test molecules passing the conduit N_{pass} connects the simulation to the reality:

$$n = \frac{Q}{N_{\text{pass}}}\, n_{\text{test}}. \tag{3.11}$$

The gas density spatial distribution can be obtained by scanning the small volume.

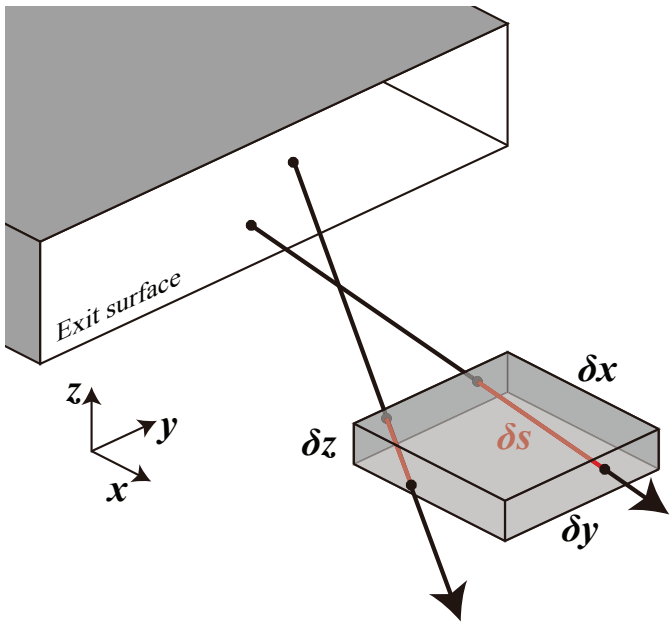

Figure 3.3: The gas density spatial distribution is measured with a small volume $\delta x\, \delta y\, \delta z$. The flight length of the test particle in the volume is defined as δs.

3.2.2 Design of gas sheet generator

First, the angular distributions of the gas flow with respect to angles α, β shown in Fig. 3.4 against the conduit shape of the length L, the width w and the thickness d are discussed. The angle α defined against the x axis in the x-z plane is an index to evaluate the gas flow spread in the thickness direction. The angle β specifying the direction with respect to the x axis in the x-y plane is an index to evaluate the gas flow spread in the width direction. Since change of the conduit length relatively corresponds to change of the width and the thickness in a same time, the gas-distribution spreads against the width and the thickness normalized by the length are evaluated. Figure 3.5 shows the flux distribution along the angles α, β against the conduit thickness d/L. The conduit length and width are 100 mm and 50 mm, respectively. The flux intensities are normalized by each peak intensity. The spread of the gas flow in the thickness (α) direction becomes narrow against a decrease of the thickness d/L: the beam effect of gas flow. On the other hand, the spread in the width (β) direction becomes broad against a decrease of the thickness d/L. These results can be understood by considering the speed distribution function. The speed distribution function determined by the temperature does not change even if the gas molecules pass through any conduits whose temperature is the same as the molecules. If the velocity distribution in the thickness direction becomes narrow, the velocity distributions in the other directions have to become broad to satisfy the thermal equilibrium condition. Figure 3.6 shows the flux distribution along the angles α, β against the conduit width w/L. The conduit length and thickness are 100 mm and 1 mm, respectively. Thees flux intensities are also normalized by the peaks. The spread of the gas flow in the thickness (α) direction becomes broad against a decrease of the width w/L. On the other hand, the spread in the width (β) direction becomes narrow against a decrease of the width w/L. These result can be understood with the same discussions described above. Since the gas flow spread in the sheet thickness is needed to be small to create a gas sheet, a wide and thin conduit is necessary.

Next, the conduit shape L, w, d is determined considering a target high-intensity beam. A low-energy, high-intensity beam is suitable to demonstrate the effectiveness of the gas sheet monitor because the beam cannot be measured with an ordinary profile monitor using a metal or carbon-nanotubes wire due to the energy deposition. The amount of energy deposition can be described by the Bethe-Bloch formula which has a peak at 0.1-1 MeV for a proton beam [27, 36]. In J-PARC, there is the RFQ test stand [37, 38] creating a 3 MeV H^- beam whose typical beam size is 2-3 mm as a root

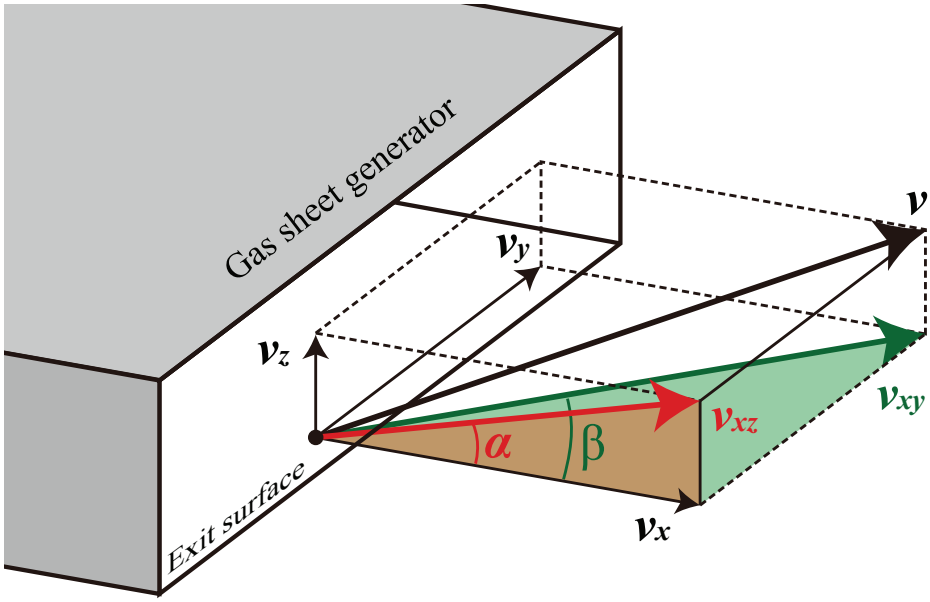

Figure 3.4: The angular distribution of the molecules is evaluated with the flux intensity distribution along two kinds of angles. The angle α is defined with respect to the x axis in the x-z plane. The angle β is defined with respect to the x axis in the x-y plane.

mean square and is around 20 mm in the full width in both x and y directions (See Chapter 5). The gas sheet monitor developed in this dissertation is optimized to the beam of the J-PARC RFQ test stand. The free space on the beam line to install the gas sheet monitor is restricted to about 225 mm along the beam axis because three focusing magnets are placed in short spans to avoid the space-charge-based beam divergence. The gas sheet conduit width of 50 mm is the maximum size that can be installed. Considering the target beam size of 20 mm, the width was determined as 50 mm. The remaining parameters of the length and the thickness were determined with Fig. 3.7 showing the flux distribution along the angles α, β against change of the conduit length L. The center position of Fig. 3.7a is shifted to -1.0 to see the details. The angular distribution along α is almost same at d/L smaller than 0.001 (the black dashed line). Since the angular distribution along β is not important as compared with the one along α, the d/L ratio was determined at 0.001. Considering the realistic size of the conduit, the length and the thickness were determined at 100 mm and 0.1 mm, respectively.

Next, the designed gas sheet generator which is the rectangular conduit of the 100 mm length, the 50 mm width and the 0.1 mm thickness is evaluated by calculating the conductance and the gas density spatial distribution. The simulated transmission probability of the conduit and the conductance calculated by Eq. (3.8) are 6.50×10^{-3} and 3.94×10^{-6} m^3/s, respectively. A typical inlet gas flux is chosen to give the maximum

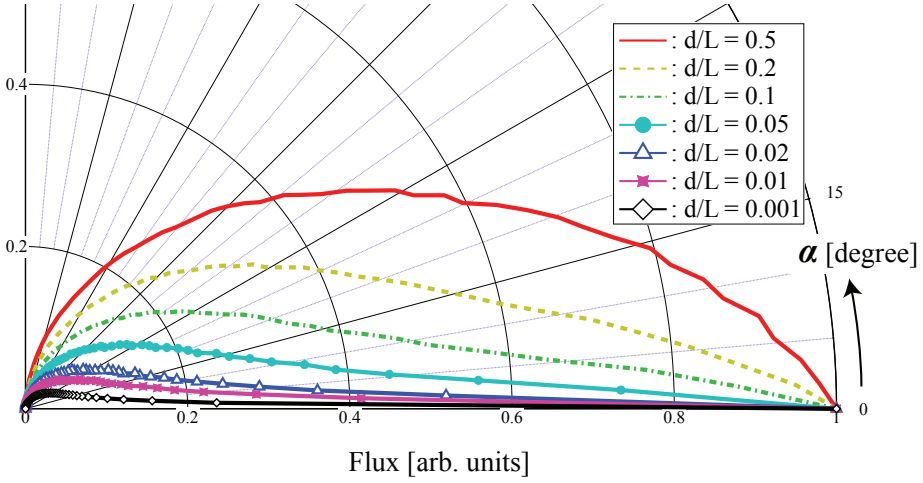

(a)

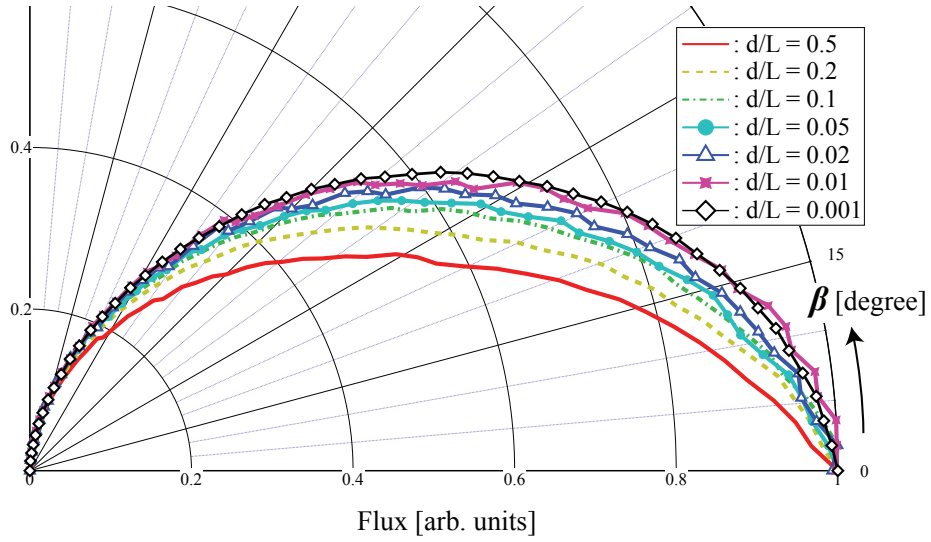

(b)

Figure 3.5: The gas flux distribution along (a) the angle α and (b) angle β against the normalized conduit thickness d/L for $L = 100$ mm and $w = 50$ mm.

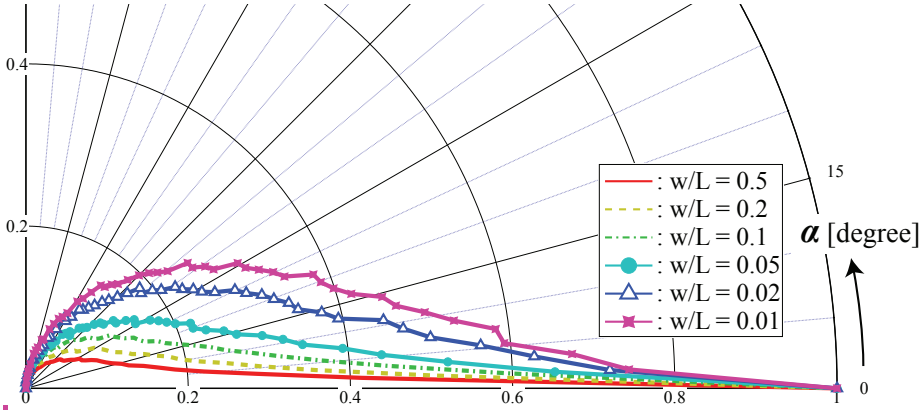

(a)

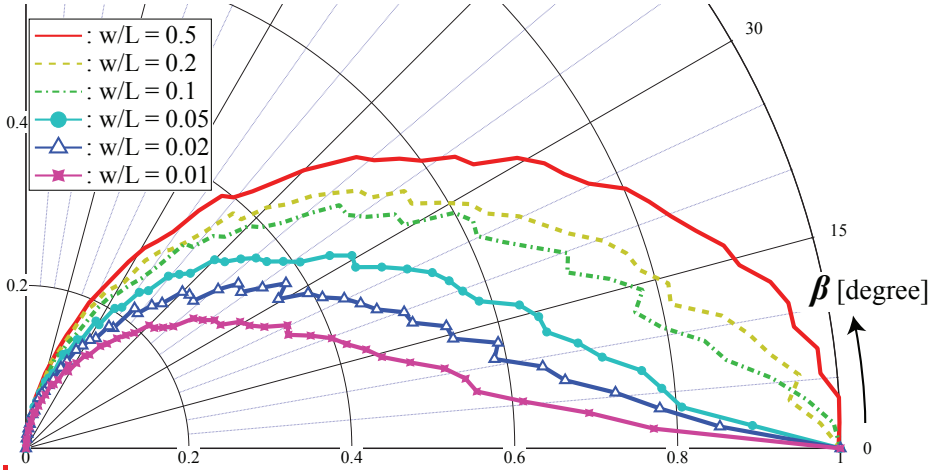

(b)

Figure 3.6: The gas flux distribution along (a) the angle α and (b) angle β against the normalized conduit width w/L for $L = 100$ mm and $d = 1$ mm.

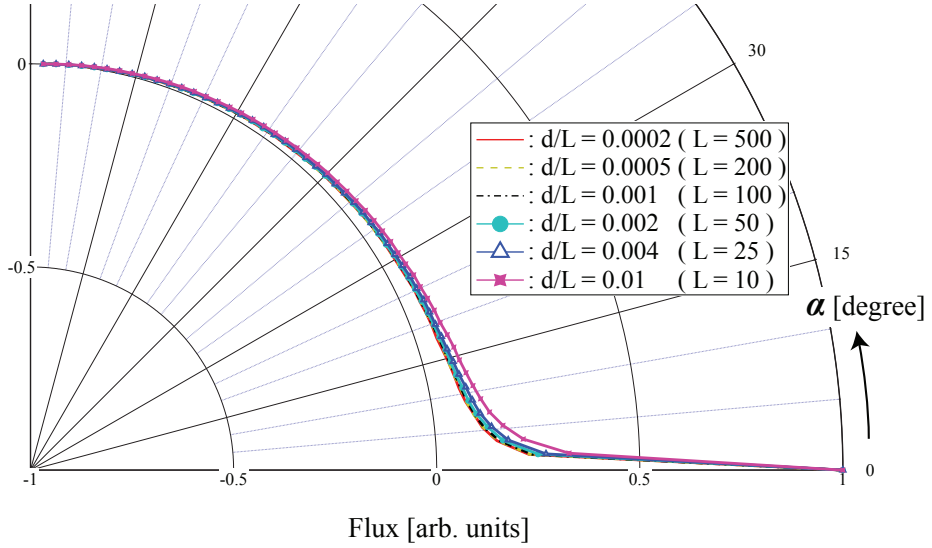

(a)

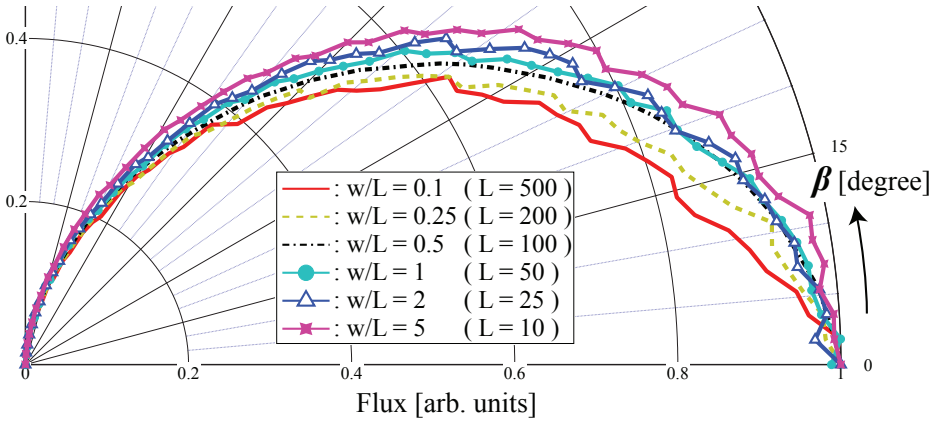

(b)

Figure 3.7: The gas flux distribution along (a) the angle α and (b) angle β against the conduit length L for $w = 50$ mm and $d = 0.1$ mm. The center position of the upper panel is shifted to -1 in the intensity axis.

inlet pressure in the range of the molecular flow. (The definition of the molecular flow is that the mean-free path of the molecules is longer than the characteristic length of the chamber.) For the gas sheet generator, the thickness of 0.1 mm is the characteristic length because the reflection process in the thickness direction is considered to be dominant. The mean-free path of 0.1 mm is given by 68.1 Pa, and the gas flux of 2.68×10^{-4} Pa m^3/s is given by the conductance and the pressure (see Section 3.2.4). The gas density spatial distributions at the typical inlet gas flux of 2.68×10^{-4} Pa m^3/s are shown in Fig. 3.8. All of the distributions are projected in the three-dimensional velocity space. Figure 3.8a shows the density distribution on x axis: $y = z = 0$. Figures 3.8b, 3.8c show the distributions along the y and z axes at a distance of 50 mm from the exit surface in the x direction. The distance of 50 mm is chosen for the beam not to strike the generator. The test molecules passing the generator are evacuated without any reflections for simplicity; the background gas density consisting of molecules accumulated in a chamber is zero. Since the gas density rapidly decreases along the x (flow) direction as shown in Fig. 3.8a, the distance between the beam axis and the generator exit should be short. The gas sheet is uniform in 20 mm along the y axis as shown in Fig. 3.8b. The gas sheet of 0.3 mm thickness in the full width at half maximum is realized as described in Fig. 3.8c.

Here, the gas pressure in the main chamber of the gas sheet monitor which is attached to the beam line is estimated. The beam line pressure is limited up tp 10^{-3} Pa because the gas sheet injection must not affect the gas pressure in the RFQ cavity to avoid discharge. When the injection gas flux is 2.68×10^{-4} Pa m^3/s, the required minimum pumping speed is 268 L/s, and the background pressure is to be 1×10^{-3} Pa. Since the peak pressure is 3.86×10^{-3} Pa at $x = 50$ mm without the background pressure, the ratio of the peak pressure to the background pressure is about 5. A pump having a 1000 L/s pumping speed which is the maximum speed of a pump attachable to the main chamber due to the spatial restriction of the beam line was chosen to increase the density ratio. In this case, the background pressure reduces down to 2.68×10^{-4} Pa from 1×10^{-3} Pa, and the peak pressure becomes 4.13×10^{-3} Pa including the background pressure. To further reduce the background pressure, a cover chamber having a rectangular slit surrounding the gas sheet generator as shown in Fig. 2.3b was designed, and a vacuum pump was attached to the opposite side of the slit to evacuate molecules reflected on the slit plate. The slit size was set to 50 mm $\times$ 0.5 mm considering the alignment to the generator exit of 0.1 mm thickness, and was placed at a distance of 10 mm from the exit. Figure 3.9 shows the gas density distributions in y and z directions

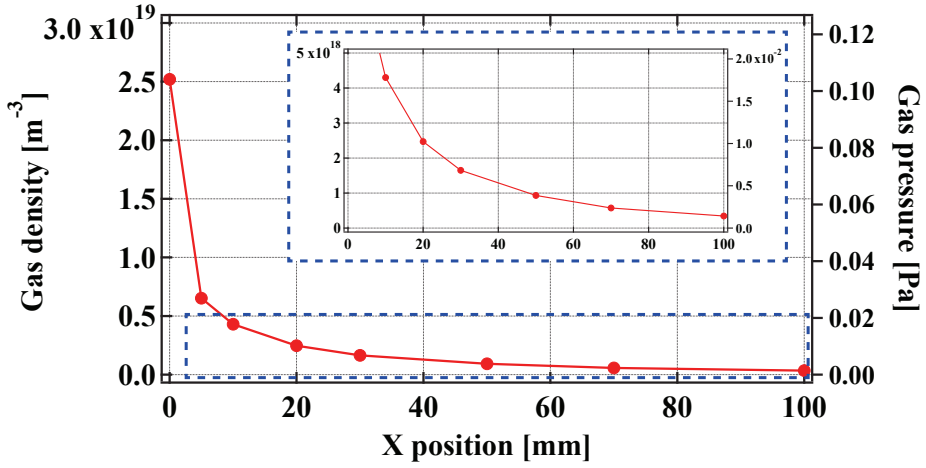

(a)

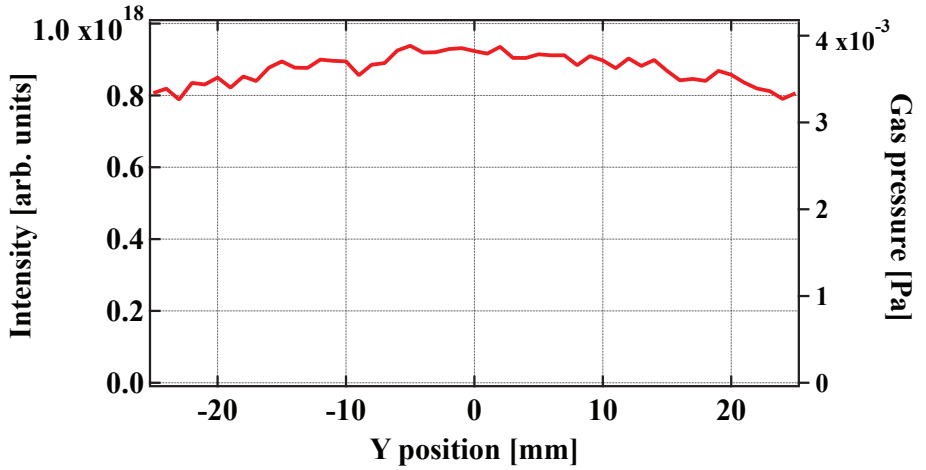

(b)

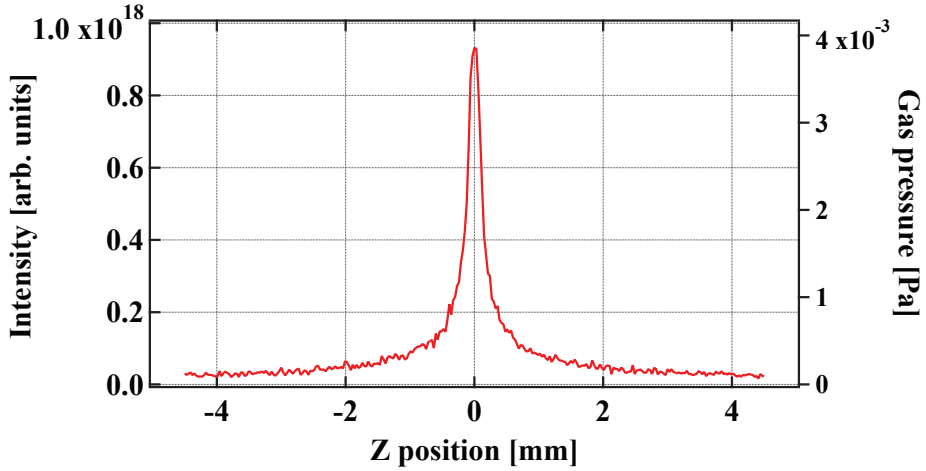

(c)

Figure 3.8: The gas density spatial distribution (a) along the x axis at $y = z = 0$ mm, (b) along the y axis at $x = 50$ mm, $z = 0$ mm, and (c) along the z axis at $x = 50$ mm, $y = 0$ mm.

with the cover chamber as compared with the ones without the cover chamber. The cover chamber does not affect the core part of the gas distribution and evacuates the tail part. If the pump attached to the cover chamber has an infinite pumping speed, the gas flux entering the beam line can be reduced down from 2.68×10^{-4} Pa m^3/s to 7.42×10^{-5} Pa m^3/s: 72% reduction. The background pressure decreases to 7.42×10^{-5} Pa, and the ratio of the peak pressure including the background pressure to the background pressure becomes about 53.

3.2.3 Developed gas sheet monitor system

The gas sheet monitor developed based on the above discussions is shown in Fig. 3.10. Flange size of the main chamber attached to the beam line is restricted up to the Conflat® 203. To evacuate the injected gas sheet, a cryopump having a pumping speed of 750 ℓ/s and a turbomolecular pump (TMP) having a 300 ℓ/s are attached to the main chamber. On the opposite side of the cryopump, the cover chamber consisting of the gas sheet generator, the 50 mm $\times$ 0.5 mm rectangular slit, and a TMP having a pumping speed of 370 ℓ/s is attached. The gas sheet is formed with the tilt angle of 36 degrees with respect to the beam axis.

3.2.4 Evaluation of the generator and the vacuum system

To evaluate the developed gas sheet generator and the pumping system, the gas pressures at some points were measured against the inlet pressure at the off-line setup composed of only the gas sheet monitor, and the conductance against the inlet pressure was estimated. In molecular flow region, the gas flux Q flowing between two volumes $p_1 > p_2$ is described as follows:

$$Q(p) = C(p_1 - p_2) \simeq Cp_1 \tag{3.12}$$

where C is the conductance between the two volumes and is constant against the pressures. The gas flux is approximately in proportion to the upstream pressure. In the viscous flow region, the conductance becomes proportional to the average gas pressure $\bar{p} = (p_1 + p_2)/2$, and the gas flux is approximately proportional to the square of the upstream pressure:

$$Q(p) = C(\bar{p})\,(p_1 - p_2) \propto {p_1}^2 \tag{3.13}$$

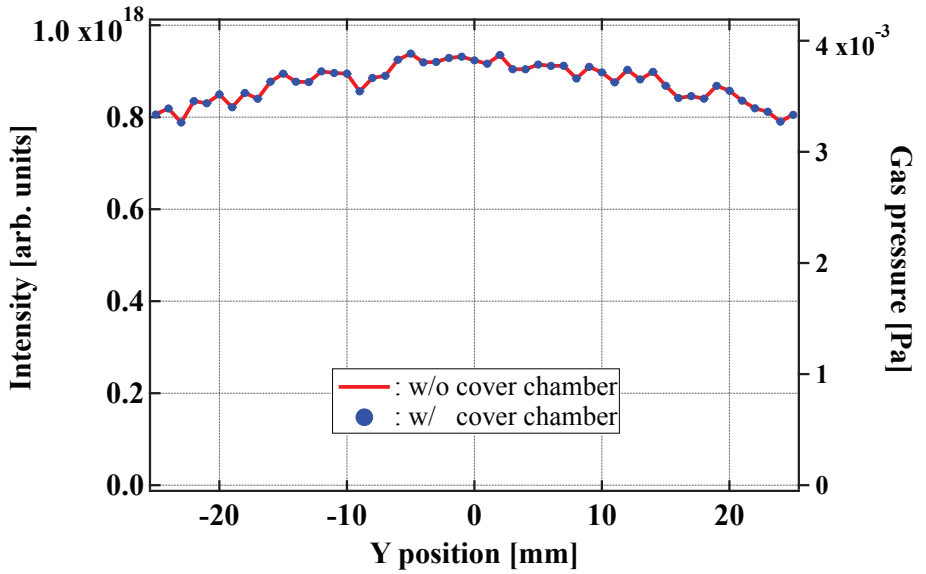

(a)

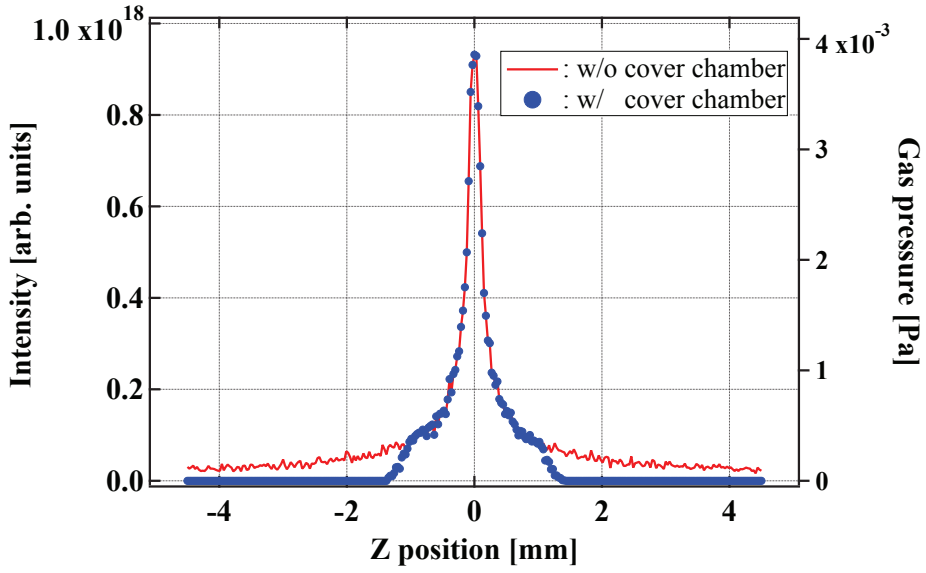

(b)

Figure 3.9: The comparison of the gas density spatial distribution with and without the cover chamber: (a) the distribution along the y axis at $x = 50$ mm, $z = 0$ mm and (b) the distribution along the z axis at $x = 50$ mm, $y = 0$ mm.

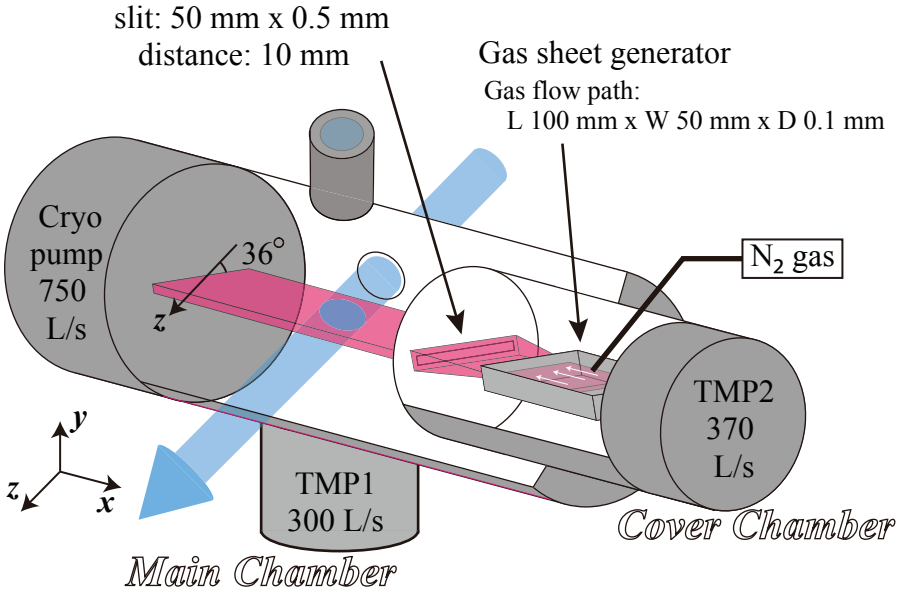

Figure 3.10: The gas sheet monitor consists of a gas sheet generator, a cover chamber, a main chamber, and vacuum pumps. The gas sheet is tilted 36° against the beam(z) axis. The monitor dimensions are 1,500 mm × 600 mm × 220 mm in x, y, and z axes.

Therefore, the dependence of the conductance against the inlet pressure is a useful index to know the characteristic of the conduit.

The gas pressures were measured at three points as shown in Fig. 3.11. The gas fluxes are defined with the pressure gauges and the pumping speeds of each pumps S:

$$Q_{\mathrm{mc}} = p_{\mathrm{mc}} \left(S_{\mathrm{cp}} + S_{\mathrm{TMP1}}\right) \tag{3.14}$$

$$Q_{\mathrm{cover}} = p_{\mathrm{cover}}\, S_{\mathrm{TMP2}} \tag{3.15}$$

$$Q_{\mathrm{in}} = Q_{\mathrm{mc}} + Q_{\mathrm{cover}}. \tag{3.16}$$

The conductance of the gas sheet generator can be estimated by

$$Q_{\mathrm{in}} = C\, p_{\mathrm{in}}. \tag{3.17}$$

Figure 3.12a shows the gas pressure of the cover chamber p_{cover} and the main chamber p_{mc} against the inlet pressure of the sheet generator p_{in}. Figure 3.12b shows the gas injection flux Q_{in}, the gas flux evacuated at the cover chamber Q_{cover}, and the gas flux evacuated at the main chamber Q_{mc} against the inlet pressure. Since the gas pressure in the chamber which the pumps are attached is up to 10^{-2} Pa, the pumping speed can be approximately uniform at typical values described in the catalog [39]. At the inlet pressure of 70 Pa, the injection gas flux is $3.0{\times}10^{-4}$ Pa m^3/s which well agrees

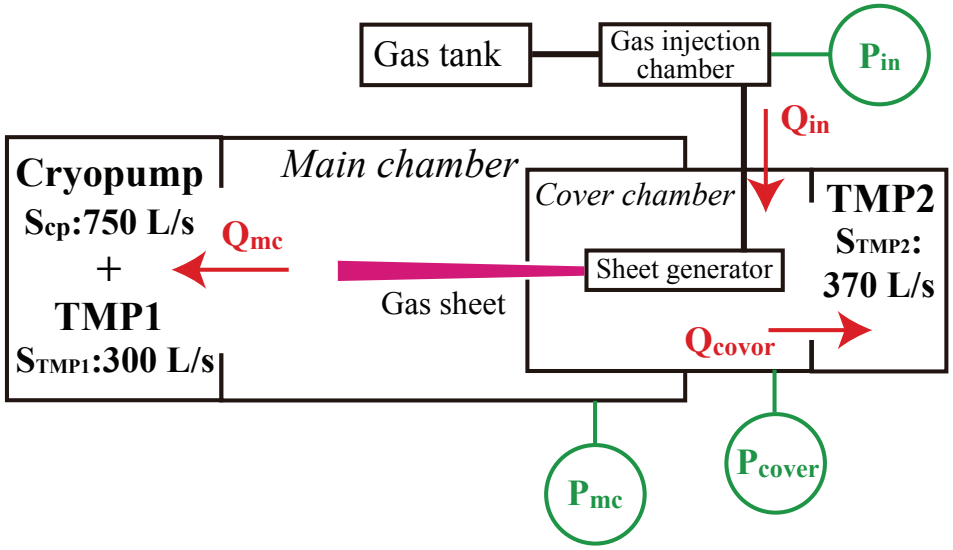

Figure 3.11: The diagram of the gas sheet monitor system. The gas pressures are defined at the generator inlet, in the cover chamber, and in the main chamber.

with the estimation value of 2.7×10^{-4} Pa m^3 in Section 3.2.2. The gas pressure in the main chamber is 4.3×10^{-5} Pa which is a half of the estimated value of 7.4×10^{-5} Pa. To clarify the reason of the difference, the gas flux reduction ratio due to the cover chamber $Q_{\rm cover}/Q_{\rm in}$ is shown in Fig. 3.13. The flux ratio is almost constant at 77% for the inlet pressure less than 1 Pa which almost agrees with the simulated value of 72% and increases against a rise in the inlet pressure over 1 Pa. These results imply that the gas density distribution becomes broad over 1 Pa injection due to intermolecular collisions and the main chamber flux $Q_{\rm mc}$ relatively reduces. Broadening of the gas density distribution can be also expected from the characteristic of the conductance shown in Fig. 3.14. In the lower pressure region less than 0.2 Pa, the conductance is constant against the inlet pressure: molecular flow. After 0.2 Pa the conductance decreases against increase of the inlet pressure and takes a minimum at 100 Pa: the Knudsen minimum. This result indicates that the effect of the intermolecular collisions appears due to the short mean-free path. The most gas molecules entering the generator are reflected around the inlet. Once the molecules obtain a large reflection angle, they pass through the generator; the molecules travels a few tens of mm. Since the mean-free path at 0.1 Pa is about 60 mm, the molecules traveling over 60 mm collide with other molecules. The intermolecular collisions are considered to induce the decrease of the conductance and spread of the sheet-gas distribution. On the basis of an estimation using the mean-free path, the fully collisionless flow may be realized at the pressure less than 0.07 Pa against the 100 mm long conduit. Thus, the conduit length is an

important parameter to determine the fully collisionless pressure region. After 100 Pa the conductance rapidly increases because the intermolecular collisions are dominant to determine the gas flow; the gas flow model becomes viscous flow. The conductance which is linearly proportional to the inlet pressure as shown in Fig. 3.14b also indicates the characteristic of viscous flow.

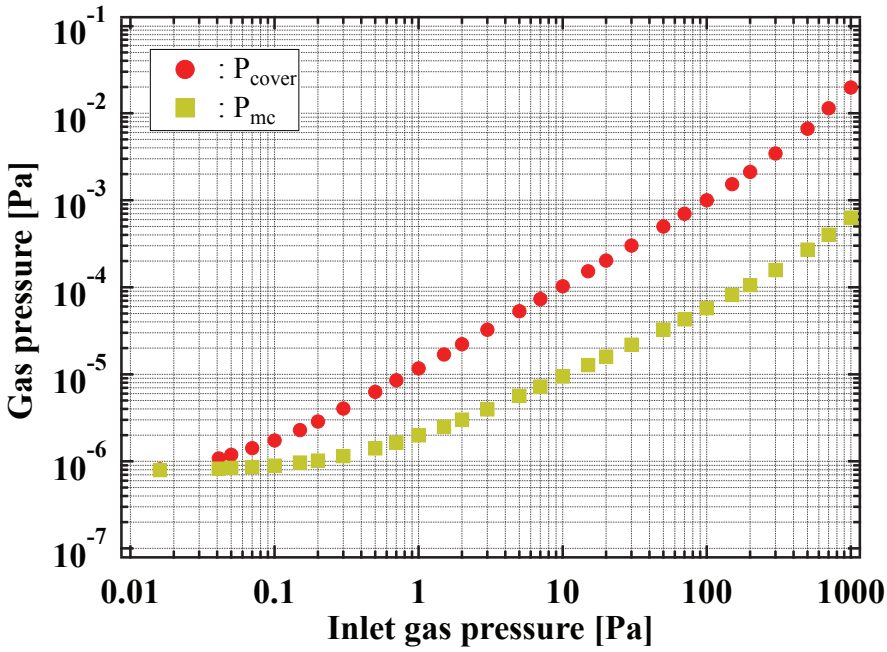

(a)

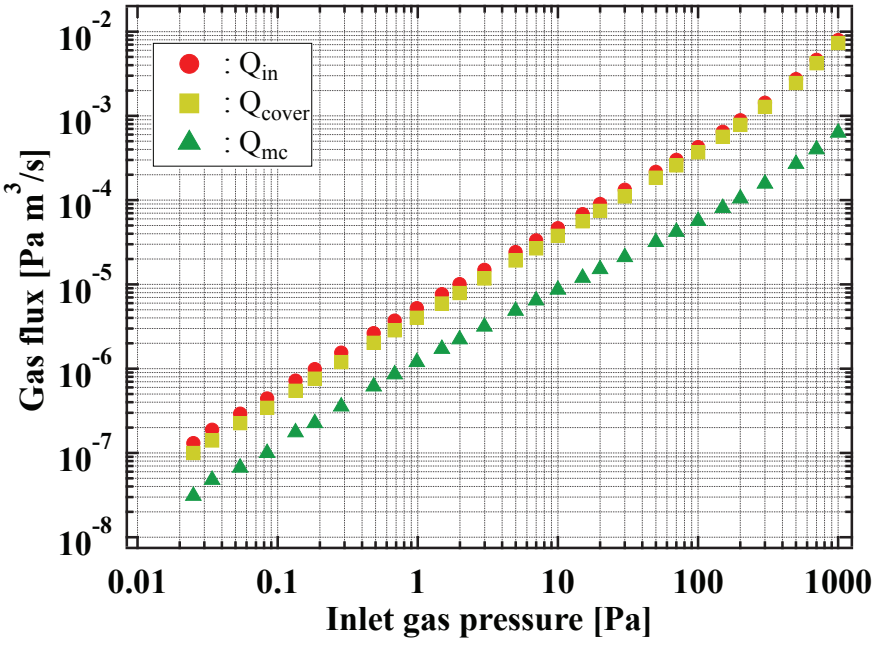

(b)

Figure 3.12: The characteristics of (a) the gas pressures at the cover chamber and the main chamber and (b) the injected gas flux, the evacuated flux at the cover chamber, and the evacuated flux at the main chamber against the inlet pressure.

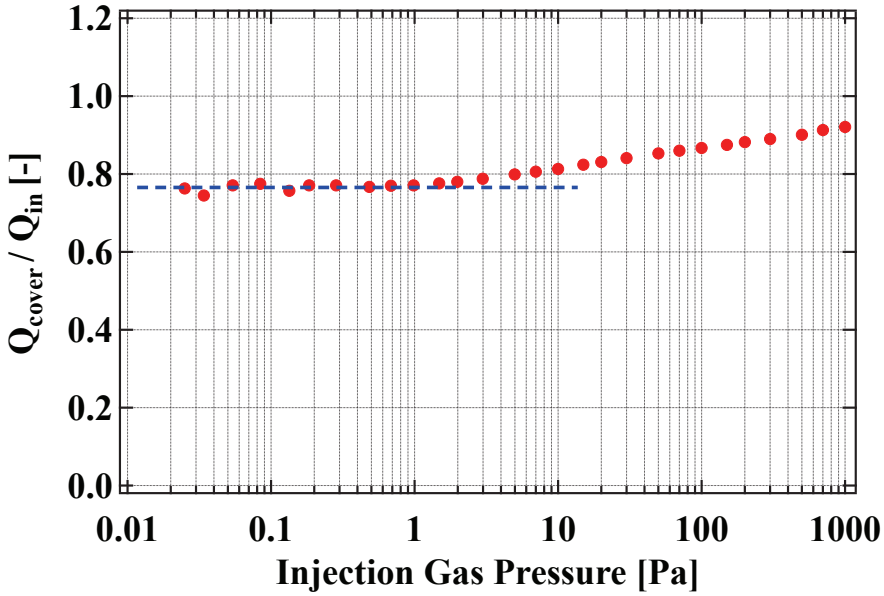

Figure 3.13: The ratio of the evacuated gas flux at the cover chamber to the injected gas flux against the inlet pressure.

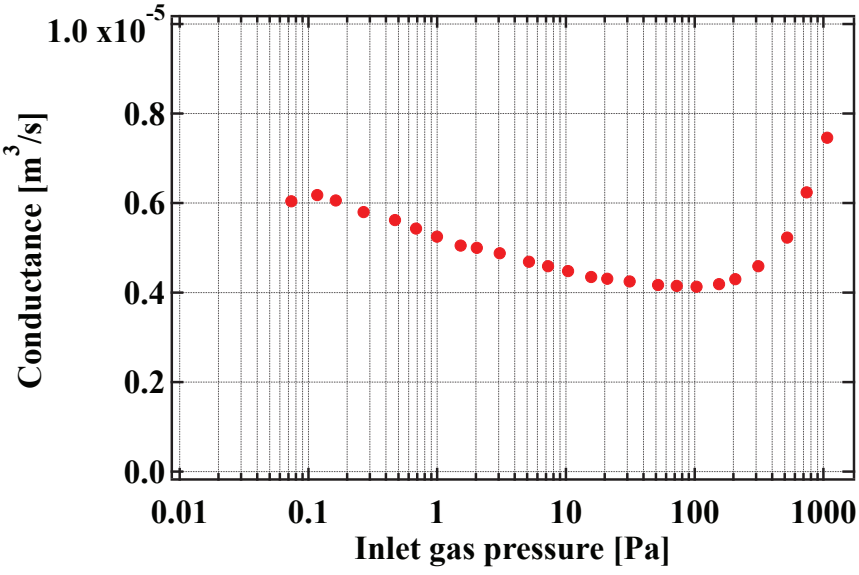

(a)

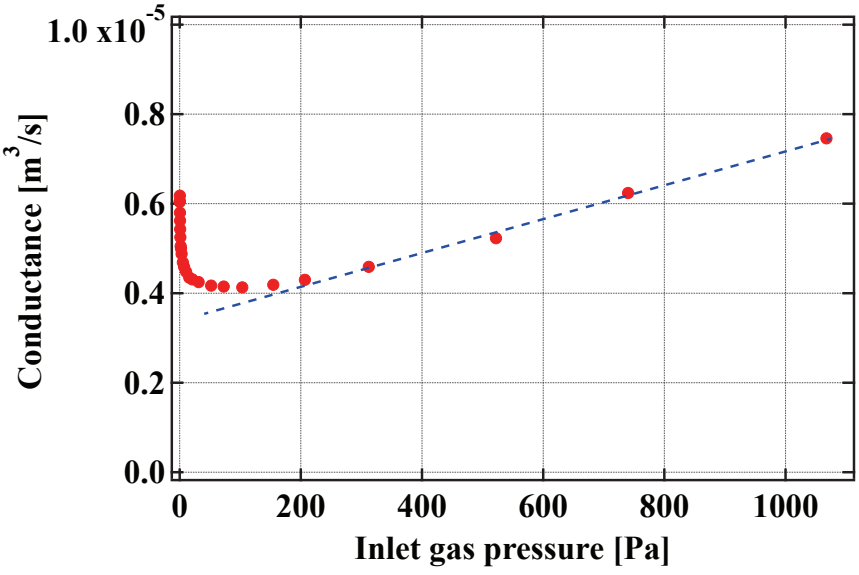

(b)

Figure 3.14: The characteristic of the conductance against the inlet pressure: (a) logarithmic scale and (b) linear scale.

3.3 Photon detector system

Figure 3.15 shows the gas sheet monitor with a photon detecter system. The photon detector system consists of a set of optical lenses (Nikon Co., AI Nikkor 35mm 1:1.4 [40]), an image intensifier (Hamamatsu Photonics K.K., C9016-21 [41]), and a CCD camera (BITRAN Co., BU-66EM [42]). The F-number and the focal length of the optical lens system are F/1.4 and 35 mm, respectively. The incident solid angle into the optical lenses is 0.012 sr (0.1% of 4π) as computed from the effective lens diameter of 25 mm and the distance of 200 mm between the objective lens and the center of the beam pipe. The image intensifier increases photon signal up to 10^4 times by the built-in multi-channel plate which can be gated with 25 ns, 2 kHz. The CCD camera has 1920 $\times$ 1080 pixels of 16 bit CCD image sensors that are 5.5 μm square each. One side of the sensor pixel on the image corresponds to 32 μm at the in-focus region of the beam-gas-interaction point. An anti-reflection plate is placed to reduce the number of photons which are reflected on the chamber wall and blur the beam profile image.

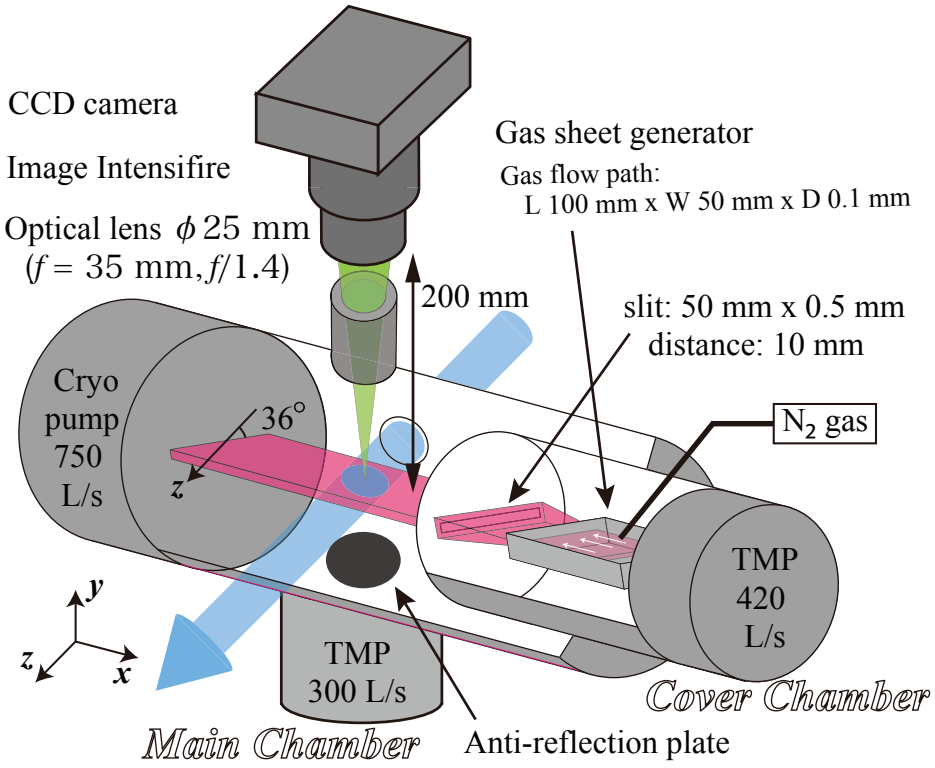

(a)

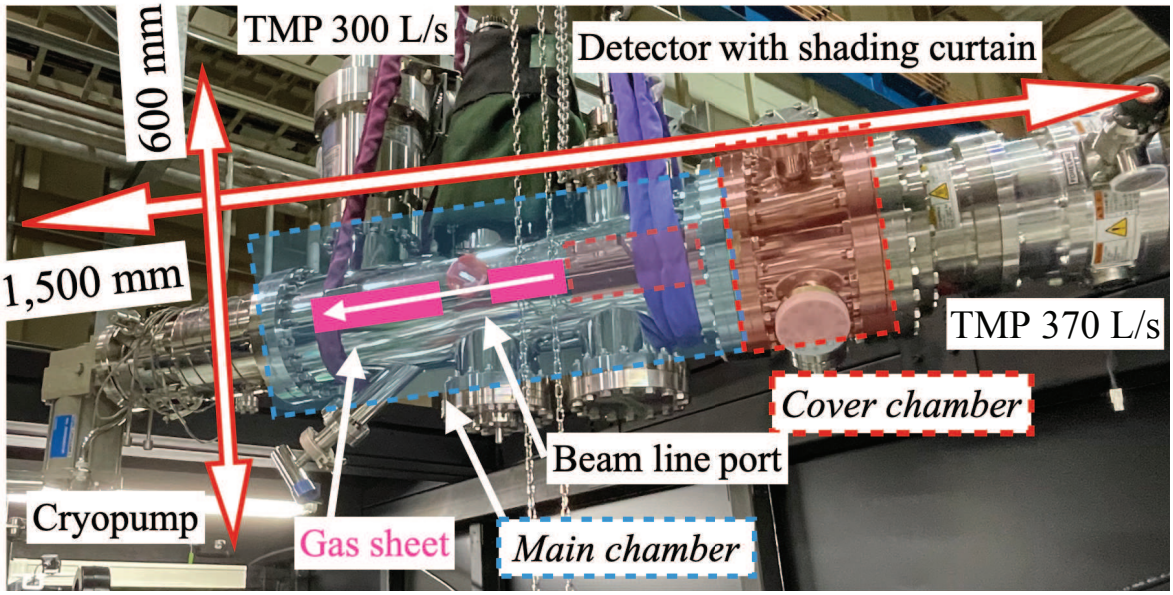

(b)

Figure 3.15: The gas sheet monitor system with the photon detector system consisting of a set of optical lenses, an image intensifier, and a CCD camera: (a) the schematic diagram and (b) the photo.

References

[15] F. Becker, C. Andre, P. Forck, and D. H. H. Hoffmann, in *8th European Workshop on Beam Diagnostics and Instrumentation for Particle Accelerators(DIAPAC)*, (Venice, Italy, 2017), MOO3A02.

[27] F. Bloch, "Bremsvermögen von Atomen mit Mehreren Elektronen", Zeitschrift fü Physik **81**, 363–376 (1933).

[28] M. A. Plum, E. Bravin, J. Bosser, and R. Maccaferri, "Ionizaion cross section data of nitrogen, methane, and propane for light ions and electrons and their suitability for use in track structure simulation", Nucl. Instrum. Meth. Phys. Res. A **492**, 74–90 (2002).

[29] R. H. Hughes and J. L. Philpot, "Spectra Induced by 200-kev Proton Impact on Nitrogen", Phys. Rev. **123**, 2084–2086 (1961).

[30] J. L. Philpot and R. H. Hughes, "Spectroscopic Study of Controlled Proton Impact on Molecular Nitrogen", Phys. Rev. **133**, A107–A110 (1964).

[31] J. M. Hoffman, G. J. Lockwood, and G. H. Miller, "Absolute emission cross section for N_2^+ (3914 Å) for proton incident on N_2 gas", Phys. Rev. A **11**, 841–845 (1975).

[32] T. E. Stewart, G. S. Hurst, T. E. Bortner, J. E. Parks, F. W. Martin, and H. L. Weidner, "Proton Excitation of Continuous Emission in the Noble Gases", J. Opt. Soc. Am. **60**, 1290–1297 (1970).

[33] MOLFLOW+, `http://molflow.web.cern.ch`.

[34] L. Devroye, *Non-uniform random variate generation* (Springer-Verlag, 1986).

[35] L. L. Carter and E. D. Cashwe, "Particle-Transport Simulation with the Monte Carlo Method", ERDA Critical Review Serie (1975) `10.2172/4167844`.

[36] R. M. Sternheimer, "Density Effect for the Ionization Loss in Various Materials", Phys. Rev **103**, 511–515 (1956).

[37] Y. Kondo, T. Morishita, S. Yamazaki, T. Hori, Y. Sawabe, E. Chishiro, S. Fukuta, K. Hasegawa, K. Hirano, N. Kikuzawa, I. Koizumi, A. Miura, H. Oguri, K. Ohkoshi, F. Sato, S. Shinozaki, A. Ueno, H. Kawamata, T. Sugimura, A. Takagi, Z. Fang, Y. Fukui, K. Futatsukawa, K. Ikegami, T. Maruta, T. Miyao, and K. Nanmo, "Beam test of a new radio frequency quadrupole linac for the Japan Proton Accelerator Research Complex", Phys. Rev. ST Accel. Beams **17**, 120101 (2014).

[38] Y. Kondo, T. Morishita, K. Hirano, T. Ito, N. Kikuzawa, R. Kitamura, H. Oguri, K. Ohkoshi, S. Shinozaki, K. Shinto, Z. Fang, Y. Fukui, K. Futatsukawa, K. Ikegami, T. Miyao, K. Nanmo, M. Otani, T. Shibata, T. Hori, Y. Nemoto, Y. Sato, F. Kobayashi, D. Takahashi, R. Tasaki, Y. Ito, Y. Kato, T. Ishiyama, and Y. Sawabe, "Upgrade of the 3-MeV Linac for testing of accelerator components at J-PARC", Journal of Physics: Conference Series **1350**, 012077 (2019).

[39] OSAKA VACUUM LTD. `https://www.osakavacuum.co.jp/products/detail0048.html`.

[40] NIKON CORPORATION, `http://www.nikon.com`.

[41] HAMAMATSU PHOTONICS K. K. `http://www.hamamatsu.com/`.

[42] BITRAN CORPORATION. `http://www.bitran.co.jp`.

Chapter 4

Response Function Measurement

According to the principle equation Eq. (2.20) of beam profile measurement with the gas sheet monitor derived in Chapter 2.2

$$g(\mu,\nu) = \int T(\mu,\nu;x,y,z)\ F(x,y;z)\ \mathrm{d}^3x, \tag{2.20}$$

the response function $T(\mu,\nu;x,y,z)$ must be quantified to reconstruct the beam profile $F(x,y,z)$ from the captured image $g(\mu,\nu)$. In this chapter, the method to measure the response function and the measurement result are described.

4.1 Principle of response function measurement

The response-function measurement method based on beam profile measurement with the gas sheet monitor is devised since the response function consists of a lot of contributions including the ones which are sensitive to the gas sheet monitor system. The profile measurement with the gas sheet monitor is described as the integral equation Eq. (2.20). If the integral is removed and the beam profile is given, the response function can be measured as an image $g(\mu,\nu)$ which is the output of the gas sheet monitor. A pencil beam described as a delta function which is constant against the z direction and time t is applied to the gas sheet monitor at an off-line setup, and the integral can

be removed at the pencil beam position (x_0, y_0):

$$\begin{aligned} g(\mu,\nu) &= \int T(\mu,\nu;x,y,z)\ F(x,y;z)\ \mathrm{d}^3x \\ &= \int T(\mu,\nu;x,y,z)\ \delta(x-x_0)\delta(y-y_0)\ \mathrm{d}^3x \\ &= \int T(\mu,\nu;x_0,y_0,z)\ \mathrm{d}z \\ &\equiv T_{4\mathrm{D}}(\mu,\nu;x_0,y_0). \end{aligned} \tag{4.1}$$

The integral with respect to the z direction cannot be removed because the pencil beam travels along the z direction and the z dependance of the 2-D profile cannot be described as a delta function. The response function with the integral in the z direction is defined as a four-dimensional response function. The entire 4-D response function $T_{4\mathrm{D}}(\mu,\nu;x,y)$ can be obtained by scanning the pencil beam position. The 4-D response function enables to reconstruct a 2-D beam profile $F(x,y)$ which is approximated as uniform in the z direction:

$$\begin{aligned} g(\mu,\nu) &= \int T(\mu,\nu;x,y,z)\ F(x,y;z)\ \mathrm{d}^3x \\ &= \int T(\mu,\nu;x,y,z)\ F(x,y)\ \mathrm{d}^3x \\ &= \int\int \left(\int T(\mu,\nu;x,y,z)\ \mathrm{d}z \right)\ F(x,y)\ \mathrm{d}x\ \mathrm{d}y \\ &= \int\int T_{4\mathrm{D}}(\mu,\nu;x,y)\ F(x,y)\ \mathrm{d}x\ \mathrm{d}y. \end{aligned} \tag{4.2}$$

If the z dependance of the 2-D beam profile needs to be analyzed, a 5-D response function has to be measured with another method. When the pencil beam differs from the high-intensity beam in the current density or the charge, the effect of the motion in the excited-state lifetime cannot be exactly compensated, and the difference causes an error of the reconstructed profile against the real profile.

4.2 Experimental apparatus

Figure 4.1 shows the experimental apparatus for the response-function measurement. An electron gun is employed as a pencil beam source and is attached to the developed gas sheet monitor described in Chapter 3 via an X-Y stage. A Faraday cup is also attached to the beam-line port of the gas sheet monitor to collect the electron beam. The electrons emitted from a LaB_6 hot cathode form a beam of 10 μA by 3 kV DC extraction. The electron beam scan is realized with the X-Y stage whose spatial resolution is 0.01 mm.

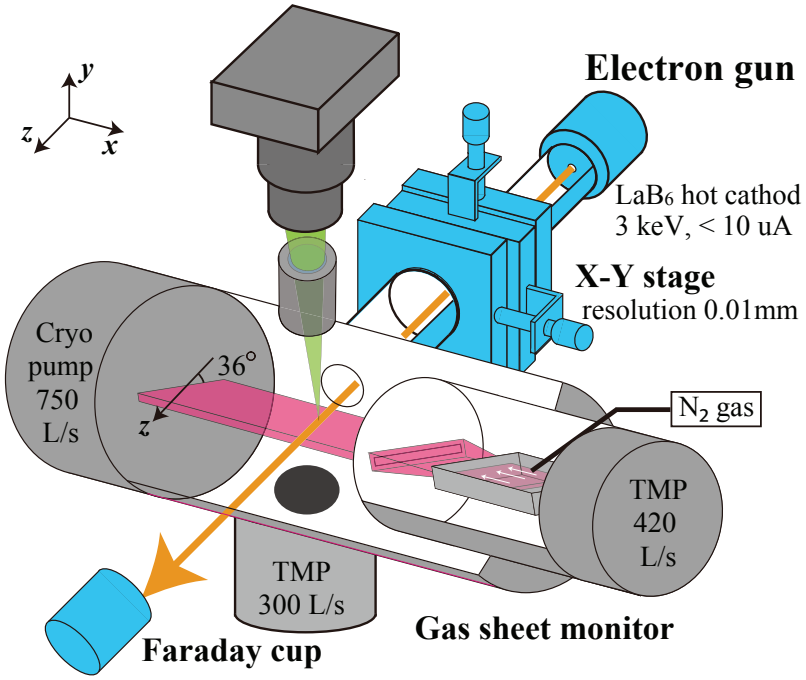

Figure 4.1: The response-function measurement system consists of the gas sheet monitor, an electron beam source, an X-Y stage, and a Faraday cup.

As described in Section 4.1, the response function should be ideally measured with a delta-function-like beam. The spatial profile of the electron beam performing the role of the delta-function-like beam has to be quantified to evaluate how the electron beam differs from the ideal delta function because the difference causes an error in reconstructing a high-intensity beam profile against the real profile. The electron beam profile is measured based on beam-gas interaction with the response-function-measurement system except some components. To eliminate the contributions of the response function from the obtained signal distribution, the image intensifier is removed and the gas sheet is not injected. The amplification-efficiency distribution of the image intensifier changes easily by injection of strong light, and cannot be approximated as uniform. The gas

density spatial distribution without the gas sheet injection can be approximated as uniform. The detection-efficiency spatial distribution of the CCD camera can be also approximated as uniform. The out-of-focus effect of the optical lens is ignorable when the object is placed around the focal point. Since the measured signal distributions did not change for a 2 mm scanning range along the y direction as shown in Fig. 4.2, the out-of-focus effect was assumed negligible. Thus, the electron beam profile measured with this apparatus can be regarded as a distribution which does not include the effect of the response function. The x profile can be directly measured with the response-function measurement system as shown in Fig. 4.1 but the y profile cannot be measured. In the pencil-electron-beam profile measurement, the cryopump was replaced with a viewport, and the photon detector system was moved in front of the viewport after the x profile measurement.

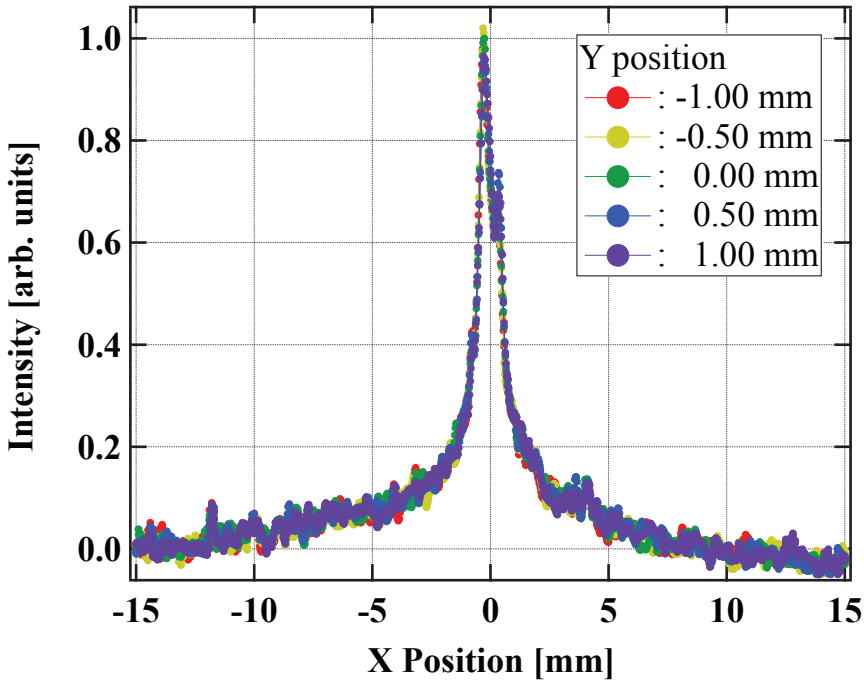

Figure 4.2: The comparison of the luminous intensity distributions of the captured image data for y direction scan of the electron beam position.

The projected profiles of the electron beam are shown in Fig. 4.3. Calibration of the horizontal axis from the image pixels to the physical length was conducted by scanning the electron beam position and comparing the signal peak position; 1.00 mm corresponds to 32.07 pixels and the standard deviation is 0.6075 pixels. The profiles

can be fitted with a triple-Gaussian function:

$$F_{x\,\mathrm{pen}}(x) = \exp\left(-\frac{x^2}{2\cdot(0.42\,\mathrm{mm})^2}\right) + 0.17\exp\left(-\frac{x^2}{2\cdot(2.0\,\mathrm{mm})^2}\right) + 0.071\exp\left(-\frac{x^2}{2\cdot(6.0\,\mathrm{mm})^2}\right) \tag{4.3}$$

$$F_{y\,\mathrm{pen}}(y) = \exp\left(-\frac{y^2}{2\cdot(0.22\,\mathrm{mm})^2}\right) + 0.28\exp\left(-\frac{y^2}{2\cdot(0.5\,\mathrm{mm})^2}\right) + 0.11\exp\left(-\frac{y^2}{2\cdot(2.8\,\mathrm{mm})^2}\right) \tag{4.4}$$

The effect of these electron beam profiles on the high-intensity-beam profile reconstruction will be discussed with the fitting function in Chapter 6.2.3.

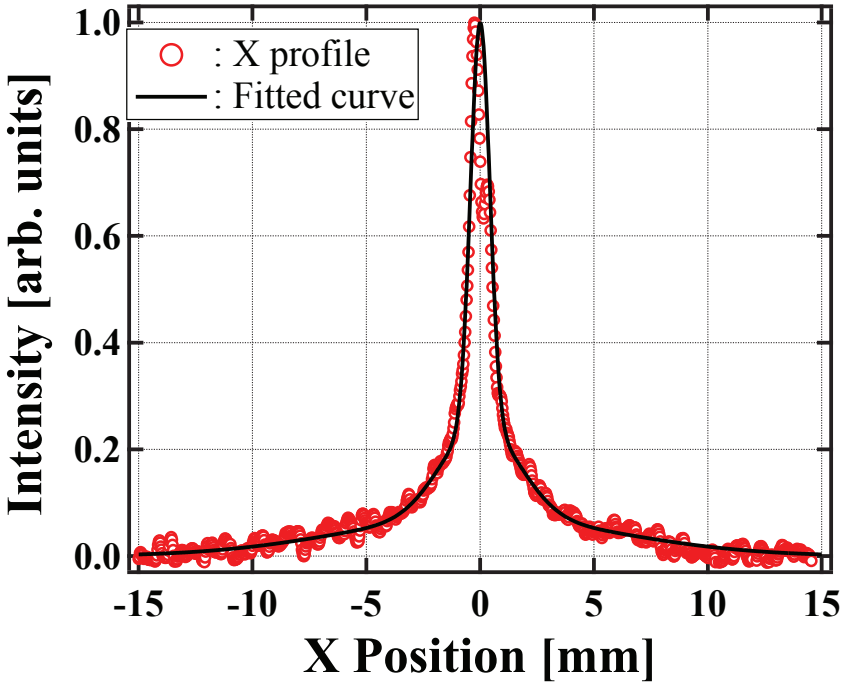

(a)

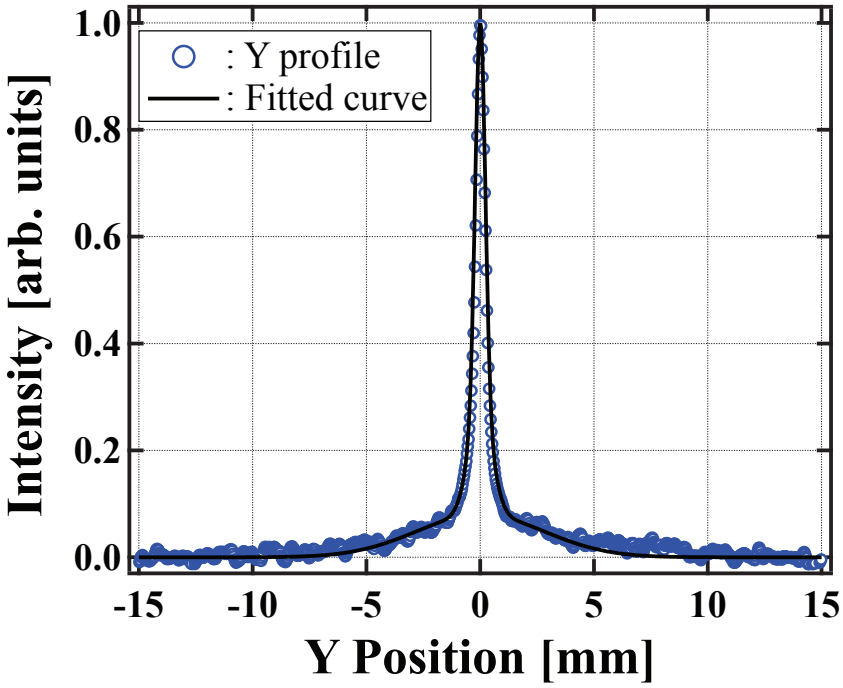

(b)

Figure 4.3: The projected profiles of the electron beam: (a) x profile and (b) y profile. The plots describe the measured data, and the lines describe the fitted curve with the triple-Gaussian function.

4.3 Four-dimensional response function

Examples of the image captured in the response-function measurement are shown in Fig. 4.4, and the projected intensity distribution along ν axis at the beam position $(x_0, y_0) = (0, 0)$ is shown in Fig. 4.5. The luminous intensity spatial distribution of each image corresponds to a part of the response function $T_{4D}(\mu, \nu; x_0, y_0)$. Each image is averaged over 10 frames, and the exposure time of the CCD camera for each frame is 120 s. Moving median filter and moving average filter for 5 $\times$ 5 pixels are applied to each frame for removing spike noise and smoothing. The 10-frame-averaged picture without gas sheet introduction as the background data is subtracted from the one with gas sheet introduction. For the pictures with the gas sheet, the gas-sheet-generator-inlet pressure was set to 100 Pa by considering the measurement efficiency although the pressure is considered to be out of the molecular flow region for the generator according to the conductance measurement result described in Chapter 3.2.4. The electron beam was scanned in 7 points with 1.50 mm intervals along x axis and 10 points with 2.00 mm intervals along y axis to construct the entire four-dimensional response function $T_{4D}(\mu, \nu; x, y)$. In the scan measurement process, the electron emission current was stable within $\pm$2.5% fluctuation and the inlet gas pressure was stable within $\pm$5% fluctuation. The total experiment time was over 100 hours to accomplish 70-point measurement. The white part in the images of Fig. 4.4 describes the photon signal produced by beam-gas interaction which can be separated into two components: the line-shape signal produced by the background gas and the center part signal produced by the gas sheet core. The photon-producing points move in the μ direction for the electron beam scan along the x axis and in the ν direction for the scan along the y axis due to the gas-sheet tilt as consistent with the intuitive understanding. Comparing the picture of Fig. 4.4f with the other pictures, the picture shows a broadening due to the y-direction scan which is the normal direction of the optical lens. This result indicates that the out-of-focus effect appears when a signal induced by a 10 mm-order thick high-intensity beam is captured as a 2-D image and this method measuring the response function can compensate the effect.

The 7 $\times$ 10 scan points are insufficient to conduct a numerical integration, which is required in the process to reconstruct a high-intensity beam profile. In general, numerical integration with good accuracy requires more than around 20 data points. The 7 $\times$ 10 data points are interpolated to 19 $\times$ 19 data points after smoothing with 10-pixel averaging and 2-D Fourier transform of $T_{4D}(\mu, \nu; x, y) \rightarrow \widehat{T}_{4D}(\xi, \zeta; x, y)$. An example of

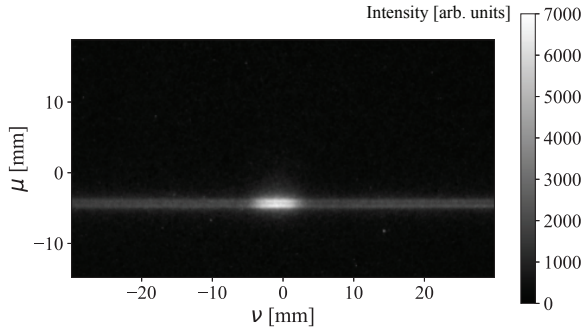

(a) (x_0, y_0) = (-4.5 mm, 0 mm)

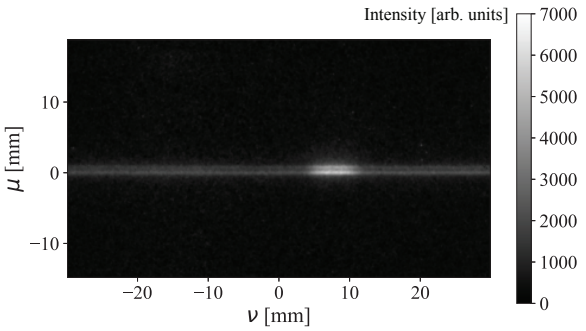

(d) (x_0, y_0) = (0 mm, 6 mm)

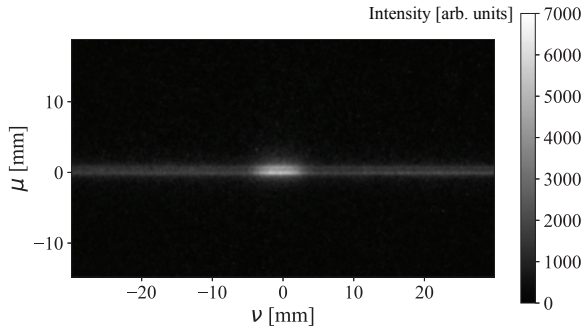

(b) (x_0, y_0) = (0 mm, 0 mm)

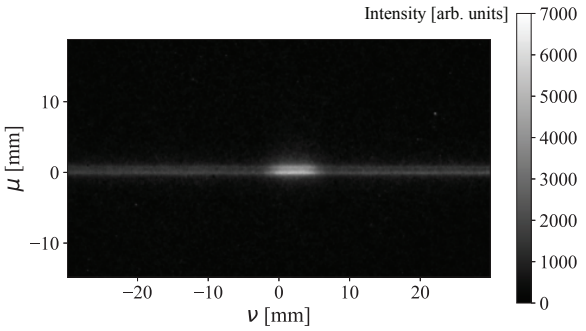

(e) (x_0, y_0) = (0 mm, 2 mm)

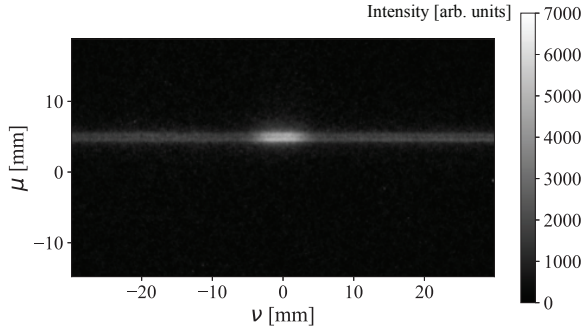

(c) (x_0, y_0) = (4.5 mm, 0 mm)

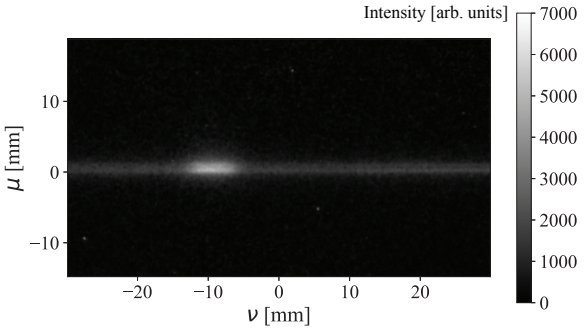

(f) (x_0, y_0) = (0 mm, -6 mm)

Figure 4.4: The captured images in the response function measurement: (a),(b),(c) x-direction scan and (d),(e),(f) y-direction scan. These images correspond to the response function $T_{4\mathrm{D}}(\mu, \nu; x_0, y_0)$.

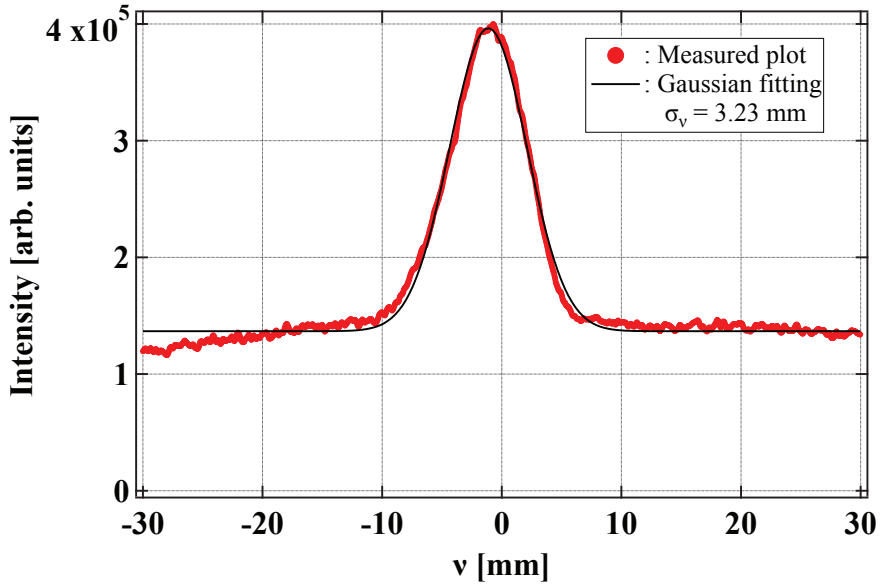

Figure 4.5: The projected luminous intensity distribution along ν axis at the beam position $(x_0, y_0) = (0, 0)$ can be fitted with a Gaussian of the deviation $\sigma_\nu = 3.23$ mm.

the 2-D Fourier transform of the response function $T_{4D}(\mu, \nu; 0, 0)$ is shown in Fig. 4.6. The intensities of the Fourier-transform coefficients outside the low frequency (low wave number) area marked by $(\xi_1, \xi_2, \zeta_1, \zeta_2)$ as shown in Fig. 4.6 are set to zero. Three kinds of conditions are considered; the condition 1 is defined as the no noise reduction condition, the condition 2 is defined as $(\xi_1, \xi_2, \zeta_1, \zeta_2) = (0.148, 1.60, 0.167, 0.418)$, and the condition 3 is defined as $(\xi_1, \xi_2, \zeta_1, \zeta_2) = (0.148, 0.445, 0.167, 0.418)$.

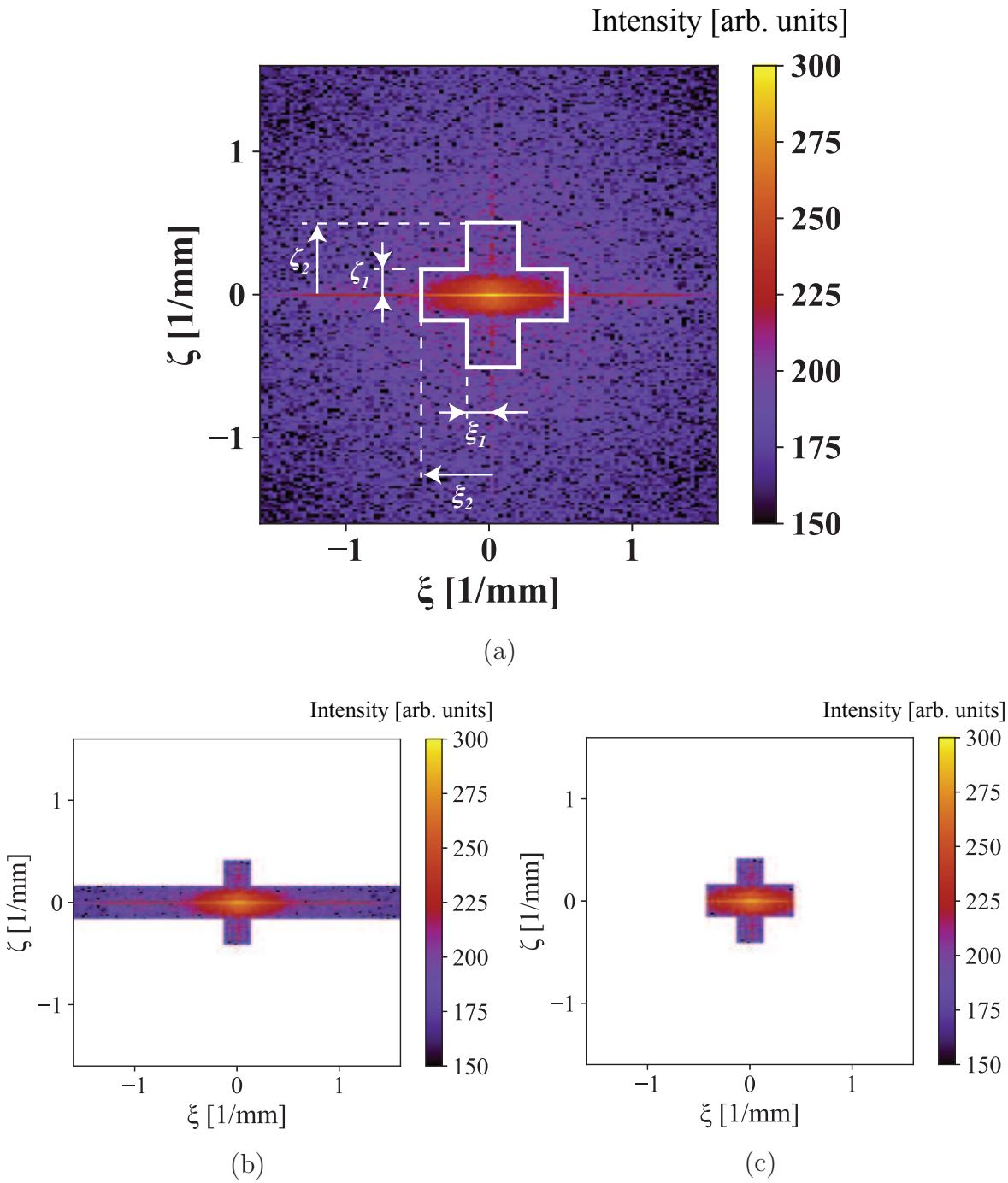

Figure 4.6: The frequency (wave number) space mapping $\widehat{T}_{4D}(\xi, \zeta; 0, 0)$ transformed from $T_{4D}(\mu, \nu; 0, 0)$ of Fig. 4.4b. The low frequency part surrounded by $(\xi_1, \xi_2, \zeta_1, \zeta_2)$ is extracted for noise reduction and smoothing. (a) the condition 1 is defined as the no noise reduction condition, (b) the condition 2 is defined as $(\xi_1, \xi_2, \zeta_1, \zeta_2) = (0.148, 1.60, 0.167, 0.418)$, and (c) the condition 3 is defined as $(\xi_1, \xi_2, \zeta_1, \zeta_2) = (0.148, 0.445, 0.167, 0.418)$.

4.4 Gas density spatial distribution measurement

The contribution of the gas density spatial distribution to the response function is considered to be dominant as compared with the other components, and the gas density distribution can be estimated by the response-function measurement. Evaluation of the gas density distribution is important to improve the gas sheet generator and properly analyze the gas sheet monitor's data. Since the dynamics of the gas molecules changes depending on the gas pressure as described in Chapter 2.1, the gas density spatial distribution (the velocity-distribution function) is affected by the gas pressure. If the gas density distribution changes in the main operational-gas-pressure region of the sheet generator, the response function measured at the different pressure from the high-intensity-beam profile measurement cannot be utilized for the profile reconstruction analysis. The dependance of the gas density distribution against the generator-inlet gas pressure was evaluated. The gas-sheet-tilt angle was changed to 90 degrees for measuring the gas density distribution along the sheet-thickness direction, and the image intensifier was removed to reduce the effect of the other components contributing the response function from the obtained data.

Figure 4.7 shows the cross-sectional luminous intensity distribution along the ν direction corresponding to the sheet-thickness direction at the inlet gas pressures of 0.1 Pa, 1.0 Pa, 10 Pa, 100 Pa, and 1.0 kPa. The full width at half maximum of the signal distribution against the inlet gas pressure is shown in Fig. 4.8. The gas-density spatial distribution broadens against increase of the inlet pressure, and the contrast between the peak intensity and the background intensity becomes smaller. These results indicate that intermolecular collisions are not negligible for the inlet gas pressure more than 0.2 Pa and the number of the collisions in the sheet generator increases depending on the inlet gas pressure. Since the full width at half maximum is constant at the inlet pressure more than 300 to 500 Pa, the intermolecular collisions are dominant to determine the gas flow, and this pressure range is classified as the viscous flow region. These results are consistent with the conductance measurement result described in Chapter 3.2.4; the effect of the intermolecular collisions appears from around 0.2 Pa and the gas flow model changes to the viscous flow around 300 Pa.

The signal intensity of the captured image is roughly calibrated into the gas pressure with the gas pressure gauge attached to the main chamber. Although the gauge does not measure the gas pressure on the electron beam line, the background gas distribution without the gas sheet injection is approximately uniform, and the gas pressure on

the beam line can be estimated with the gauge. To increase and control the uniform background gas pressure, the cryopump was stoped and the pumping speed of the TMP attached to the main chamber was changed by controlling the rotation speed. The calibrated peak gas pressure in the gas sheet against the inlet gas pressure is shown in Fig. 4.9. The calibration was conducted by separating the gas pressure range into four regions by changing the exposure time of the CCD camera because a higher gas pressure induces saturation of the CCD camera. The inlet pressure of 100 Pa corresponding to the pressure of the response function measurement described in Section 4.3 produces the gas sheet having the 2×10^{-4} Pa peak pressure. In the low inlet pressure region less than 1 Pa, the gas sheet pressure slowly increases against a rise in the inlet pressure. This result implies that the fully collisionless region exists at the inlet pressure less than 0.1 Pa. The result is consistent with the observation by Ogiwara *et al.* who measured the gas sheet density and reported that the linear-increase region of the gas density exists before the region where the gas-density increase ratio reduces [23]. In conclusion, the main operational-gas-pressure region is not in the collisionless flow region for this gas sheet generator. A transition-region gas flow model should be employed, and the response function requires to be measured for each generator-inlet gas pressure.

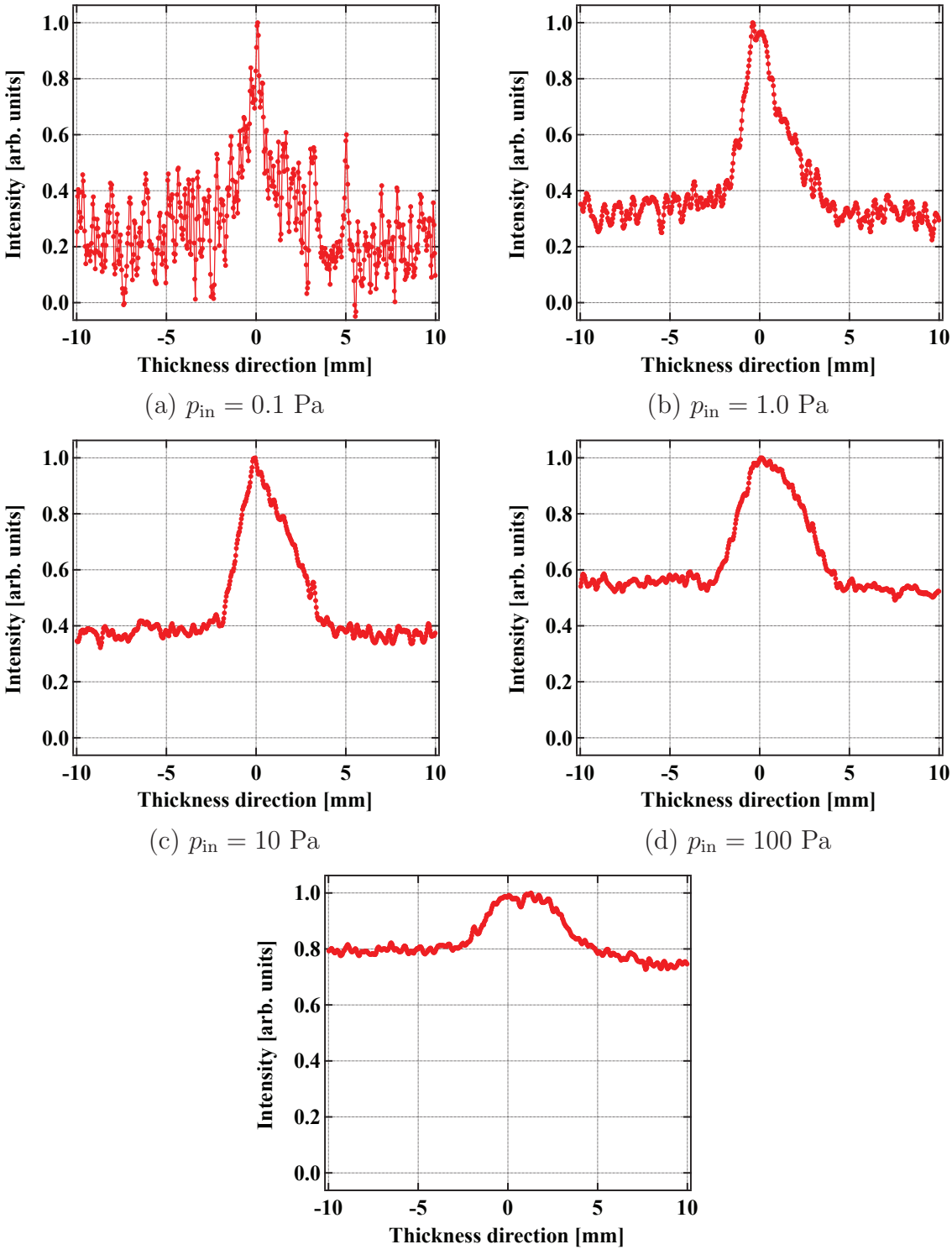

(a) $p_{\mathrm{in}} = 0.1$ Pa

(b) $p_{\mathrm{in}} = 1.0$ Pa

(c) $p_{\mathrm{in}} = 10$ Pa

(d) $p_{\mathrm{in}} = 100$ Pa

(e) $p_{\mathrm{in}} = 1.0$ kPa

Figure 4.7: The gas density spatial distributions along the sheet-thickness direction against the inlet pressure of (a) 0.1 Pa, (b) 1.0 Pa, (c) 10 Pa, (d) 100 Pa, and (e) 1.0 kPa. The intensities are normalized by each peak intensity.

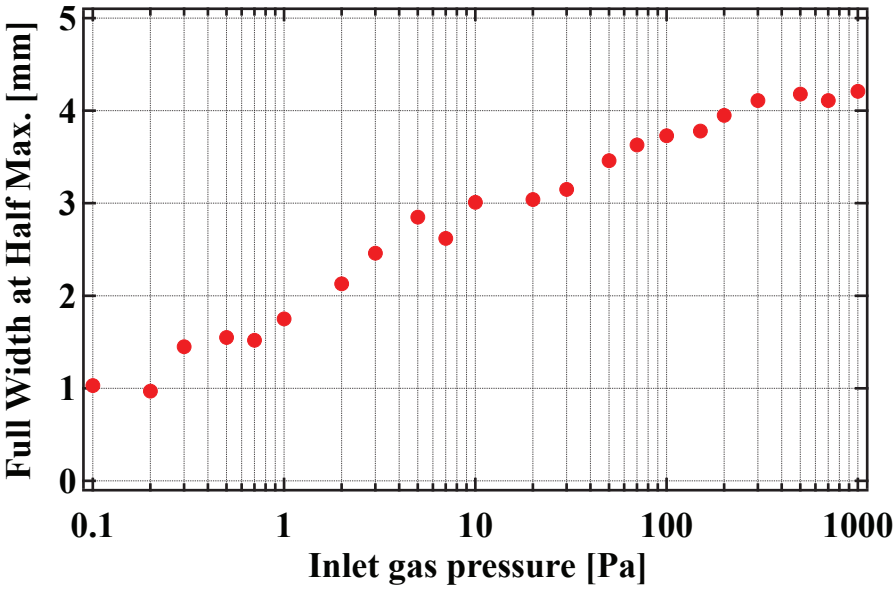

Figure 4.8: The full width at half maximum of the gas density distribution along the sheet-thickness direction against the inlet pressure.

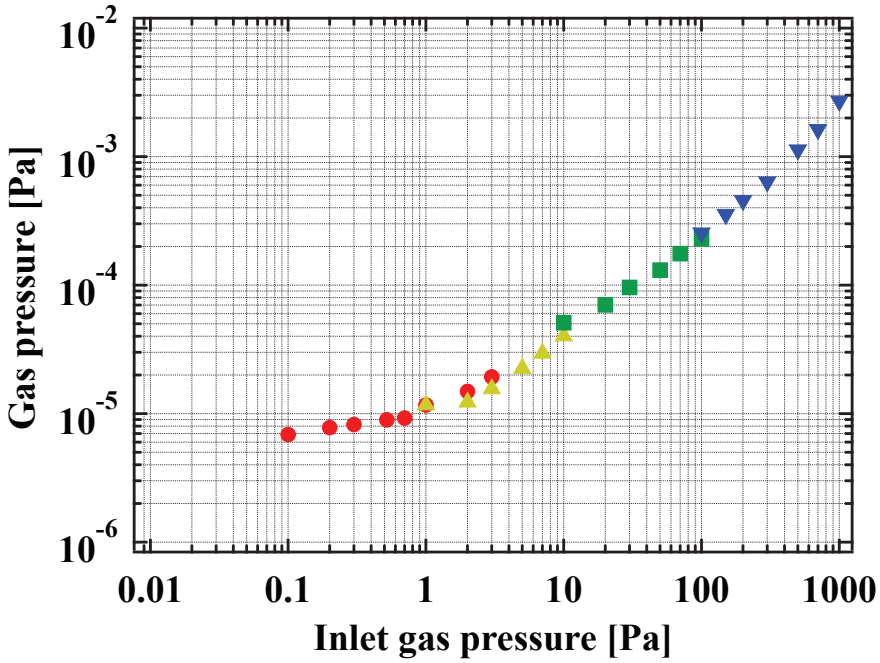

Figure 4.9: The calibrated peak pressure in the gas sheet against the inlet gas pressure. The calibration was conducted by separating the gas pressure range into four regions by changing the exposure time of the CCD camera because a higher gas pressure induces saturation of the CCD camera.

References

[23] N. Ogiwara, Y. Hori, I. Yamada, Y. Hikichi, J. Kamiya, and M. Kinsho, in *Proceedings of the International Particle Accelerator Conference IPAC2019*, (Melbourne, Australia, 2019), WEPGW037.

Chapter 5

High Intensity Beam Profile Measurement

To demonstrate the effectiveness of the gas sheet monitor, a high-intensity, low-energy beam profile was measured at the J-PARC RFQ test stand which is the spare system for the J-PARC Linac from the ion source to 3 MeV beam line [37, 38]. In this chapter, the RFQ test stand is introduced, and the result of the J-PARC high-intensity beam profile measurement is described.

5.1 J-PARC RFQ test stand

5.1.1 Constituent of beam line

Figure 5.1 shows the conponents of the RFQ test stand, and Table 5.1 describes the parameters of the beam operation. The 50 keV negative hydrogen ion beam is extracted from the ion source and enters the radio-frequency quadrupole (RFQ) linear accelerator through the two solenoid-type focusing magnets. The RFQ accelerates the H^- beam from 50 keV to 3 MeV and bunches the beam in the longitudinal (time) direction. The beam is transported for about 1.6 m with three focusing quadrupole magnets. The bending magnet can deflect the beam trajectory by 11 degrees. The beam current is measured with the current transformers and the Faraday cups. The beam profile is measured with the wire-scanner monitor placed between the first and the second quadrupole magnets. In the medium-energy-beam-transport (MEBT) chamber, a double-slit-type emittance monitor is placed to measure the phase space distribution of the beam. The gas sheet monitor is placed between the second and the third quadrupole magnets and

is replaced with another wire-scanner monitor after the gas sheet monitor's studies to compare the obtained beam profiles between the two methods.

Table 5.1: The typical parameters of J-PARC RFQ test stand.

Beam species	H^-
Beam energy	3 MeV
Resonant freqency(RFQ)	324 MHz
Peak beam current	55∼60 mA
Pulse length	50 μs
	(1.7 $\times 10^{13}$ protons per pulse)
Repetition rate	up to 25 Hz
transverse RMS beam size	2∼3 mm
transverse RMS emittance	0.3π mm·mrad (normalized)

Figure 5.2 shows the double-slit-type emittance monitor. In a multi-particle system like the beam, the phase space distribution of the system is indispensable to express the beam condition. To measure the velocity vectors and the positions of the beam particles, the emittance monitor consists of a first slit and a Faraday cup with an entrance slit. The first slit determines the measurement position, and the Faraday cup measures the velocity vectors in the scan direction. The measured current intensity of each position and velocity constructs the 2-D phase space of x-v_x or y-v_y by scanning the slit and the Faraday cup. The emittance is defined as the area of the ellipse which is the fitting curve of the measured phase space. This type of monitor is a destructive one and can be utilized only in a test stand.

Figure 5.3 shows how a wire-scanner monitor measures the beam profile. The monitor inserts a metal or a carbon-nanotubes wire in the beam line and records the electrical current on the wire induced by beam-wire interaction. In the case of H^- beam measurement, the wire current is mainly composed of the electrons detached from the H^- beam. Scanning the wire and comparing the wire current realize the 1-D projected beam profile measurement in x and y directions shown in the figure. This type of monitor cannot be utilized for a high-intensity, low-energy beam measurement because the wire breaks due to the energy deposition. When the beam profile is measured with the wire-scanner monitor, the beam pulse length is shortened to 50 μs against the actual operational beam duration of up to 500 μs to reduce the heat load.

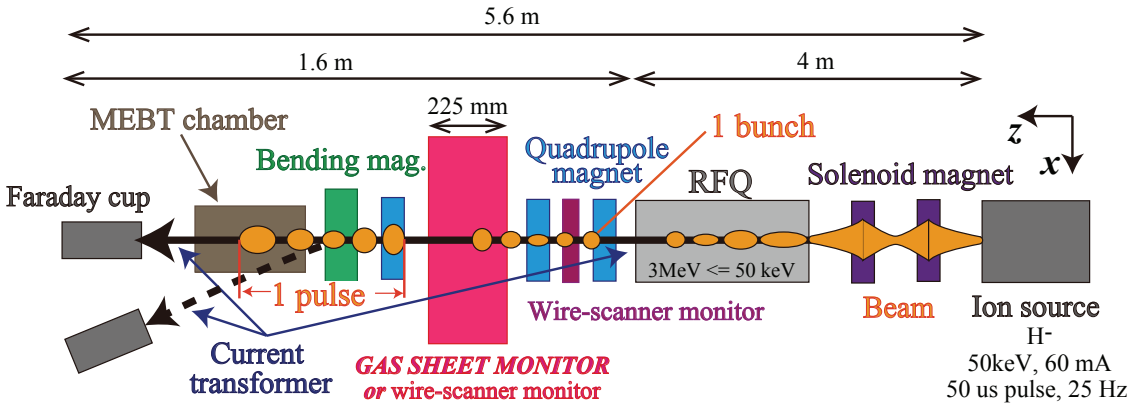

(a)

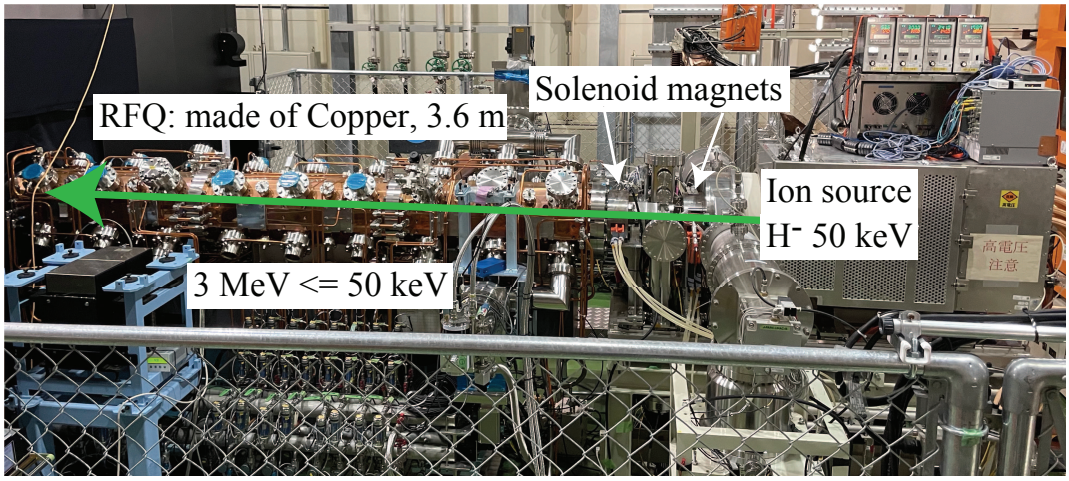

(b)

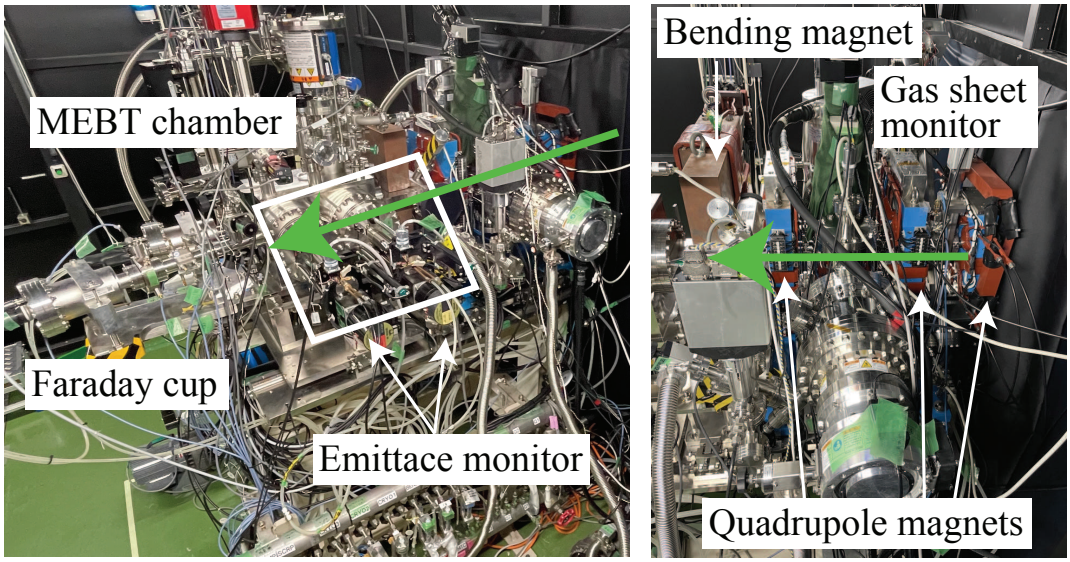

(c)

Figure 5.1: The RFQ test stand beam line: (a) a schematic diagram and (b)(c) photos.

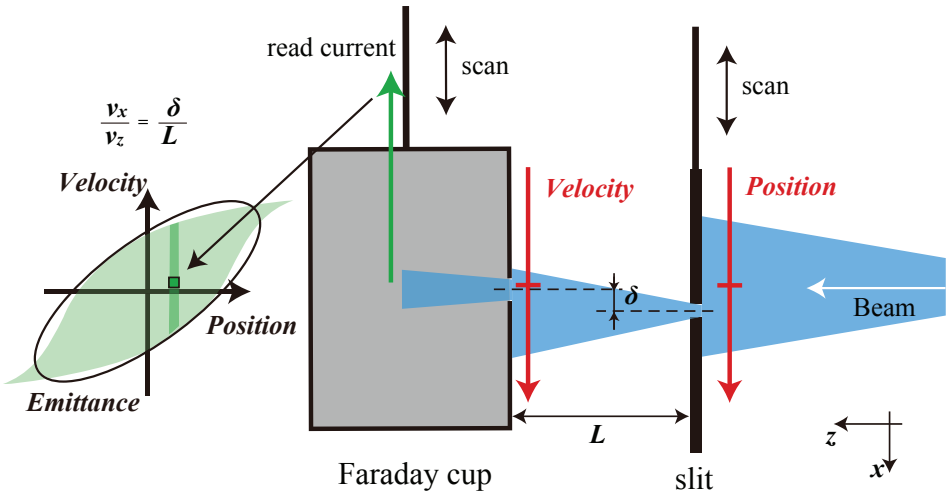

Figure 5.2: The double-slit-type emittance monitor. The first slit determines the measurement position, and the Faraday cup determines the measurement velocity. The read current intensity of each position and velocity constructs the phase space 2-D distribution. The emittance is defined as the area of the ellipse which is the fitting curve of the measured phase space.

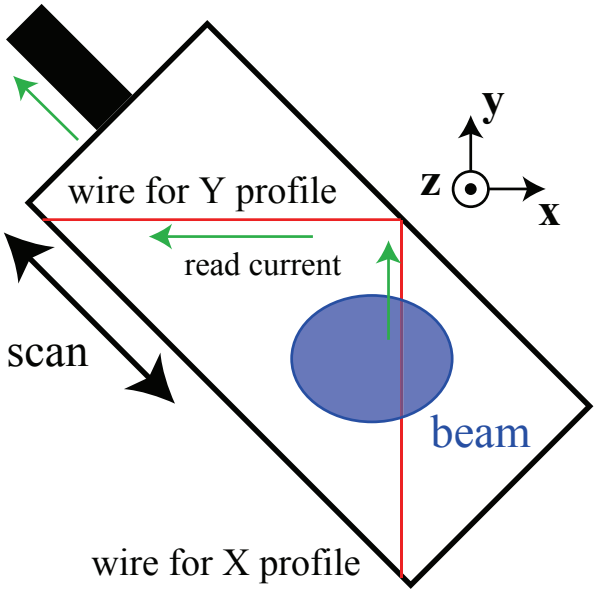

Figure 5.3: The wire-scanner monitor. Scanning the wire position constructs the 1-D projected beam profile with the read current.

5.1.2 Envelope-equation-based beam simulation

To control the focusing-magnet parameters for avoiding a beam loss, the beam trajectory estimation is important, and the beam envelope equation is often utilized to obtain a rough idea how the beam expands along the trajectory. From the equation of motion, the beam-orbital equation for linear focusing systems along $s = v_z t$ axis which is introduced instead of z, the coordinate representing the beam axis, is described as

$$\frac{\mathrm{d}^2 x}{\mathrm{d}s^2} + k(s)\, x = 0 \tag{5.1}$$

where $k(s)$ describes the focusing strength for a linear force. When $k(s)$ is constant against s and $k(s) = k_0$, the general solution can be written as

$$x = a\cos(\sqrt{k_0}\, s + \psi_0) \tag{5.2}$$

where a, ψ_0 are constants. To find a solution for a general $k(s)$, the constant a and $\sqrt{k_0}\, s$ are rewritten as $a(s)$ and $\psi(s)$, and the following identity can be obtained by applying the solution into the orbital equation:

$$\left\{a''(s) - a(s)\psi'^2(s) + k(s)\, a(s)\right\}\, \cos(\psi + \psi_0) + \left\{-2a'(s)\psi'(s) - a(s)\psi''(s)\right\}\, \sin(\psi + \psi_0) = 0 \tag{5.3}$$

$$\Rightarrow \begin{cases} a''(s) - a(s)\psi'^2(s) + k(s)\, a(s) = 0 & (5.4) \\ -2a'(s)\psi'(s) - a(s)\psi''(s) = 0 & (5.5) \end{cases}$$

where the prime symbol describes derivative with respect to s. From Eq. (5.5), the following constant ε is introduced,

$$\left\{a^2(s)\, \psi'(s)\right\}' = 0 \tag{5.6}$$

$$\Rightarrow a^2(s)\, \psi'(s) = \varepsilon. \tag{5.7}$$

Equation (5.4) can be rewritten as follows with Eq. (5.7):

$$a''(s) + k(s)\, a(s) - \frac{\varepsilon^2}{a^3(s)} = 0. \tag{5.8}$$

Thus, the solution of Eq (5.1) is

$$x = a(s)\ \cos(\psi(s) + \psi_0) \tag{5.9}$$

$$x' = \sqrt{a'^2(s) + \frac{\varepsilon^2}{a^2(s)}}\ \sin(\psi(s) + \psi_1) \tag{5.10}$$

where ψ_1 is a constant and $a(s)$ satisfies Eq. (5.8) which describes the envelope trajectory determined by the focusing systems $k(s)$ and the initial beam condition ε. The solutions (5.9), (5.10) describe an ellipse in the phase space,

$$\gamma(s)x^2 + 2\alpha(s)xx' + \beta(s)x'^2 = \varepsilon \tag{5.11}$$

where $\alpha(s), \beta(s), \gamma(s)$ are called the Twiss parameters and the constant ε called the Courant-Snyder invariant or emittance describes the area of the ellipse [43, 44]. The correlations between the Twiss parameters with $a(s)$ are as follows:

$$\beta(s) = \frac{a^2(s)}{\varepsilon} \tag{5.12}$$

$$\alpha(s) = -\frac{\beta'(s)}{2} \tag{5.13}$$

$$\gamma(s) = \frac{1 + \varepsilon\alpha^2(s)}{\beta(s)}. \tag{5.14}$$

The beam trajectory in the RFQ test stand is estimated by solving Eq. (5.8). Considering the linear term of the space charge force which is an indispensable component for a high-intensity beam analysis, the envelope equation Eq. (5.8) can be rewritten as follows by separating it into x and y directions:

$$\begin{aligned} X''_{\mathrm{rms}}(s) + \left\{ k(s) - \frac{K_{\mathrm{sc}}}{X_{\mathrm{rms}}(s)(X_{\mathrm{rms}}(s) + Y_{\mathrm{rms}}(s))} \right\} X_{\mathrm{rms}}(s) - \frac{\varepsilon^2}{X^3_{\mathrm{rms}}(s)} = 0 \\ Y''_{\mathrm{rms}}(s) + \left\{ k(s) - \frac{K_{\mathrm{sc}}}{Y_{\mathrm{rms}}(s)(X_{\mathrm{rms}}(s) + Y_{\mathrm{rms}}(s))} \right\} Y_{\mathrm{rms}}(s) - \frac{\varepsilon^2}{Y^3_{\mathrm{rms}}(s)} = 0. \end{aligned} \tag{5.15}$$

where $X_{\mathrm{rms}}, Y_{\mathrm{rms}}$ introduced instead of a describe the root mean square size of the beam profile and K_{sc} is the perveance describing the linear term of the space charge force [43, 44]. The perveance for the beam assumed as a Gaussian shape in the transverse directions and a uniform profile in the longitudinal direction can be found by solving the Poisson's equation:

$$K_{\mathrm{sc}} = \frac{qI}{4\pi\epsilon_0\ f_{\mathrm{RF}}\ \sigma_t} \tag{5.16}$$

where ϵ_0 is the permittivity of vacuum, q is the charge of the beam particles, I is the beam current, f_{RF} is the acceleration frequency, and the σ_t is the characteristic length in longitudinal converted to the position space length. The initial conditions for solving the equations (5.15) are determined using the phase space distributions measured with the emittance monitor. The longitudinal parameter σ_t cannot be measured in the present system of the RFQ test stand, and is estimated to fit the solution of the envelope equation to the spatial beam profile measured with the wire-scanner monitor placed between the first and the second quadrupole magnets.

Figure 5.4 shows the simulated beam envelope against s for the typical parameters of the focusing magnets $k(s)$. The front end $s = 0$ of the simulation region corresponds to the RFQ exit. At the gas sheet monitor's position, the rms beam sizes are estimated as 2.2 mm and 3.2 mm in the x and y directions, respectively. The strength of the each quadrupole magnet can be controlled for the beam not to strike the beam pipe with the envelope simulation because the tail part of the beam spatial distribution typically extends up to 5 times of the rms size.

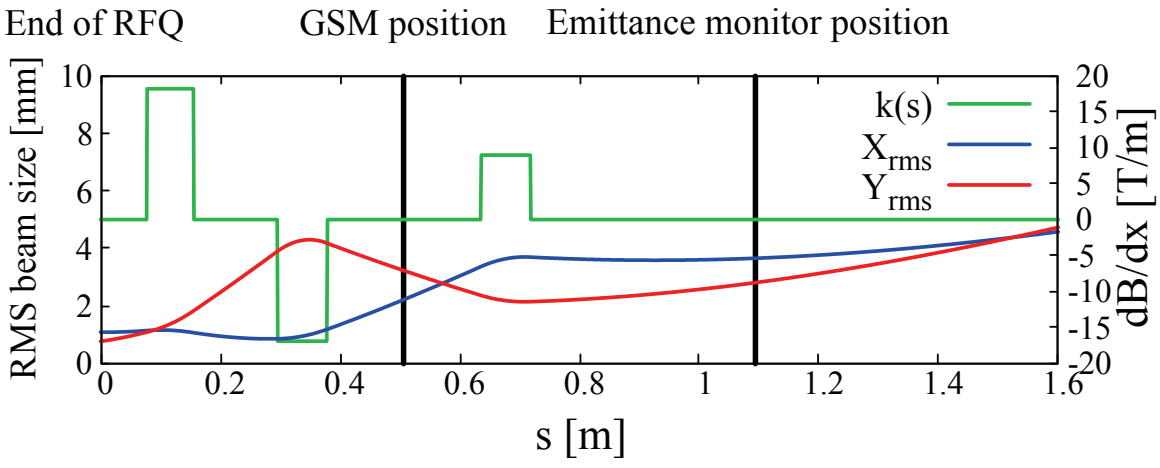

Figure 5.4: The beam envelope against s for the typical parameters of the focusing magnets $k(s)$. The position $s = 0$ corresponds to the exit of the RFQ. The positions of the gas sheet monitor (GSM) and the emittance monitor are described. At the GSM position, the rms beam sizes are 2.2 mm and 3.2 mm in the x and y directions, respectively.

5.2 Beam profile measurement

5.2.1 Captured image

The raw data for beam profile measurement obtained with the gas sheet monitor is shown in Fig. 5.5. The luminous intensity spatial distribution of the image corresponds to $g(\mu, \nu)$ in Eq. (2.20) of Chapter 2.2. The focusing-magnet parameters are the typical ones used for the envelope simulation shown in Fig. 5.4. The exposure time of the CCD camera was 20 s, and the gate width and the gate delay of the image intensifier were 10 μs and 35 μs from the beam-pulse head as shown in Fig. 5.6, respectively. The photon signal is averaged with 40,000 beam pulses (= 20 s $\times$ 25 Hz $\times$ 80 frames) corresponding to 1.5 $\times$ 10^{17} H^- particles. The gas-sheet-generator inlet pressure was 100 Pa which is the same condition as the response function measurement. The gas pressures at the cover chamber, the main chamber, the MEBT chamber, and the RFQ against the gas-sheet-generator inlet pressure are shown in Fig. 5.7. The locations for defining the respective gas pressure and the respective gas flux are shown in Fig. 5.8. The gas pressures at the cover chamber and the main chamber are almost same as the measurement result at the off-line setup shown in Chapter 3.2.4 and Fig. 3.12. The gas-density spatial distribution in the main chamber is considered to be same in both measurements. The background subtraction, moving median filter, and moving average filter are applied with the same conditions as Fig. 4.4. At the center part, the two-dimensional beam profile can be recognized. However, the luminous intensity spatial distribution does not directly corresponds to the beam profile due to the signal produced by the background gas. A proper analysis method to reconstruct the beam profile from the image based on the profile measurement principle described in Chapter 2.2 is required. The profile reconstruction will be discussed in Chapter 6.

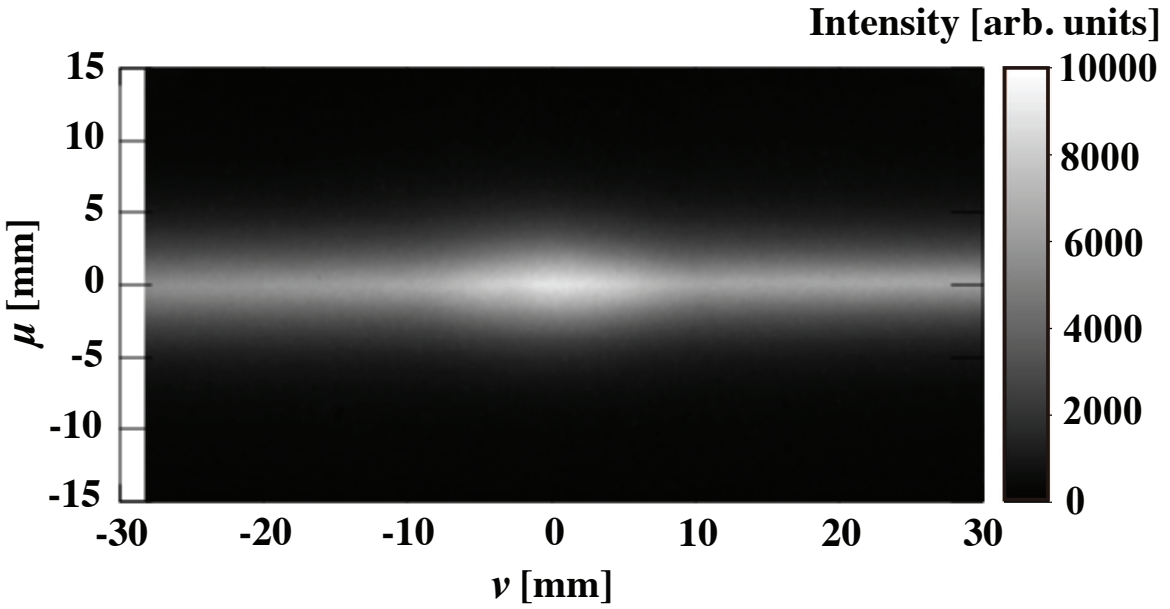

(a)

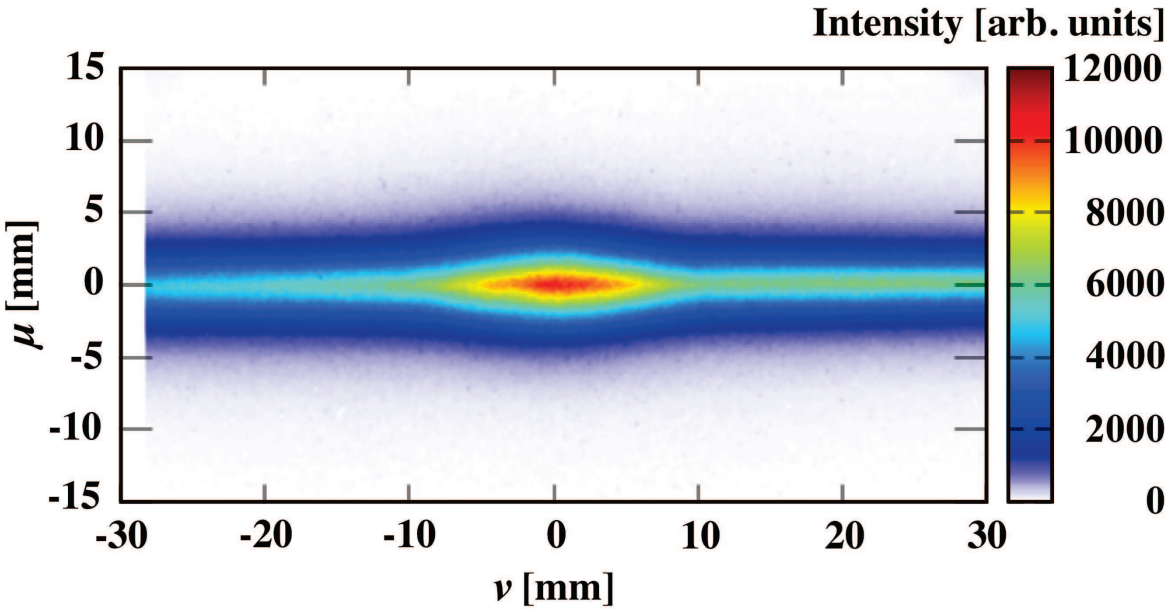

(b)

Figure 5.5: The captured image by the high-intensity beam profile measurement at the J-PARC RFQ test stand: (a) gray scale contour plot and (b) color contour plot. This two-dimensional spatial distribution corresponds to $g(\mu, \nu)$ in Eq. (2.20)

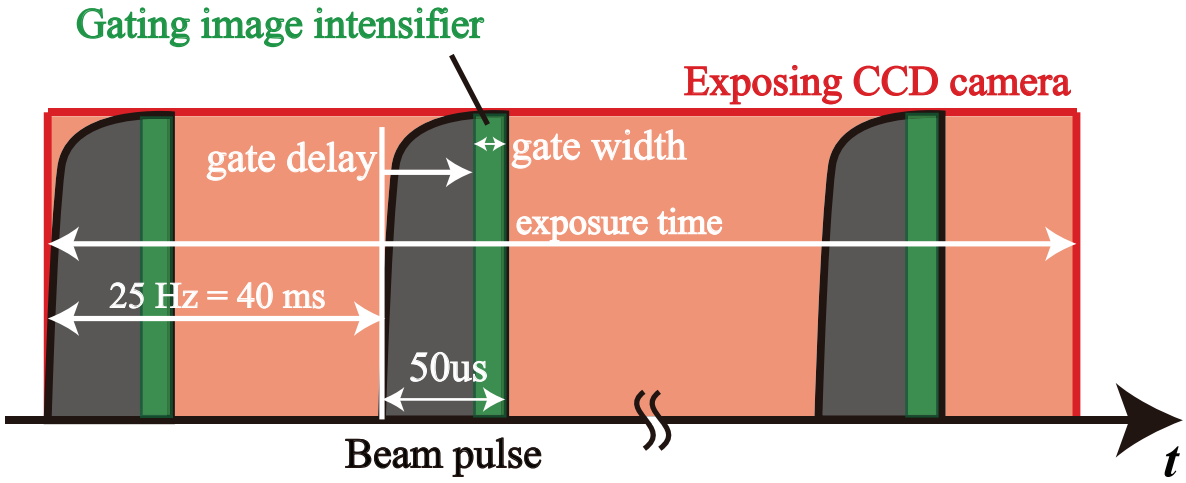

Figure 5.6: The time structure of the beam pulse, the image intensifier gate, and the CCD camera exposure.

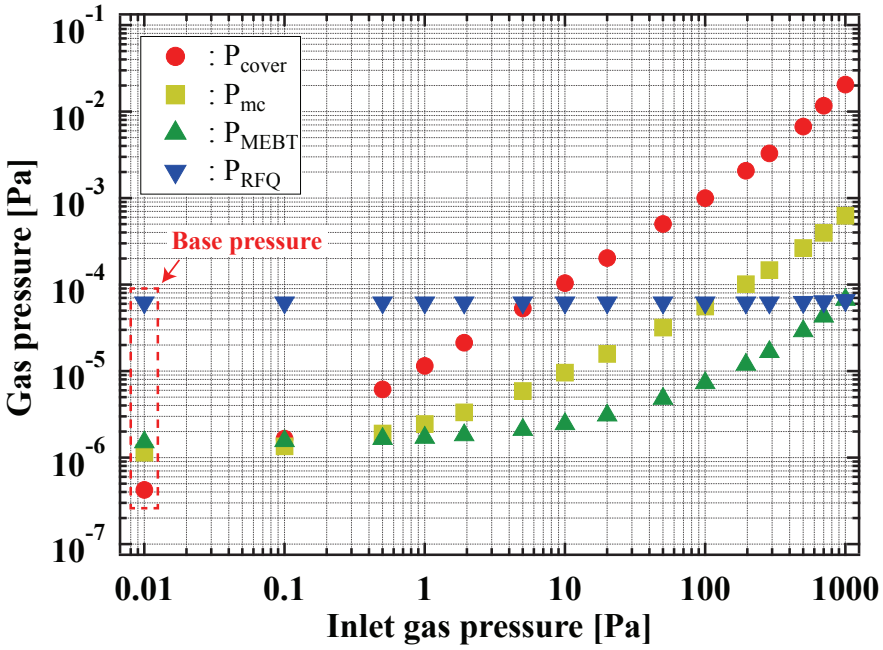

(a)

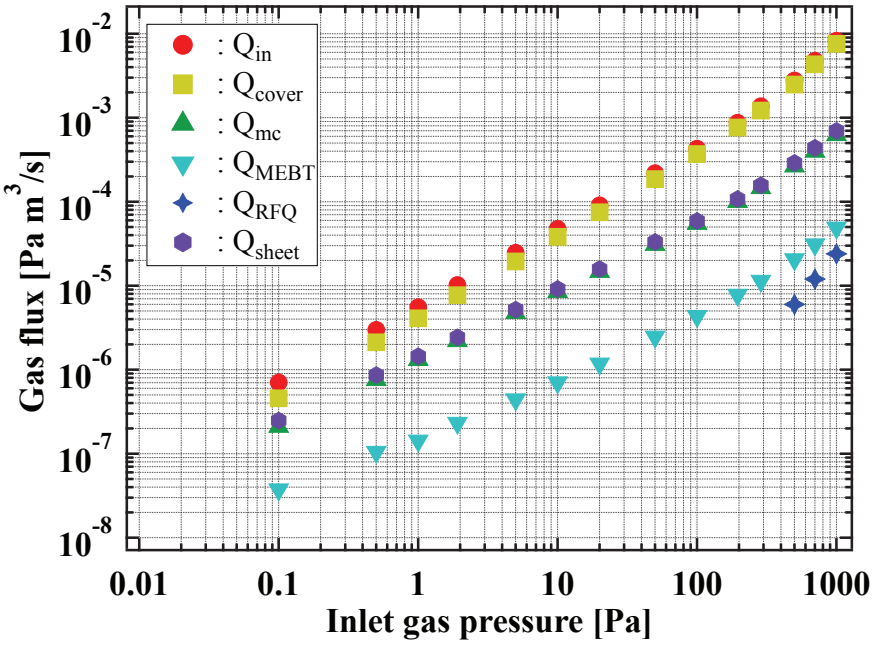

(b)

Figure 5.7: (a) The gas pressures and (b) the gas fluxes at the cover chamber, the main chamber, the MEBT chamber, and the RFQ against the sheet generator inlet pressure.

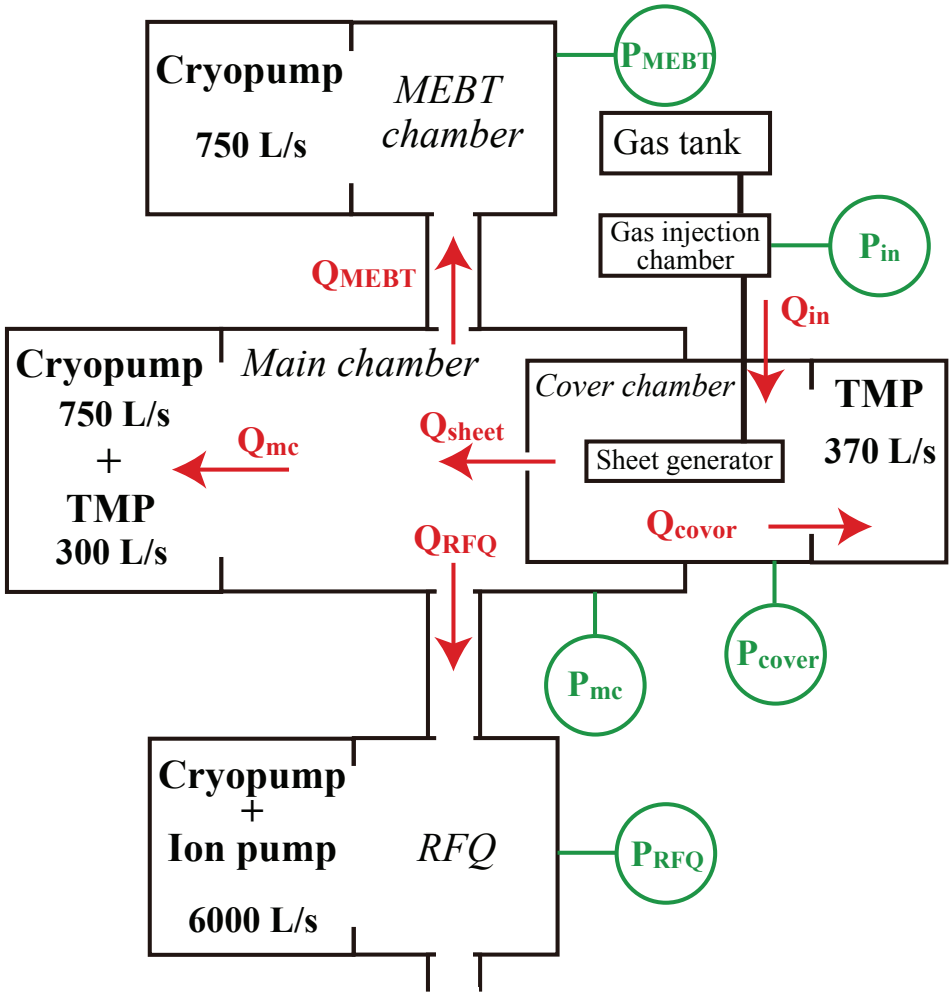

Figure 5.8: The locations where the gas pressures and the gas fluxes are defined with respect to the cover chamber, the main chamber, the MEBT chamber, and the RFQ.

5.2.2 Inlet pressure dependance of captured image

One important parameter of the gas sheet monitor to measure a beam profile is the gas-sheet-generator inlet pressure. A high gas-sheet density enables a high signal-to-noise ratio or a high speed measurement, and a low gas-sheet density realizes a minimum invasive measurement. The dependance of the captured image distribution on the inlet pressure is evaluated to clarify the possibilities.

Figure 5.9 shows the captured images with the inlet pressures of 0.1 Pa, 1 Pa, 10 Pa, 100 Pa, and 1.0 kPa. The exposure time, the gate width, the gate delay, and the number of averaging frames are shown in Table 5.2. Figure 5.10 shows the cross-sectional luminous intensity spatial distributions of each image shown in Fig. 5.9. The distributions in both the x and y directions become broad against an increase in the inlet pressure. This result is consistent with the gas density distribution measurement result shown in Chapter 4.4, and indicates that the profile reconstruction analysis for each inlet pressure is required. If the beam profile can be reconstructed independently of the inlet gas pressure, the gas sheet monitor can be utilized in the wide gas pressure range depending on the measurement purpose or the measurement environment. Particularly for 0.1 Pa injection, the beam profile can be measured with little influence on the beam-line gas pressure according to Fig. 5.7a.

Table 5.2: The measurement conditions of the sheet-generator inlet pressure, the gate width/delay of the image intensifier, the CCD camera exposure time, and the number of averaging frames.

inlet pressure	I.I. gate width	I.I. gate delay	Exposure time	averaging frame
0.1 Pa	50 μs	0 μs	200 s	30 frames
1.0 Pa	50 μs	0 μs	200 s	30 frames
10 Pa	50 μs	0 μs	250 s	10 frames
100 Pa	50 μs	0 μs	50 s	10 frames
1.0 kPa	50 μs	0 μs	5 s	100 frames

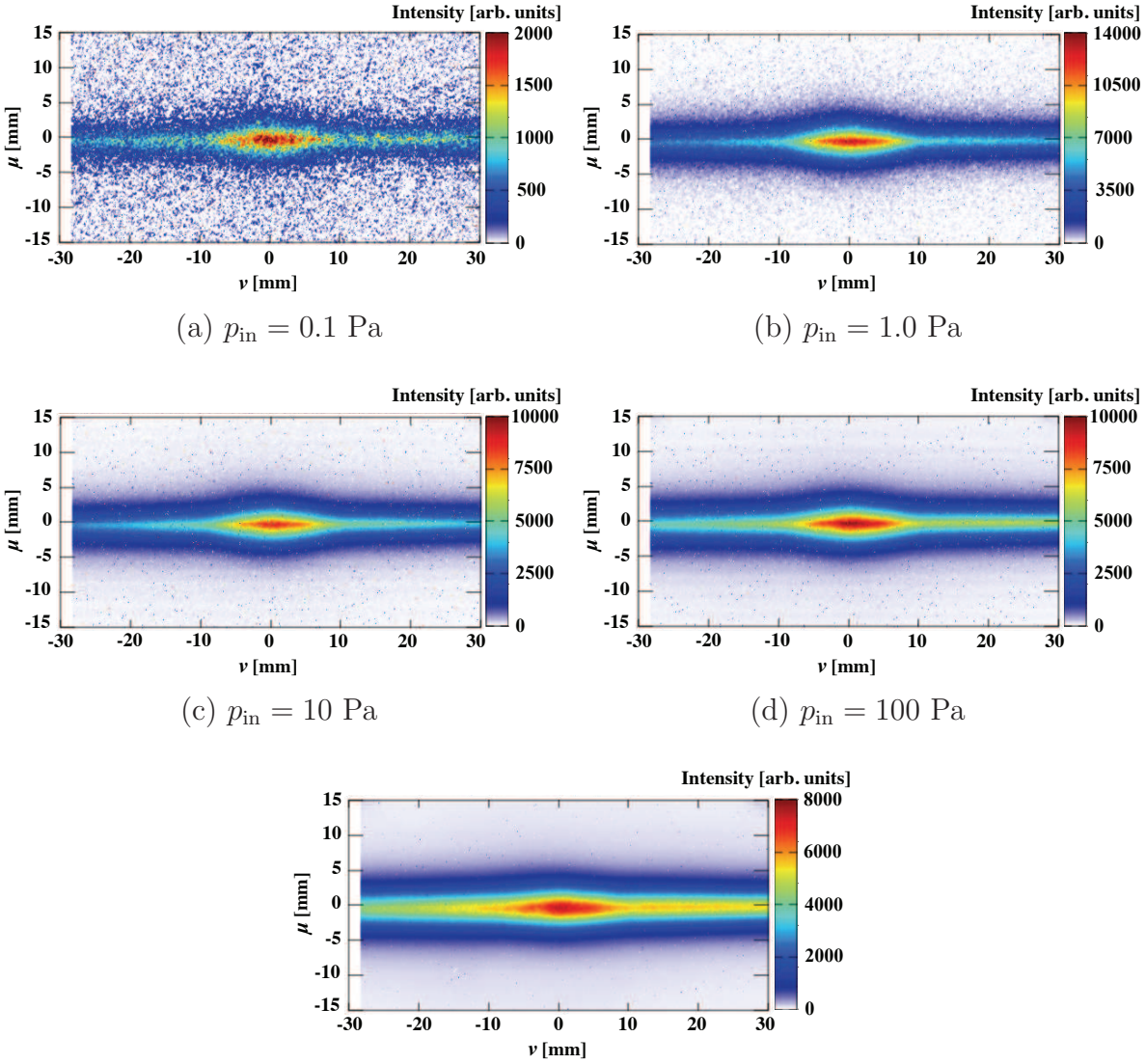

(a) $p_{\mathrm{in}} = 0.1$ Pa

(b) $p_{\mathrm{in}} = 1.0$ Pa

(c) $p_{\mathrm{in}} = 10$ Pa

(d) $p_{\mathrm{in}} = 100$ Pa

(e) $p_{\mathrm{in}} = 1.0$ kPa

Figure 5.9: The captured images of the high-intensity H^- beam measurement at the inlet pressure of (a) 0.1 Pa, (b) 1.0 Pa, (c) 10 Pa, (d) 100 Pa, and (e) 1.0 kPa.

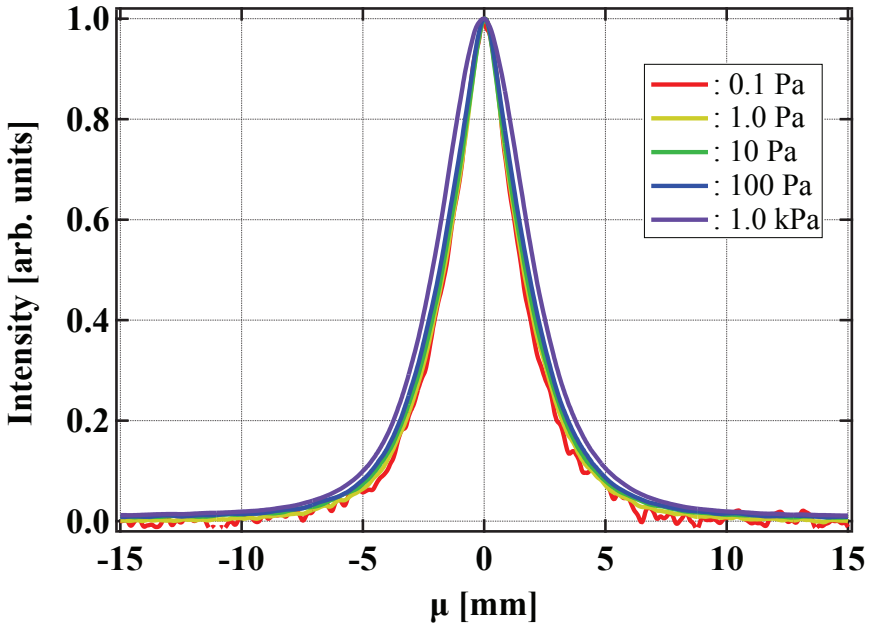

(a)

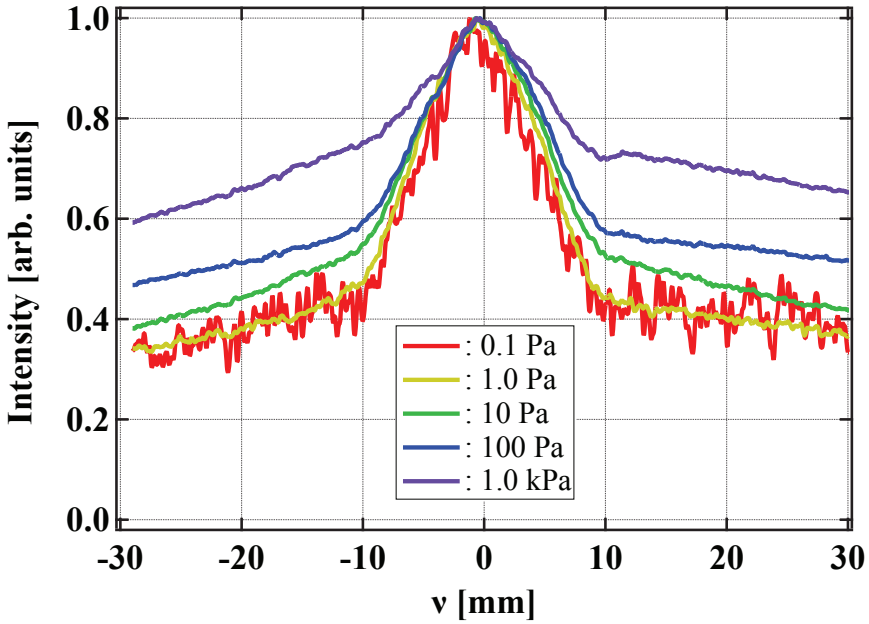

(b)

Figure 5.10: The cross-sectional luminous intensity spatial distributions against the inlet pressure (a) along μ axis and (b) along ν axis. The intensities are normalized by each peak intensity.

5.2.3 High-speed measurement

Another important parameter of the gas sheet monitor is the number of averaging the beam pulses. The wire-scanner monitor which is an ordinary profile monitor requires about 100 beam pulses to construct x and y profiles for wire-position scanning process. On the other hand, the gas sheet monitor has a potential to measure a 2-D beam profile with only one pulse because of the imaging detection.

Figure 5.11 shows the captured images averaged with 1, 5, 10, and 100 pulses at the inlet pressure of 1.0 kPa. Figure 5.12 shows the projected luminous intensity spatial distributions of Fig. 5.11. The CCD camera exposure time was 1 ms, and the image intensifier gate width and delay were 50 μs and 0 μs, respectively. The beam-induced signal distributions constructed by one pulse can be recognized. In the J-PARC accelerator operation, the maximum pulse length is 500 μs of duty 0.5 corresponding to 5 pulses of the 50 μs RFQ-test-stand beam, and the 5-pulse-averaging signal constructs clearer distributions. This result indicates that the gas sheet monitor has the possibility of the shot-by-shot constant monitoring which serves to detect anomalies of the beam conditions and stop the beam operation.

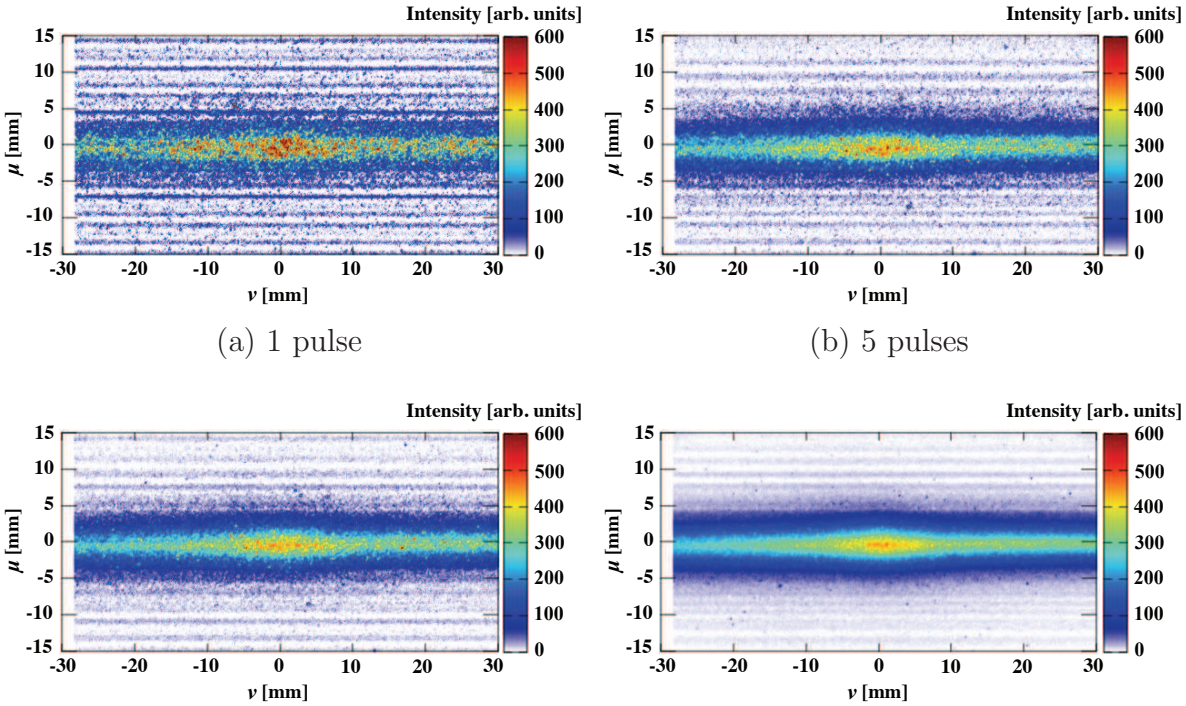

(a) 1 pulse (b) 5 pulses

(c) 10 pulses (d) 100 pulses

Figure 5.11: The captured images averaged with (a) 1 pulse, (b) 5 pulses, (c) 10 pluses, and (d) 100 pulses at the inlet pressure of 1.0 kPa

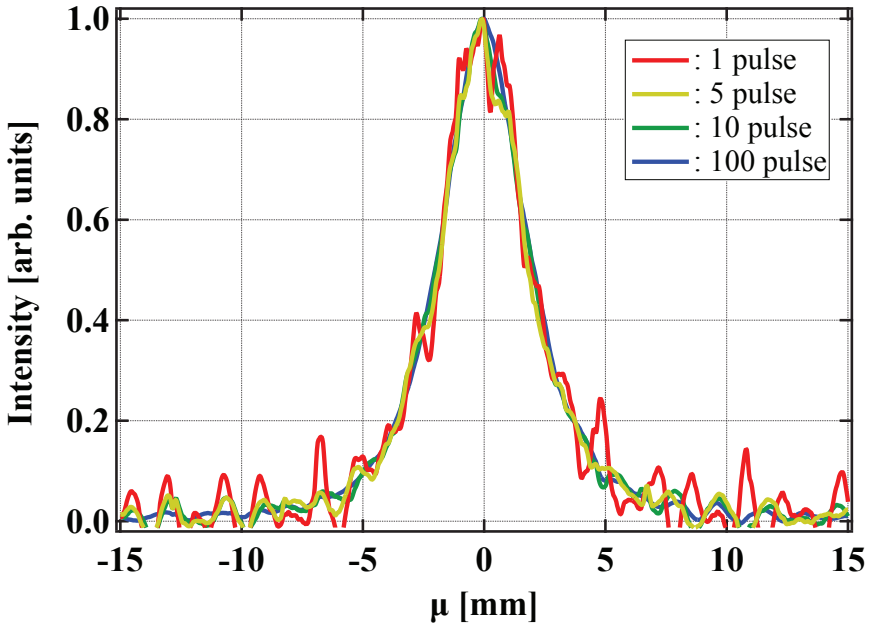

(a)

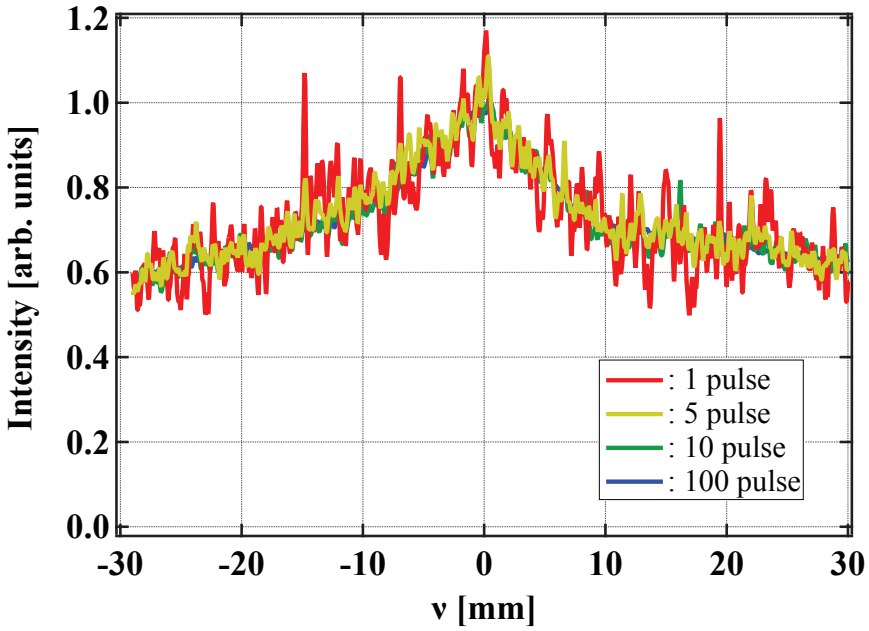

(b)

Figure 5.12: The projected luminous intensity distributions of the images shown in Fig. 5.11 (a) along μ axis and (b) along ν axis. The intensities are normalized by each peak intensity

References

[37] Y. Kondo, T. Morishita, S. Yamazaki, T. Hori, Y. Sawabe, E. Chishiro, S. Fukuta, K. Hasegawa, K. Hirano, N. Kikuzawa, I. Koizumi, A. Miura, H. Oguri, K. Ohkoshi, F. Sato, S. Shinozaki, A. Ueno, H. Kawamata, T. Sugimura, A. Takagi, Z. Fang, Y. Fukui, K. Futatsukawa, K. Ikegami, T. Maruta, T. Miyao, and K. Nanmo, "Beam test of a new radio frequency quadrupole linac for the Japan Proton Accelerator Research Complex", Phys. Rev. ST Accel. Beams **17**, 120101 (2014).

[38] Y. Kondo, T. Morishita, K. Hirano, T. Ito, N. Kikuzawa, R. Kitamura, H. Oguri, K. Ohkoshi, S. Shinozaki, K. Shinto, Z. Fang, Y. Fukui, K. Futatsukawa, K. Ikegami, T. Miyao, K. Nanmo, M. Otani, T. Shibata, T. Hori, Y. Nemoto, Y. Sato, F. Kobayashi, D. Takahashi, R. Tasaki, Y. Ito, Y. Kato, T. Ishiyama, and Y. Sawabe, "Upgrade of the 3-MeV Linac for testing of accelerator components at J-PARC", Journal of Physics: Conference Series **1350**, 012077 (2019).

[43] M. Reiser, *Theory and Design of Charged Particle Beams* (WILEY-VCH, 2008).

[44] H. Weidemann, *Particle Accelerator Physics* (Springer, 2015).

Chapter 6

Beam Profile Reconstruction

The principle of beam profile measurement using the gas sheet monitor is described in Chapter 2.2 as that the luminous intensity spatial distribution of the obtained image $g(\mu, \nu)$ is correlated with the beam profile $F(x, y; z)$ though the integral equation Eq. (2.20):

$$g(\mu, \nu) = \int T(\mu, \nu; x, y, z)\ F(x, y; z)\ \mathrm{d}^3x \tag{2.20}$$

where $T(\mu, \nu; x, y, z)$ describes the response function of the gas sheet monitor. In this chapter, two kinds of the profile reconstruction methods and their mathematical formulations based on the integral equation are described: the simplified method and the exact method.

6.1 Simplified method

6.1.1 Method to reconstruct beam profile

The simplified reconstruction method approximates the response function of the gas sheet monitor as an ideal gas sheet described as a delta function and ignores the other factors such as the gas density spatial distribution, the efficiency spatial distribution of the photon detector, and the point-spread effects:

$$T(\mu, \nu; x, y, z) = \delta(\mu - x)\ \delta(\nu - z)\ \delta(y - z\tan\theta) \tag{6.1}$$

where θ means the gas-sheet-tilt angle with respect to the beam axis. The former two delta functions indicate the change of coordinate, and the latter delta function indicates the gas sheet of an infinite density without the thickness. Applying this

response function to the integral equation Eq. (2.20) gives the direct relation between the image and the beam profile:

$$\begin{aligned} g(\mu,\nu) &= \int \delta(\mu - x)\,\delta(\nu - z)\,\delta(y - z\tan\theta)\,F(x,y;z)\,\mathrm{d}^3x \\ &= F(\mu,\nu\tan\theta;\nu). \end{aligned} \tag{6.2}$$

This formula means that the luminous intensity distribution of the obtained image is constructed by the change of coordinate $\nu\tan\theta \to \nu$ on the beam profile. Thus, the transverse beam profile can be reconstructed by transforming the ν axis of the obtained image into $\nu\tan\theta$ and regarding the image distribution in $(\mu,\nu\tan\theta)$ coordinate as a distribution in the (x,y) coordinate since the $(\mu,\nu\tan\theta)$ space directly corresponds to the (x,y) space through the delta functions. However, the luminous intensity distribution of the obtained image along ν direction includes the z dependance of the transverse beam profile, and this effect induces an error in the reconstructed profile with this method.

6.1.2 Error estimation

The reconstructed beam profile using the simplified method does not necessarily reproduce the real profile as it ignores the effect due to the response function, in particular the gas density spatial distribution. In this section, an error in the reconstructed profile against the real profile is evaluated by assuming the beam profile to be an analytical (Gaussian) function.

The real response function is defined as follows to reflect the gas density spatial distribution which is the dominant contribution,

$$T(\mu,\nu;x,y,z) = \delta(\mu - x)\,\delta(\nu - z)\,\left\{(1 - T_0)\exp\left(-\frac{\{z - y/\tan\theta\}^2}{2{\sigma_{gz}}^2}\right) + T_0\right\}. \tag{6.3}$$

The angle θ describes the gas sheet tilt with respect to the beam axis of z and is set to 36°. The real high-intensity-beam profile is defined as Gaussian:

$$F(x,y) = \exp\left(-\frac{x^2}{2{\sigma_{bx}}^2} - \frac{y^2}{2{\sigma_{by}}^2}\right). \tag{6.4}$$

The image function $g(\mu, \nu)$ can be calculated analytically by Eq. (2.20)

$$g(\mu,\nu) = \int T(\mu,\nu;x,y)\ F(x,y;z)\ \mathrm{d}^3x \tag{2.20}$$

$$= \exp\left(-\frac{\mu^2}{2{\sigma_{bx}}^2}\right)\ \left\{(1-T_0)\sqrt{2\pi}\frac{\sigma_{gz}\sigma_{by}}{\sigma_\nu}\exp\left(-\frac{\nu^2}{2{\sigma_\nu}^2}\right) + T_0\sqrt{2\pi}\sigma_{by}\right\} \tag{6.5}$$

where $\sigma_\nu = \sqrt{\left(\frac{\sigma_{by}}{\tan\theta}\right)^2 + \sigma_{gz}^2}$.

Since the information of the beam profile is represented by the Gaussian distribution part, the reconstructed profile described as $\widetilde{F}$ in the (μ, ν) space can be regarded as

$$g(\mu,\nu) \propto \widetilde{F}(\mu,\nu) = \exp\left(-\frac{\mu^2}{2{\sigma_{bx}}^2}\right)\ \exp\left(-\frac{\nu^2}{2{\sigma_\nu}^2}\right). \tag{6.6}$$

The beam profile reconstruction by the simplified method is the change of variables: $\nu \to \nu\tan\theta$,

$$\widetilde{F}(\mu,\nu\tan\theta) = \exp\left(-\frac{\mu^2}{2{\sigma_{bx}}^2}\right)\ \exp\left(-\frac{(\nu\tan\theta)^2}{2(\sigma_\nu\tan\theta)^2}\right). \tag{6.7}$$

Therefore, the reconstructed beam profile is defined in the (x, y) space as follows:

$$\widetilde{F}(x,y) = \exp\left(-\frac{x^2}{2{\widetilde{\sigma}_{bx}}^2}\right)\ \exp\left(-\frac{y^2}{2{\widetilde{\sigma}_{by}}^2}\right) \tag{6.8}$$

$$\widetilde{\sigma}_{bx} = \sigma_{bx} \tag{6.9}$$

$$\widetilde{\sigma}_{by} = \sqrt{\sigma_{by}^2 + (\sigma_{gz}\tan\theta)^2}. \tag{6.10}$$

This result indicates that the x profile corresponds to the beam profile independent of the gas density spatial distribution and the y profile become thicker depending the gas sheet thickness. An error in the beam profile is defined as the deviation ratio of the Gaussian distributions:

$$\text{Error} = \frac{\widetilde{\sigma}_{by} - \sigma_{by}}{\sigma_{by}} \tag{6.11}$$

$$= \sqrt{\tan^2\theta\left(\frac{\sigma_{gz}}{\sigma_{by}}\right)^2 + 1} - 1. \tag{6.12}$$

Figure 6.1 shows the error of the reconstructed profile against the gas sheet thickness normalized by the real beam profile in the y direction. The gas sheet thinner than 20%

of the beam profile yields the error less than 1%. In the present case that the gas sheet thickness and the beam profile are estimated to be 3.23 mm from the response function measurement result and 3.2 mm from the envelope beam simulation result respectively, the error is estimated as 24.0%; the reconstructed beam profile is 24.0% broader than the real profile.

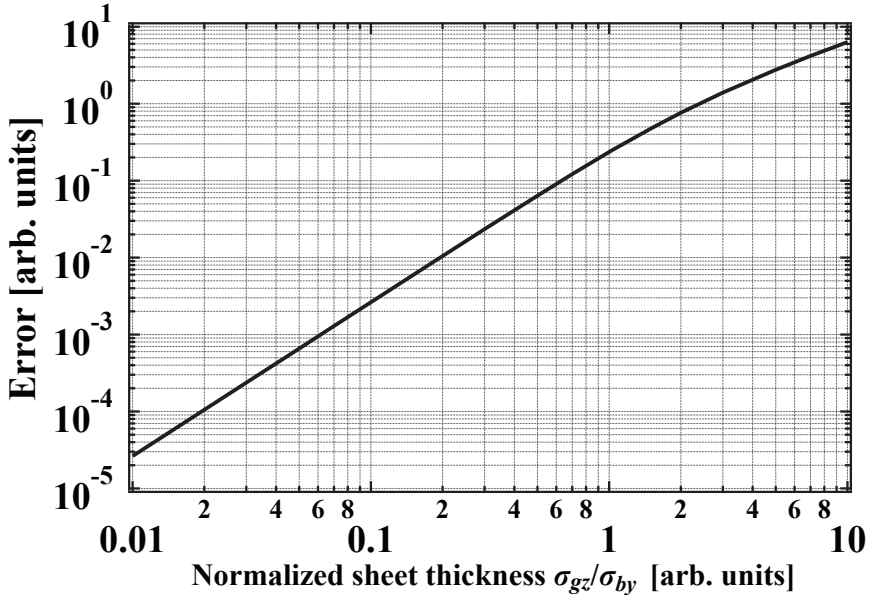

Figure 6.1: The error in the reconstructed profile to the real profile against the normalized gas density thickness by the beam profile.

6.1.3 J-PARC H^- beam reconstruction

The beam profile reconstruction with the simplified method is performed using the J-PARC beam measurement result, and the reconstructed profile is evaluated by comparing it with the profile measured by the wire-scanner monitor. The image obtained by the J-PARC beam profile measurement and its cross-sectional and projected luminous intensity distributions are shown in Fig. 6.2. The H^- beam conditions were 55 mA beam current, 50 μs pulse length and 25 Hz repetition. The inlet gas pressure was 100 Pa. The exposure time of the CCD camera was 50 s with the 50 μs image intensifier gate width, and the 40 pictures are utilized for averaging. The cross-sectional and projected distributions of Fig. 6.2 almost agree in both μ and ν directions. The profile reconstruction will be performed with the projected distributions. While the x profile directly corresponds to the intensity distribution along μ axis, the y profile reconstruction needs the following simple analysis. The tail part of the ν distribution

are not constant, and the Gaussian part needs to be extracted from the distribution by eliminating the tail part. Since the tail part can be fitted by a linear function, the profile end positions are defined as $\nu = -14.3$ mm, 20.7 mm where the slope changes from the fitted line as shown in Fig. 6.3. The average of the intensities at the profile end positions is defined as the constant base intensity which is 0.52 and is subtracted. The change of coordinate by multiplying $\tan\theta$ gives the y profile. The reconstructed x and y profiles are shown in Fig. 6.4 and are compared with the ones measured by the wire-scanner monitor. The root mean squares (RMS) of the profiles are described in Table 6.1. The reconstructed profiles of both directions are broader than the ones measured by the wire-scanner monitor due to ignoring the response function. For x profile, the point-spread effects are considered to make the profile broader. For y profile, the gas density spatial distribution as well as the point-spread effects make the profile thicker as estimated in the previous section.

Table 6.1: Comparison of the RMS values obtained by the gas sheet monitor(GSM) and the wire scanner monitor(WSM).

	GSM [mm]	WSM [mm]	difference
x profile	3.15	2.26	31.3 %
y profile	3.78	3.16	19.6 %

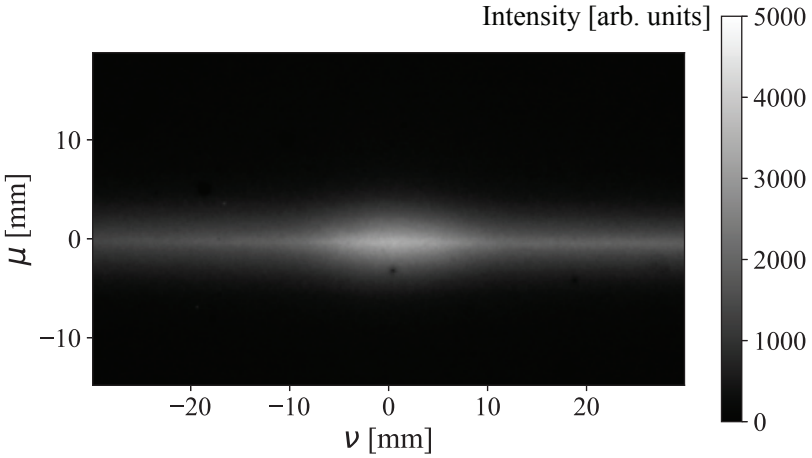

(a)

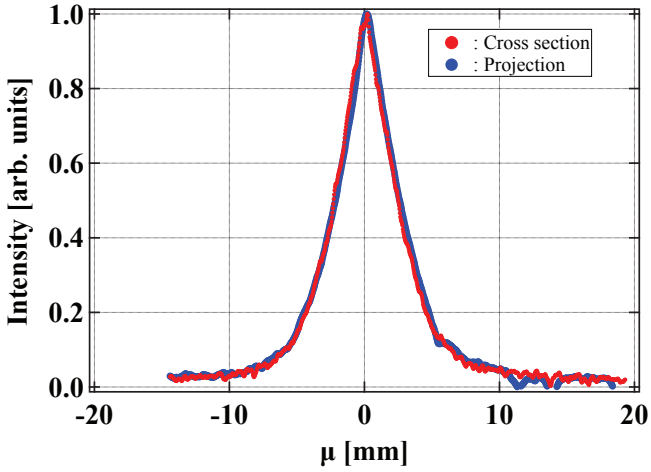

(b)

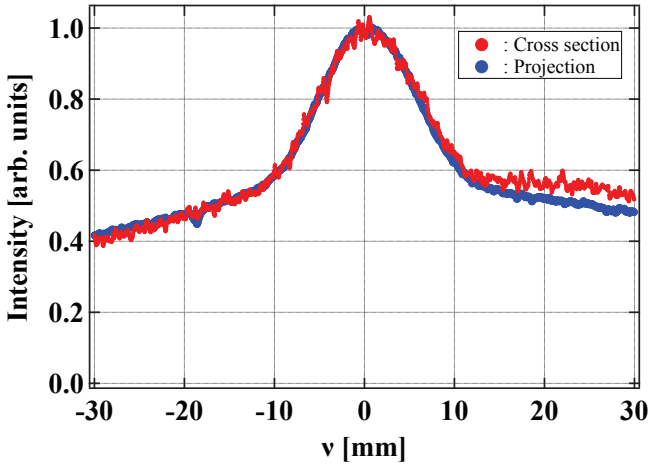

(c)

Figure 6.2: The obtained luminous intensity spatial distribution by J-PARC H^- beam profile measurement: (a) the 2-D image, (b)(c) the cross-sectional and the projected distributions along μ axis and ν axis, respectively.

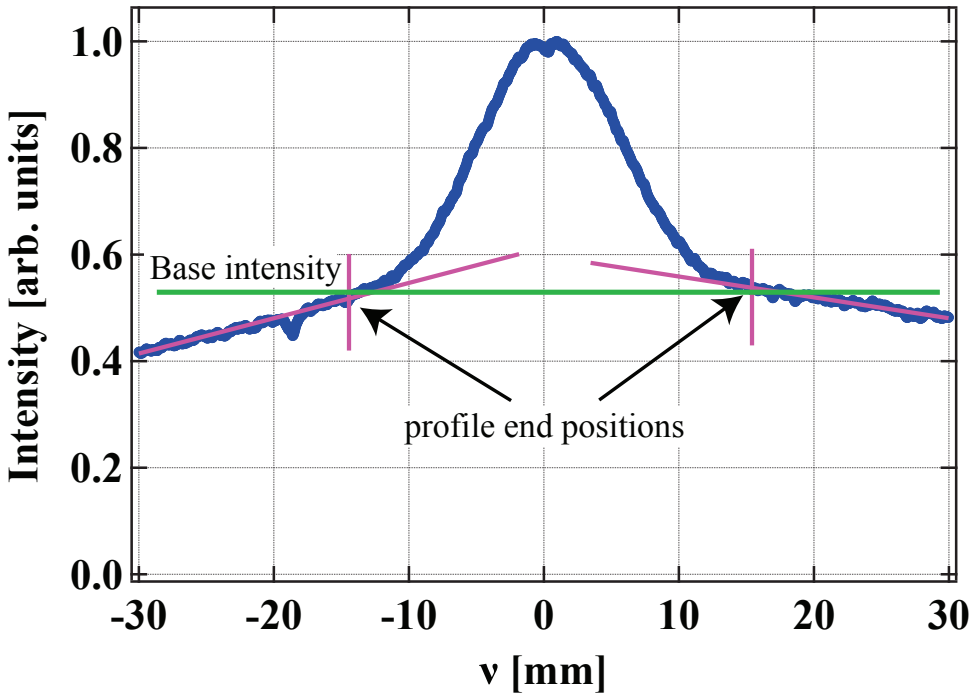

Figure 6.3: The distribution tail definition. The tail parts are fitted by linear functions and the average between the intensities of the profile end positions is defined as the base intensity.

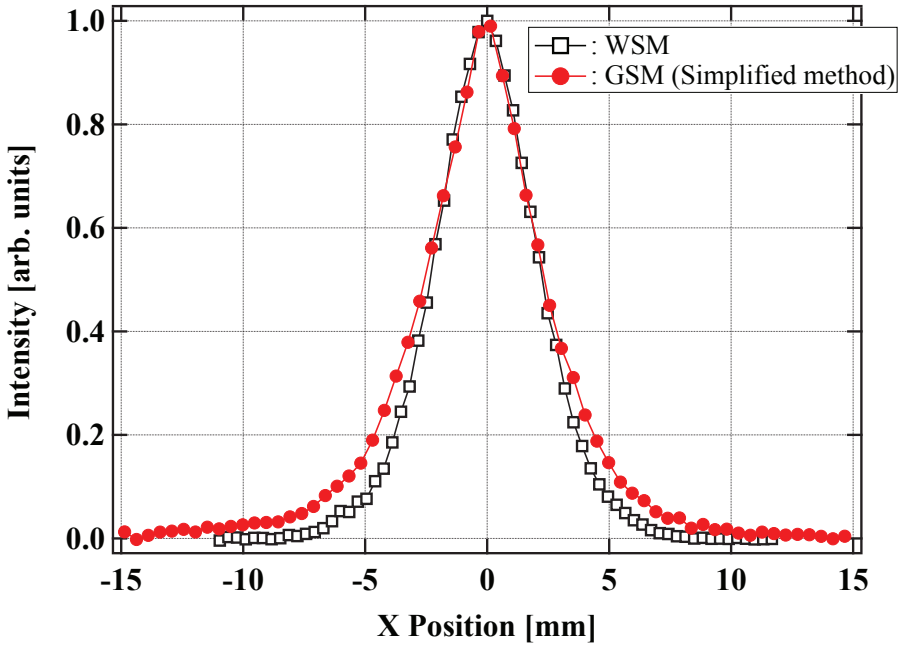

(a)

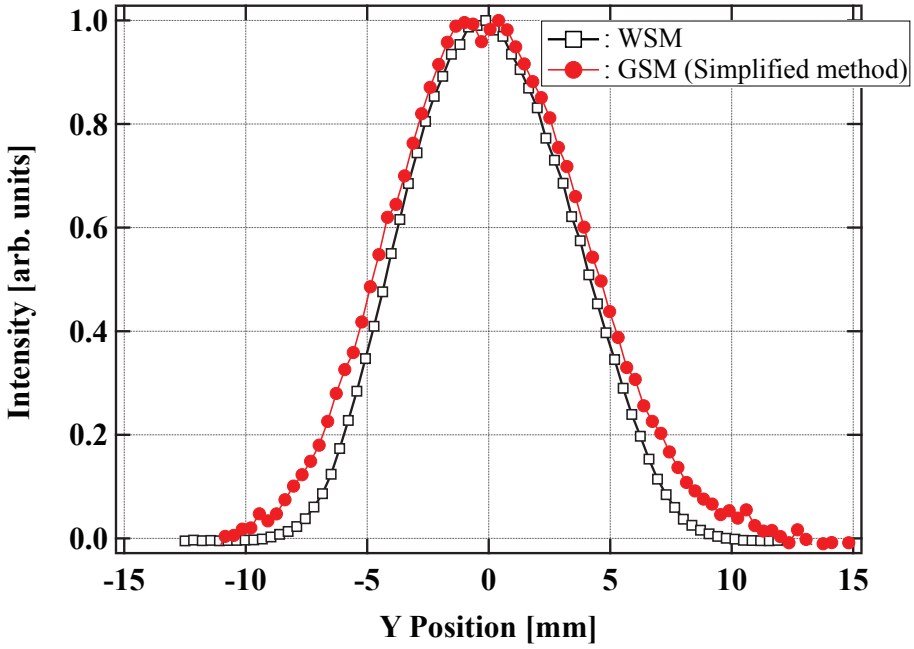

(b)

Figure 6.4: The reconstructed beam profile with the simplified method as compared with the profiles measured by the wire-scanner monitor: (a) x profiles and (b) y profiles.

6.2 Exact method

6.2.1 Method to solve double-integral equation

The exact beam profile reconstruction method inversely solves the principle equation Eq. (2.20) with the measured 4-D response function $T_{4\mathrm{D}}(\mu, \nu; x, y)$. The triple-integral equation reduces down to the double-integral equation with the 4-D response function

$$g(\mu, \nu) = \int\int T_{4\mathrm{D}}(\mu, \nu; x, y)\ F(x, y)\ \mathrm{d}x\ \mathrm{d}y. \tag{4.2}$$

However, solving it directly with the four-variable function is not straight forward. There are two choices to deal with the high dimensional function: a linearization method and an optimization method. To linearize the integral equation, the beam profile is expanded with a basis function and parameters described as $u_{kl}(x, y)$ and p_{kl}, respectively:

$$F(x, y) = \sum_{k=1}^{N_x}\sum_{l=1}^{N_y} p_{kl}\ u_{kl}(x, y). \tag{6.13}$$

where N_x and N_y are the number of parameters against x and y spaces. By discretization of the (μ, ν) space with indices i and j, the integral equation Eq. (4.2) can be rewritten as a linear equation of a four-order tensor with the expanded beam profile:

$$g_{ij} = A_{ijkl} p_{kl} \tag{6.14}$$

$$\text{where}\ \ A_{ijkl} = \int\int T_{4\mathrm{D}}(\mu_i, \nu_j; x, y)\ u_{kl}(x, y)\ \mathrm{d}x\ \mathrm{d}y. \tag{6.15}$$

If the parameter matrix p_{kl} is symmetric and the response tensor A_{ijkl} is also symmetric as $A_{ijkl} = A_{jikl}$ and $A_{ijkl} = A_{ijlk}$, the linear equation of the four-order tensor can be reduced to a linear equation of a two-order tensor. However, in case of an accelerator beam profile reconstruction, it is impossible to choose the coordinate system and a basis function to satisfy the symmetry because the beam profile is asymmetric between x and y directions due to the quadrupole focusing magnets for beam transport. As another technique to solve the equation of tensor, the singular value decomposition (SVD) is useful to find a least squares solution, particularly for an equation of matrix. For higher order tensor more than three, the SVD method requires an iteration process to find a least squares solution: the method of higher order orthogonal iteration of tensors (HOOI) [45, 46]. Therefore, solving the integral equation for the gas sheet monitor needs an optimization process for iteration even if the typical linearization method is

chosen. There are a lot of proposed optimization methods, such as gradient methods, Nelder-Mead method [47], and the method of HOOI. The Nelder-Mead method is employed because the method is easy to be implemented and does not require a numerical calculation of derivative of an objective function in the analysis process. The method using a gradient such as the Newton method tends to be unstable due to the measurement noise. The method of HOOI is not easy to be implemented like the Nelder-Mead method but may be considered as an effective approach because the method is based on SVD, which is reliable to deal with matrix computation.

In the Nelder-Mead method, an N-dimensional parameter vector is optimized geometrically by minimizing a simplex constructed from vertices of an objective function for $N+1$ parameter vectors. The parameter vector giving the maximum value of the objective function in the $N+1$ vectors is modified by moving the vector to *the reflection, the expansion or the contraction point* which is geometrically determined by the remaining N vectors as shown in Fig. 6.5. The parameter vectors are described as $\boldsymbol{p}_i$ for $i = 1, 2, ..., N+1$ and the objective function is described as $s(\boldsymbol{p}_i)$. The parameter vectors are numbered with i in increasing order of the objective function $s_i = s(\boldsymbol{p}_i)$. The average vector $\boldsymbol{p}_{\text{ave}}$ are calculated with the vectors except the $(N+1)$th vector which gives the biggest objective function:

$$\boldsymbol{p}_{\text{ave}} = \frac{1}{N}\sum_{i=1}^{N} \boldsymbol{p}_i. \tag{6.16}$$

The reflection vector $\boldsymbol{p}_{\text{ref}}$ is defined with the average vector,

$$\boldsymbol{p}_{\text{ref}} = \boldsymbol{p}_{\text{ave}} + \alpha(\boldsymbol{p}_{\text{ave}} - \boldsymbol{p}_{N+1}). \tag{6.17}$$

where α is a constant determining the search area of the optimization and is typically set to 1:

$$\boldsymbol{p}_{\text{ref}} = 2\boldsymbol{p}_{\text{ave}} - \boldsymbol{p}_{N+1}. \tag{6.18}$$

(i) If the reflection vector satisfies $s_1 \leq s(\boldsymbol{p}_{\text{ref}}) \leq s_N$, the vector $\boldsymbol{p}_{N+1}$ is replaced with $\boldsymbol{p}_{\text{ref}}$.

(ii) If the reflection vector gives the smallest objective function $s(\boldsymbol{p}_{\text{ref}}) < s_1$, the expan-

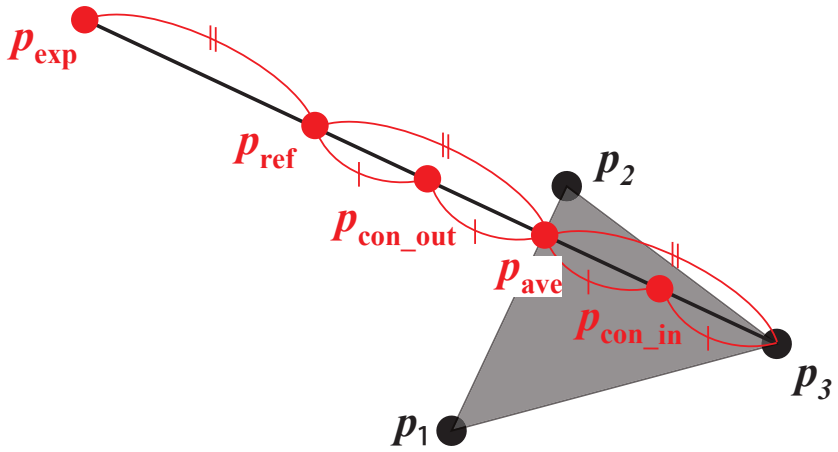

Figure 6.5: A schematic diagram of the relation among the each vector $\boldsymbol{p}_i$, the average vector $\boldsymbol{p}_{\rm ave}$, the reflection vector $\boldsymbol{p}_{\rm ref}$, the expansion vector $\boldsymbol{p}_{\rm exp}$, and the contraction vector $\boldsymbol{p}_{\rm con\_out}, \boldsymbol{p}_{\rm con\_in}$ when the parameter vector is two dimensional.

sion vector is calculated as

$$\boldsymbol{p}_{\rm exp} = \boldsymbol{p}_{\rm ave} + \beta(\boldsymbol{p}_{\rm ref} - \boldsymbol{p}_{\rm ave}) \tag{6.19}$$

where β is a constant determining the search area of the optimization and is typically set to 2:

$$\boldsymbol{p}_{\rm exp} = 2\boldsymbol{p}_{\rm ref} - \boldsymbol{p}_{N+1}. \tag{6.20}$$

If the expansion vector $\boldsymbol{p}_{\rm exp}$ gives the smaller objective function than the reflection vector $\boldsymbol{p}_{\rm ref}$, the vector $\boldsymbol{p}_{N+1}$ is replaced with $\boldsymbol{p}_{\rm exp}$. Otherwise, the vector $\boldsymbol{p}_{N+1}$ is replaced with $\boldsymbol{p}_{\rm ref}$.

(iii) If the reflection vector satisfies $s_N \leq s(\boldsymbol{p}_{\rm ref}) < s_{N+1}$, the contraction vector is defined as

$$\boldsymbol{p}_{\rm con\_out} = \boldsymbol{p}_{\rm ave} + \gamma(\boldsymbol{p}_{\rm ref} - \boldsymbol{p}_{\rm ave}) \tag{6.21}$$

or if the reflection vector gives the biggest objective function $s_{N+1} \leq s(\boldsymbol{p}_{\rm ref})$, the contraction vector is defined as

$$\boldsymbol{p}_{\rm con\_in} = \boldsymbol{p}_{\rm ave} + \gamma(\boldsymbol{p}_{N+1} - \boldsymbol{p}_{\rm ave}) \tag{6.22}$$

where γ is a constant determining the search area of the optimization and is typically

set to 0.5:

$$\boldsymbol{p}_{\text{con\_in}} = \frac{1}{2}\boldsymbol{p}_{\text{ave}} + \frac{1}{2}\boldsymbol{p}_{\text{ref}} \tag{6.23}$$

$$\boldsymbol{p}_{\text{con\_out}} = \frac{1}{2}\boldsymbol{p}_{\text{ave}} + \frac{1}{2}\boldsymbol{p}_{N+1}. \tag{6.24}$$

The contraction vectors satisfy $s(\boldsymbol{p}_{\text{con\_out}}) < s_{\text{ref}}$ or $s(\boldsymbol{p}_{\text{con\_in}}) < s_{N+1}$, the vector $\boldsymbol{p}_{N+1}$ is replaced with $\boldsymbol{p}_{\text{con\_out}}$ or $\boldsymbol{p}_{\text{con\_in}}$. If the condition is not satisfied, all of the vectors except the vector $\boldsymbol{p}_1$ is contracted to the vector $\boldsymbol{p}_1$ by

$$\boldsymbol{p}_i = \boldsymbol{p}_1 + \delta(\boldsymbol{p}_i - \boldsymbol{p}_1) \tag{6.25}$$

where δ is a constant determining the search area of the optimization and is typically set to 0.5:

$$\boldsymbol{p}_i = \frac{1}{2}\boldsymbol{p}_1 + \frac{1}{2}\boldsymbol{p}_i. \tag{6.26}$$

After changing the vector, the all vectors are sorted in the increasing order of the objective function. As shown in Fig. 6.6, this vector-replace process and the sort of the vectors are repeated until the simplex constructed from $N+1$ points of the objective function becomes enough smaller.

6.2.2 Calculation conditions

Although the Nelder-Mead method does not require any conditions for an objective function or parameters, the beam profile is expanded with a basis function for a stable analysis of the beam profile reconstruction. One typical choice of a basis function is the two-dimensional Fourier series expansion. The 2-D Fourier series expansion is suitable to express a convex function which asymptotically converges to 0 at the boundary like the beam profile,

$$F(x,y) = \sum_{k=-N}^{N}\sum_{l=-N}^{N}\left\{a_{kl}\cos\left(k\frac{\pi x}{L} + l\frac{\pi y}{L}\right) + b_{kl}\sin\left(k\frac{\pi x}{L} + l\frac{\pi y}{L}\right)\right\} \tag{6.27}$$

where L is the beam-pipe radius. However, the 2-D Fourier series expansion requires a huge number of parameters which is $2(2N+1)^2$ against N order expansion. For example, five or more orders are required to reproduce a Gaussian function and the number of parameters is over 242. Therefore, separation of variables are assumed for

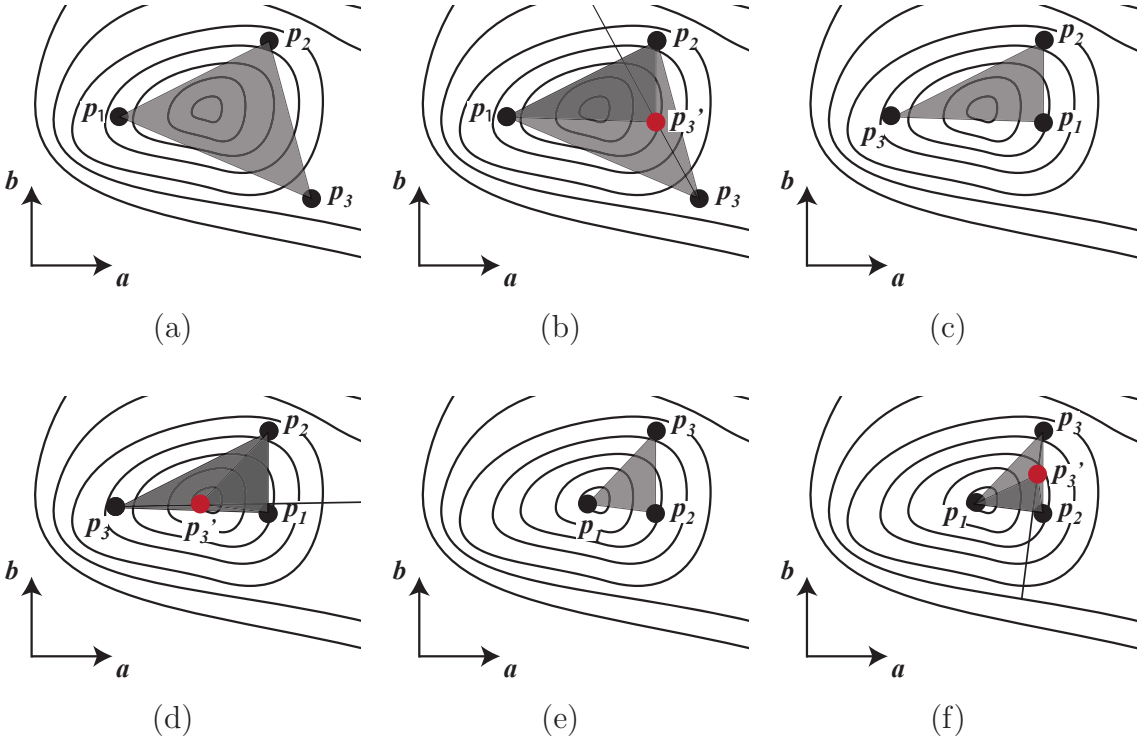

Figure 6.6: An optimization process with the Nelder-Mead method in two dimensions $\boldsymbol{p} = (a, b)$: (a) an initial condition, (b) the first step changing the worst vector with the contraction vector $\boldsymbol{p}_{\text{con\_in}}$, (c) the second step sorting the vectors, (d) the third step changing the worst vector with the contraction vector $\boldsymbol{p}_{\text{con\_in}}$, (e) the fourth step sorting the vectors, and (f) the fifth step changing the worst vector with the contraction vector $\boldsymbol{p}_{\text{con\_in}}$.

reducing the number of parameters to a realistic value,

$$\boldsymbol{a} = \{a_k\}_{k=0}^{N},\ \boldsymbol{b} = \{b_k\}_{k=1}^{N},\ \boldsymbol{c} = \{c_k\}_{k=0}^{N},\ \boldsymbol{d} = \{d_k\}_{k=1}^{N} \tag{6.28}$$

$$\boldsymbol{p} = \begin{pmatrix} \boldsymbol{a} \\ \boldsymbol{b} \\ \boldsymbol{c} \\ \boldsymbol{d} \end{pmatrix} \tag{6.29}$$

$$\begin{aligned} F(x, y; \boldsymbol{p}) = &\left[\frac{a_0}{2} + \sum_{k=1}^{N}\left\{a_k \cos\left(k\frac{\pi x}{L}\right) + b_k \sin\left(k\frac{\pi x}{L}\right)\right\}\right] \\ &\times \left[\frac{c_0}{2} + \sum_{k=1}^{N}\left\{c_k \cos\left(k\frac{\pi y}{L}\right) + d_k \sin\left(k\frac{\pi y}{L}\right)\right\}\right]. \end{aligned} \tag{6.30}$$

In this expression, the number of parameters reduces down to $4N+2$ for N order expansion. The number of parameters should be chosen by considering the calculation load and how much details of the beam profile needs to be reconstructed. In this dissertation, $N = 5$ is chosen based on a guide that Gaussian distributions in the range of the deviation σ = 1-4 mm including the typical J-PARC rms beam size of 2-3 mm can be reproduced within 1% error. The 23 beam profiles as the initial conditions of $(4N+2+1)$ vectors are defined with Fourier series of Gaussian distributions whose deviation σ are 1-4 mm.

An image obtained by high-intensity (H^-) beam measurement is defined as $g_{H^-}(\mu, \nu)$, and the integral of the assumed beam profile multiplied by the measured response function is defined as $g_{\rm int}(\mu, \nu; \boldsymbol{p})$:

$$g_{\rm int}(\mu, \nu; \boldsymbol{p}) \equiv \int\int T_{\rm 4D}(\mu, \nu; x, y)\ F(x, y; \boldsymbol{p})\ {\rm d}x\ {\rm d}y. \tag{6.31}$$

By discretization of (μ, ν) space with indices i and j, an objective function for optimization is defined as the residual for fitting $g_{\rm int}(\mu_i, \nu_j; \boldsymbol{p})$ to $g_{H^-}(\mu_i, \nu_j)$,

$$s(\boldsymbol{p}) = \sqrt{\frac{\sum_{i=1}^{M_\mu}\sum_{j=1}^{M_\nu}\left\{g_{H^-}(\mu_i, \nu_j) - g_{\rm int}(\mu_i, \nu_j; \boldsymbol{p})\right\}^2}{\sum_{i=1}^{M_\mu}\sum_{j=1}^{M_\nu}\left\{g_{H^-}(\mu_i, \nu_j)\right\}^2}}. \tag{6.32}$$

where M_μ and M_ν are the number of the image pixels. The CCD camera captures an image of $(\mu)1080 \times (\nu)1920$ pixels. The number of pixels were reduced to $(\mu)61 \times (\nu)48$ pixels by 10-pixel averaging for both axes and trimming for μ axis or thinning out every 4 pixels for ν axis to decrease the calculation load. The iteration of the parameter

optimization is terminated when the normalized simplex volume become smaller than some limit:

$$\frac{s_{\max} - s_{\min}}{\frac{1}{4N+3}\sum_{i=1}^{4N+3} s(\boldsymbol{p}_i)} < T_h, \tag{6.33}$$

where $s_{\max}, s_{\min}$ are the maximum and minimum values of the objective function in the $4N+3$ sets of parameter vectors.

6.2.3 Simulation of beam profile reconstruction

The validity of the exact profile-reconstruction method including the response-function-measurement method is simulated with assumptions of analytic functions because the beam widths or the beam profile of the pencil-like thin beam for the response-function measurement affects the beam profile reconstruction as described in Chapter 4. The response function is defined as follows to reflect the realistic gas sheet distribution which is the dominant contribution,

$$\begin{aligned} T(\mu,\nu;x,y,z) &= \delta(\mu-x)\,\delta(\nu-z)\,\left\{(1-T_0)\exp\left(-\frac{\{z-y/\tan\theta\}^2}{2{\sigma_g}^2}\right)+T_0\right\} \\ \Rightarrow T_{4\mathrm{D}}(\mu,\nu;x,y) &= \delta(\mu-x)\,\left\{(1-T_0)\exp\left(-\frac{\{\nu-y/\tan\theta\}^2}{2{\sigma_g}^2}\right)+T_0\right\}. \end{aligned} \tag{6.34}$$

The deviation σ_{gz} and the constant T_0 are assumed as 3.23 mm and 0.4 which are the estimated values based on the response-function measurement result Fig. 4.5. The high-intensity-beam profile is defined as Gaussian:

$$F(x,y) = \exp\left(-\frac{x^2}{2{\sigma_{bx}}^2}-\frac{y^2}{2{\sigma_{by}}^2}\right). \tag{6.35}$$

The deviations of the beam profile σ_{bx}, σ_{by} are set to 2.2 mm and 3.2 mm which are the J-PARC beam profile at the gas sheet monitor point estimated by the envelope equation in Chapter 5.1. The distribution $g_{\mathrm{H}^-}(\mu,\nu)$ is defined by analytical integration of Eq. (4.2) with these functions. As the pencil beam for the response-function measurement, a

rectangular function and a Gaussian function with a parameter w are considered:

$$F_{\mathrm{pen}}(x-x_0, y-y_0) = \begin{cases} 1 & |x-x_0| \leq w \text{ and } |y-y_0| \leq w \\ 0 & \text{others} \end{cases} \tag{6.36}$$

$$F_{\mathrm{pen}}(x-x_0, y-y_0) = \exp\left(-\frac{(x-x_0)^2+(y-y_0)^2}{2w^2}\right). \tag{6.37}$$

As the realistic beam profile, the fitting function to the measured electron beam profile described in Chapter 4.2 is also considered with the assumption that the separation of variables in the (x, y) space is possible. A measured response function $\widetilde{T}_{4\mathrm{D}}(\mu, \nu; x, y)$ is analytically constructed by applying the pencil beam to Eq. (4.1),

$$\widetilde{T}_{4\mathrm{D}}(\mu, \nu; x_0, y_0) = \int\int T_{4\mathrm{D}}(\mu, \nu; x, y)\, F_{\mathrm{pen}}(x-x_0, y-y_0)\, \mathrm{d}x\, \mathrm{d}y. \tag{6.38}$$

The scan step of the pencil beam position which determines the spatial resolution of the profile reconstruction is defined by considering the calculation load and the size of the high-intensity beam to be analyzed. This parameter is adjusted to the response-function-measurement condition which is the scan step of 0.5 mm for x direction and 1.0 mm for y direction. The number of scan points are set to 21 in both x and y directions. The basis function for beam-profile reconstruction is defined as a Gaussian to compare it with the real beam profile $F(x, y)$ [Eq. (6.35)]:

$$\widetilde{F}(x, y) = A \exp\left(-\frac{x^2}{2\widetilde{\sigma}_x{}^2} - \frac{y^2}{2\widetilde{\sigma}_y{}^2}\right). \tag{6.39}$$

where $A, \widetilde{\sigma}_x, \widetilde{\sigma}_y$ are the free parameters for optimization. The beam profile $\widetilde{F}(x, y)$ is reconstructed with the Nelder-Mead method by applying the constructed response function $\widetilde{T}_{4\mathrm{D}}(\mu, \nu; x_0, y_0)$ and the function $g_{\mathrm{H}^-}(\mu, \nu)$ into Eq. (4.2). The difference between the reconstructed beam profile and the real beam profile are evaluated with an error in the beam profile deviation:

$$\text{error} = \frac{\sigma_{bx} - \widetilde{\sigma}_x}{\sigma_{bx}} \text{ or } \frac{\sigma_{by} - \widetilde{\sigma}_y}{\sigma_{by}}. \tag{6.40}$$

Figure 6.7 shows the error in the reconstructed profile to the real profile against the pencil beam parameter w. The errors are zero when the pencil beam width w is smaller than 0.5 mm in x direction and 1.0 mm in y direction against the rectangular function and smaller than 0.1 mm in x direction and 0.2 mm in y direction against

the Gaussian function. The errors increase against the increment of the parameter w; the reconstructed beam profiles become thiner. In the realistic case of the pencil beam profile described by Eq. (4.4), the error in the reconstructed profiles are 28.1% for the x direction and 12.4% for the y direction as shown with the broken lines. These results are caused by two reasons: the effects of the spatial resolution and the gas-density spatial distribution. The high-intensity beam profile is defined on the (x, y) space with the meshes of the spatial resolution $\Delta x \times \Delta y$ which are determined by the scan step of the pencil beam position for the response-function measurement. This data treatment means that the reconstruction method regards the pencil beam as a rectangular beam having the width $\Delta x, \Delta y$ because the profile reconstruction is based on determining the intensities of each mesh as shown in Fig. 6.8a. If the pencil beam is thicker than the spatial resolutions (the scan steps) Δx and Δy as shown in Fig. 6.8b, a response function expanding the signal distribution from the spatial resolution size to the pencil beam size is constructed. Therefore, the high-intensity beam profile thinner than the real profile is reconstructed with the response function. On the other hand, a pencil beam thinner than the resolution as shown in Fig. 6.8c constructs a response function making an integral distribution $g_{\rm int}(\mu, \nu; \boldsymbol{p})$ with gaps. However, the reconstructed profile corresponds to the real beam profile because the fine structure of the distribution $g_{\rm int}(\mu, \nu)$ less than the spatial resolution cannot be expressed. The errors of zero against use of a pencil beam thinner than the resolutions of 0.5 mm in x direction and 1.0 mm in y direction shown in Fig. 6.7 can be understood by the explanation. This effect due to the beam width thicker or thinner than the spatial resolution appears prominently in x direction because the x space directly corresponds to the μ space. In y direction, the effect does not appear because the y space is correlated with the (μ, ν) space through an integral and the out-of-focus effect which is ignored for simplicity in this estimation. If the out-of-focus effect is considered, the use-of-thicker-beam effect appears in both x and y directions. While the assumption of the homogeneous gas density distribution in x direction has no influence on the x-profile reconstruction, it affects the y-profile reconstruction. According to Eq. (6.38), the pencil beam profile can be regarded as a window function to extract the response function. Therefore, use of a beam thicker than the gas-density-distribution structure corresponds to taking a moving average of the real response function, and the measured response function is broader than with the real one. The broadened response function gives a beam profile thinner than the real beam profile as a reconstruction result. Thus, the pencil beam widths should be same or thinner than the spatial resolution determined by the target high-intensity beam

profile and the gas density spatial distribution. The spatial resolution defines the scan step of the pencil beam as the same size.

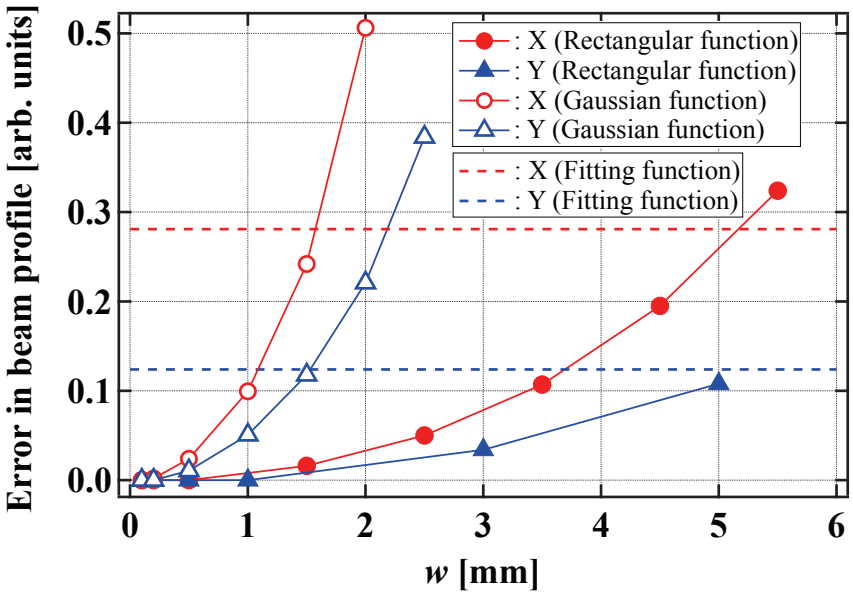

Figure 6.7: The error in the reconstructed beam profile to the real profile against the pencil beam width w.

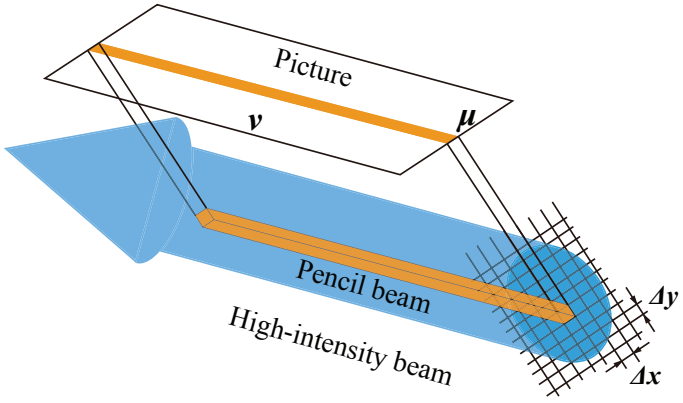

(a)

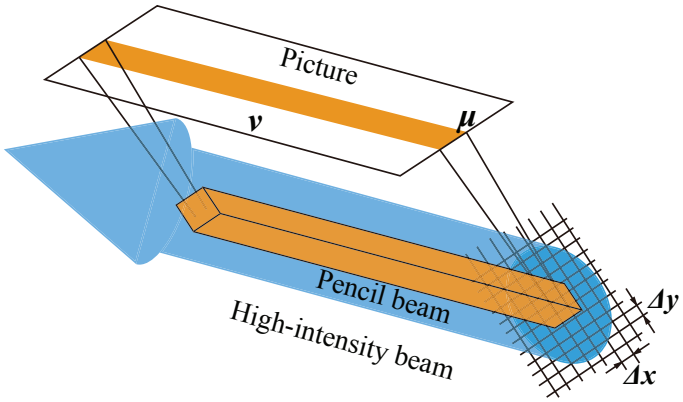

(b)

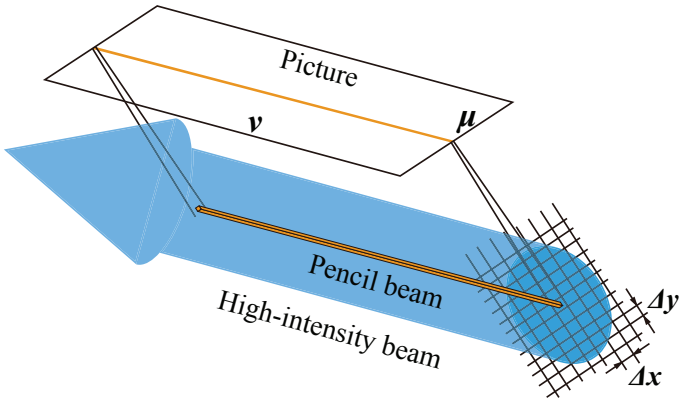

(c)

Figure 6.8: The profile reconstruction using the exact method is based on determining the intensities of each mesh where the high-intensity beam is defined. The mesh is defined not as the pencil beam width but as the scan step of the pencil beam. (a) The pencil beam width corresponding to the scan step is the ideal condition. (b) The thicker pencil beam yields the response function expanding the signal distribution. (c) The thinner pencil beam gives the response function constructing an integral distribution $g_{\mathrm{int}}(\mu, \nu)$ with gaps.

6.2.4 J-PARC H^- beam reconstruction

In this section, the beam profile reconstruction using the exact method is performed with the J-PARC H^- beam-profile-measurement result described in Chapter 5.2.1 and Fig. 5.5. Figure 6.9a shows the captured $g_{H^-}(\mu, \nu)$ distribution of the J-PARC H^- beam measurement result. Figures 6.9b and 6.9c show the integral distributions $g_{\rm int}(\mu, \nu)$ with one of the initial conditions and with the optimized beam profile for the condition 1, which is the no-noise-reduction condition of the 2-D Fourier transform described in Chapter 4.3. Figures 6.10 shows the integral distributions $g_{\rm int}(\mu, \nu)$ with two kinds of the initial conditions and with the optimized beam profile for the condition 2 that the noise reduction area is outside $(\xi_1.\xi_2, \zeta_1, \zeta_2) = (0.148, 1.60, 0.167, 0.418)$. Figures 6.11 shows the integral distributions $g_{\rm int}(\mu, \nu)$ with two kinds of the initial conditions and with the optimized beam profile for the condition 3 that the noise reduction area is outside $(\xi_1.\xi_2, \zeta_1, \zeta_2) = (0.148, 0.445, 0.167, 0.418)$. Figures 6.12 and 6.13 show the projected distributions $G(\mu), G(\nu)$ of Figs. 6.9, 6.10 and 6.11 against the initial conditions and the optimized profiles. In Fig. 6.12, the initial conditions 1, 2 and 3 correspond to the panels of Figs. 6.10a, 6.10b and 6.11a. The reconstructed 2-D beam profiles and the projected profiles are shown in Figs. 6.14 and 6.15. The iteration process was terminated at $T_h = 10^{-3}$. The number of iteration process are 147, 224 and 397 for the condition 1, 2 and 3 (70 iterations/hour) and the residuals between $g_{\rm int}(\mu, \nu)$ and $g_{H^-}(\mu, \nu)$ calculated by Eq. (6.32) are 16%, 15% and 11% for the conditions 1, 2 and 3, respectively. The transitions of the normalized simplex volume against the number of the iteration are shown in Fig. 6.16. The error in the reconstructed beam profile against the real profile is affected by the residual and the error due to the response-function measurement estimated in Section 6.2.3. While the conditions 1 and 2 reconstruct the almost same profiles, the condition 3 yields a widely different profile from the other conditions. This result implies that the condition 2 properly reduces the noise and the condition 3 may have lost the important part in the wave number spaces. Therefore, the amount of the noise reduction should be chosen considering the change of the reconstructed profile against the noise reduction condition. The reconstructed x profiles for the all conditions are thinner than the one obtained by the wire-scanner monitor as expected with the simulation describe in Section 4.2.3. On the other hand, the reconstructed y profiles are almost same as the one obtained by the wire-scanner monitor. This result is caused by the limitation that the measurement region of the response function does not cover the entire region where the J-PARC H^- beam passes through due to the structure of the present system. The reconstructed profile is considered to be thicker than the

one estimated with the simulation because the integral region of the reconstruction analysis is smaller than the real integral region. According to the simulation described in Section 4.2.3 against the limited response function, the errors in the beam profile are estimated to become 27.7% from 28.1% for x profile and 7.0% from 12.4% for y profile. Therefore, in the real case, the contraction effect due to the thick pencil beam and the expansion effect due to restriction of the integral region are considered to almost cancel out in the y profile. Considering the reconstruction residual of 11-16%, the y profile is successfully reconstructed within the possible error range.

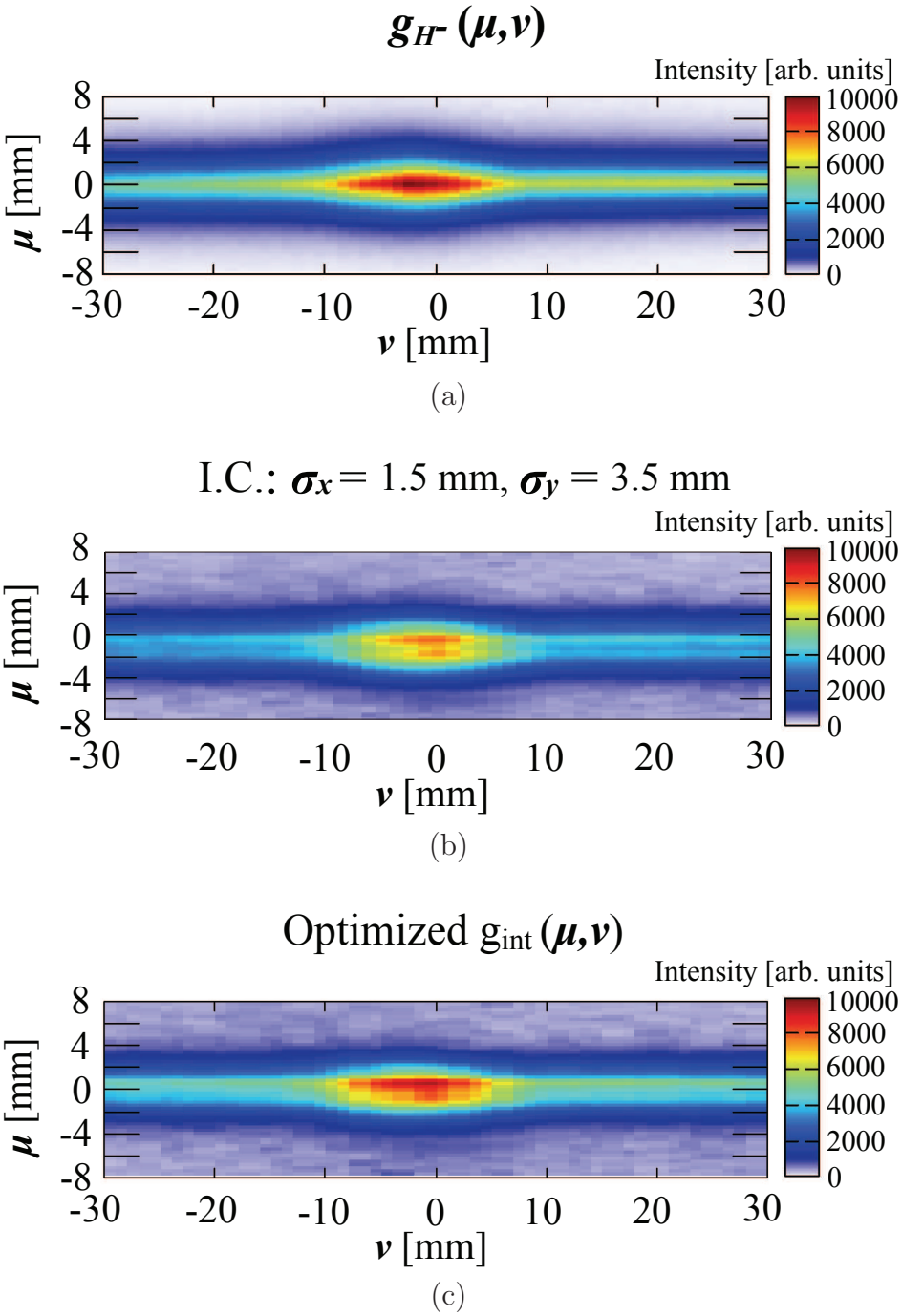

Figure 6.9: The $g(\mu, \nu)$ distributions of (a) the J-PARC H^- beam measurement result and the integrated distributions with (b) one initial condition and (c) the optimized beam profile for the noise-cut Fourier-transform condition 1.

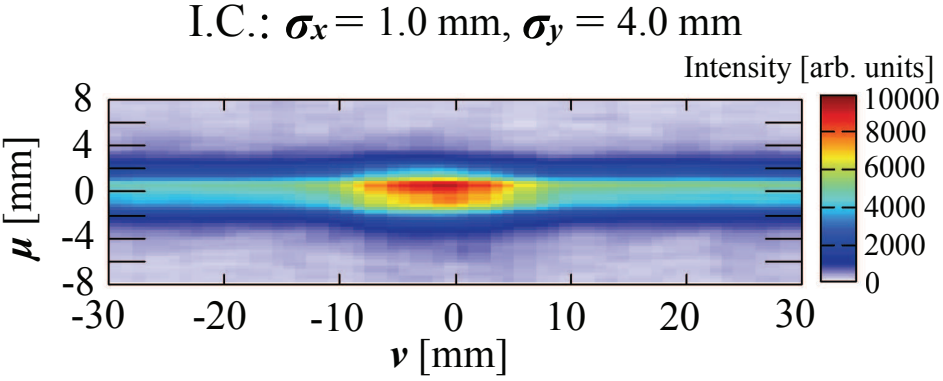

(a)

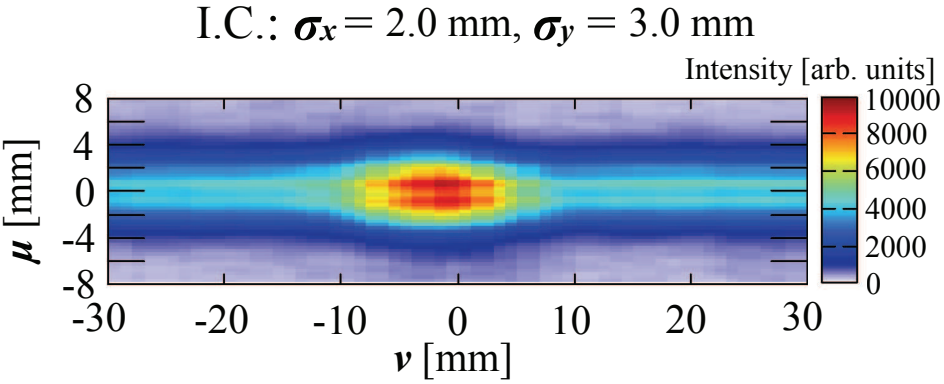

(b)

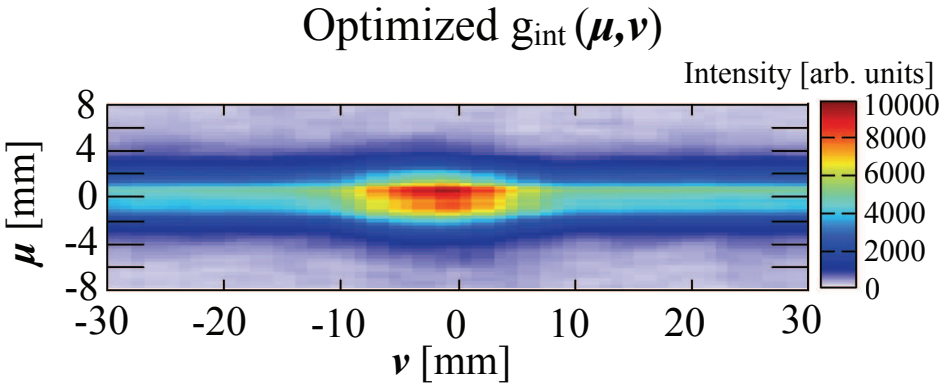

(c)

Figure 6.10: The integrated distributions $g(\mu, \nu)$ with (a)(b) two initial conditions and (c) the optimized beam profile for the noise-cut Fourier-transform condition 2.

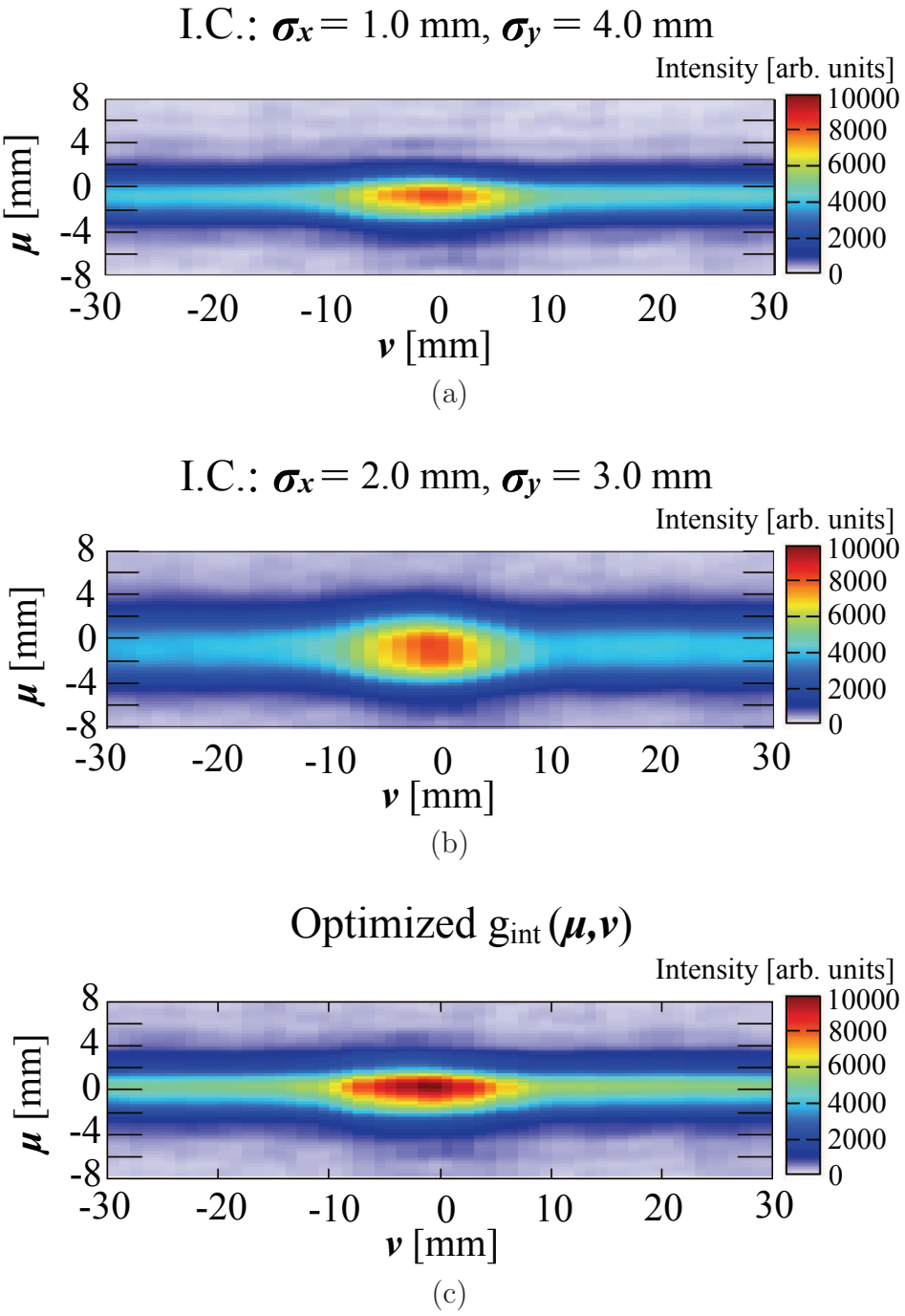

Figure 6.11: The integrated distributions $g(\mu, \nu)$ with (a)(b) two initial conditions and (c) the optimized beam profile for the noise-cut Fourier-transform condition 3.

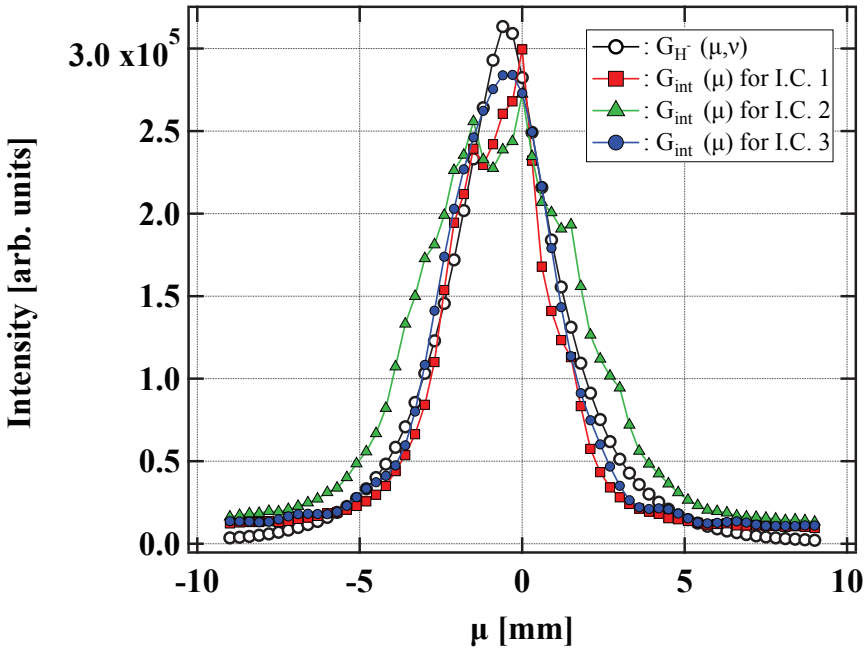

(a)

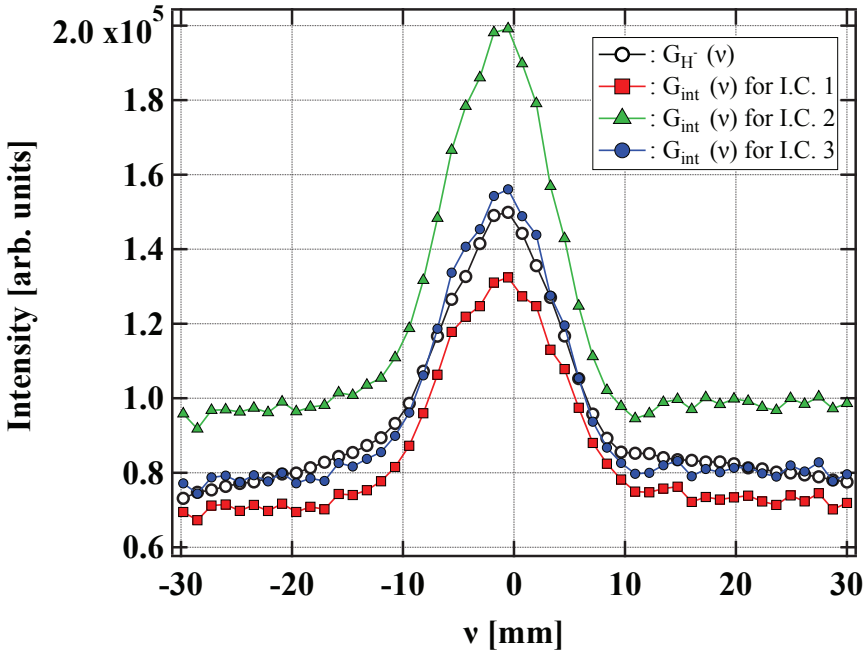

(b)

Figure 6.12: Comparison of the projected distributions (a) $G(\mu)$ and (b) $G(\nu)$ of the J-PARC beam measurement result and the initial conditions. The I.C. 1, 2 and 3 correspond to Fig. 6.10a, Fig. 6.10b and Fig. 6.11a.

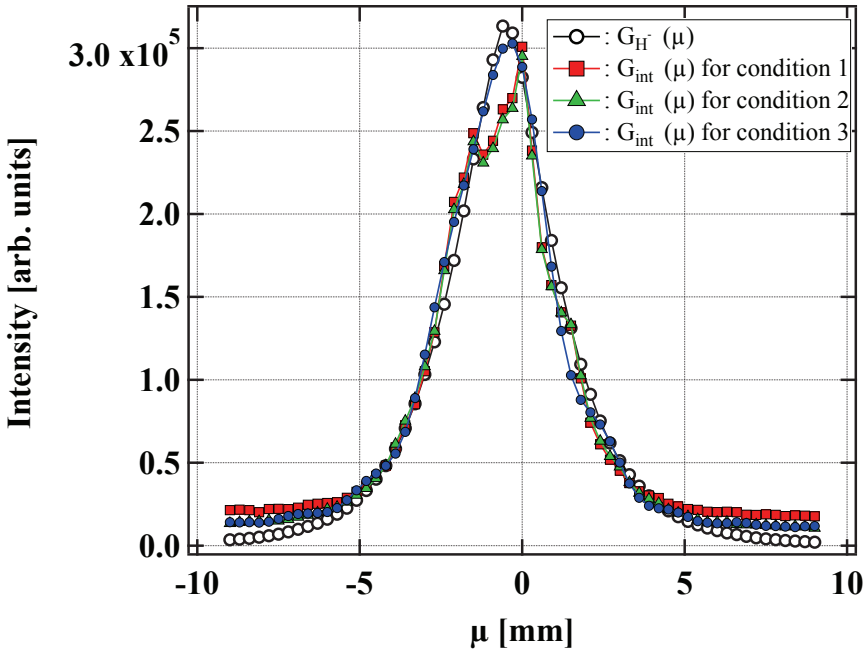

(a)

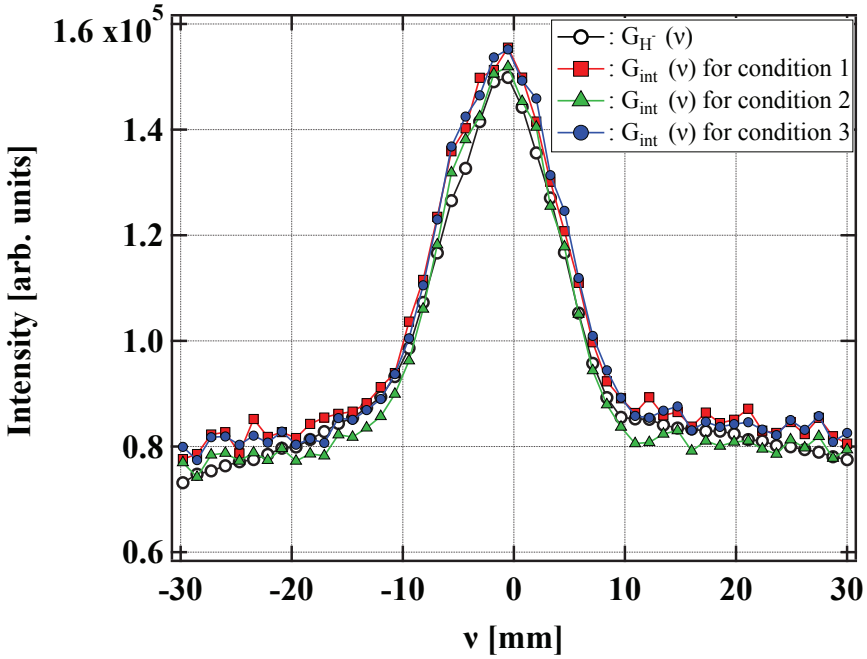

(b)

Figure 6.13: Comparison of the projected distributions (a) $G(\mu)$ and (b) $G(\nu)$ of the J-PARC beam measurement result and the optimized distributions for each noise-reduction condition.

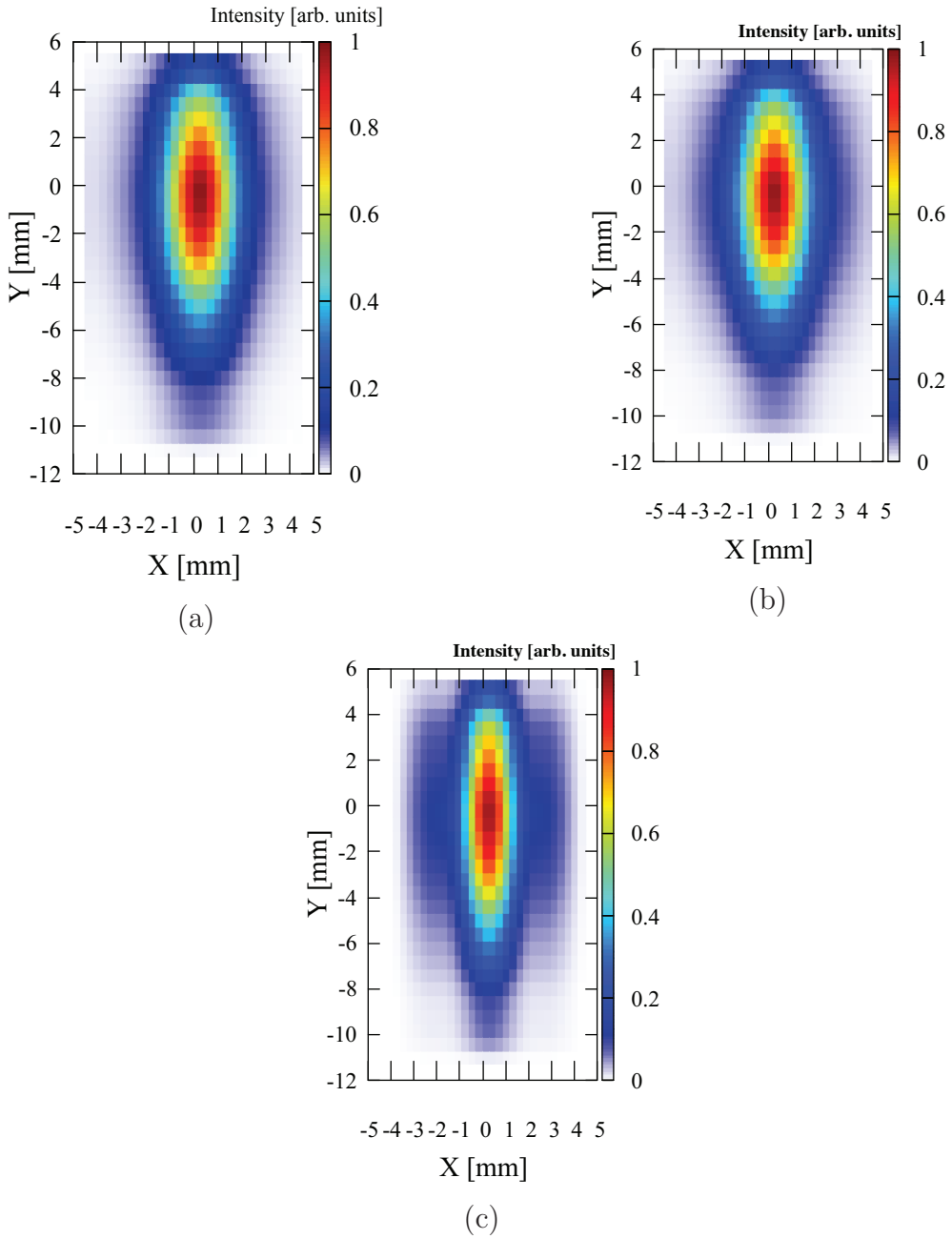

Figure 6.14: The reconstructed 2-D beam profiles: (a) the noise-reduction condition 1, (b) the noise-reduction condition 2 and (c) the noise-reduction condition 3.

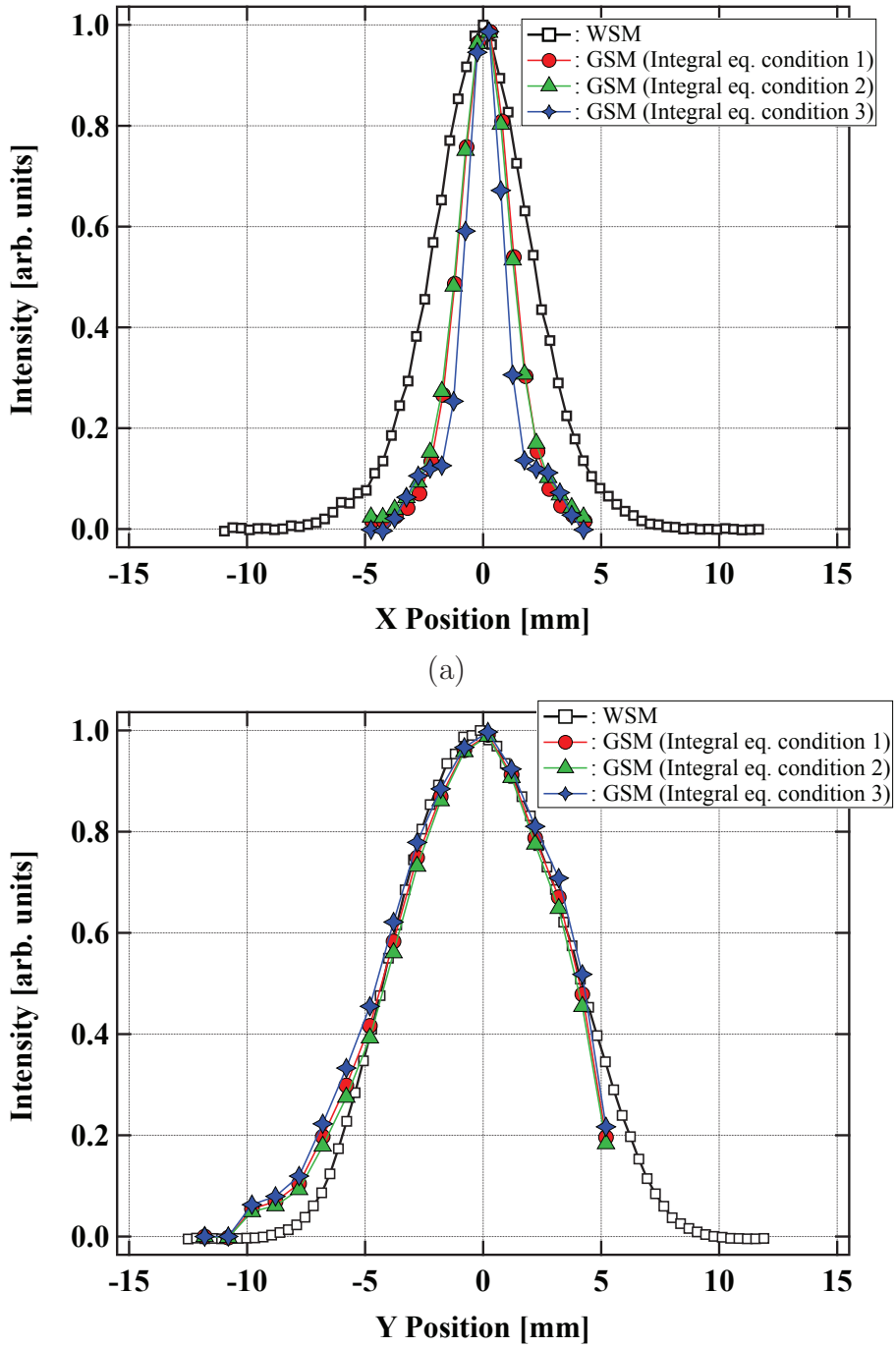

(a)

(b)

Figure 6.15: The projected profiles of Fig. 6.14: (a) x profiles and (b) y profiles. The open black rectangular plots describe the profiles obtained by the wire-scanner monitor.

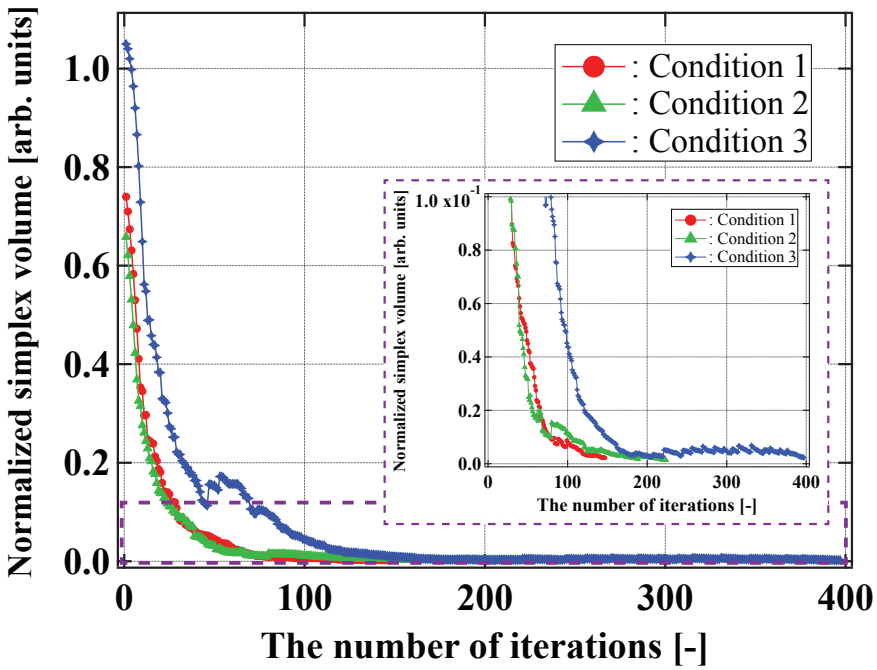

Figure 6.16: The transitions of the normalized simplex volume against the number of the iteration.

6.2.5 Improvement of exact method

To verify the x profile broadens because of the response function measured with the thick electron beam, the exact reconstruction method is improved with an approximation. The electron-beam-width effect contributes to the response function as the one of the point-spread effects. The all point-spread effects are approximated as delta functions to eliminate the electron-beam-width effect, and the response function $T(\mu, \nu; x, y, z)$ can be simplified as

$$\begin{aligned} T(\mu,\nu;x,y,z) = \sigma\, n(x,y,z)\, \alpha_{CCD}(\mu,\nu) \int\int T_3(\mu,\nu;\, {}^2x,{}^2z)\, \alpha_{I.I.}({}^2x,{}^2z) \\ T_2({}^2x,{}^2z;\, {}^1x,{}^1y,{}^1z)\, T_1({}^1x,{}^1y,{}^1z;\, x,y,z)\, \mathrm{d}^3({}^1x)\, \mathrm{d}^2({}^2x). \end{aligned} \tag{2.19}$$

$$T(\mu,\nu;x,y,z) = \sigma\, n(x,y,z)\, \alpha_{\mathrm{sa}}(y)\, \alpha_{CCD}(\mu,\nu)\, \alpha_{I.I.}(\mu,\nu)\, \delta(\mu - x)\, \delta(\nu - z) \tag{6.41}$$

where $\alpha_{\mathrm{sa}}(y)$ composing $T_2({}^2x,{}^2z;\, {}^1x,{}^1y,{}^1z)$ as the function with respect to ${}^1y$ describes the non-uniformity of the solid angle for collecting the photons. The integral equation Eq. (2.20) describing the profile measurement principle

$$g(\mu,\nu) = \int T(\mu,\nu;x,y,z)\, F(x,y;z)\, \mathrm{d}^3x \tag{2.20}$$

can be simplified as

$$g(\mu,\nu) = \int k(\mu,\nu;y)\, F(\mu,y;\nu)\mathrm{d}y \tag{6.42}$$

$$\text{where} \quad k(\mu,\nu;y) = \sigma\, \alpha_{CCD}(\mu,\nu)\, \alpha_{I.I.}(\mu,\nu)\, n(\mu,y,\nu)\, \alpha_{\mathrm{sa}}(y). \tag{6.43}$$

The function $k(\mu, \nu; y)$ is defined as the simplified response function. According to this single-integral equation, the z dependance of the beam can be measured as the ν dependance because the signal spread along the z direction is ignored. However, to reduce the number of the parameters, the z dependance of the high-intensity beam profile is assumed as uniform: $F(\mu, y; \nu) \to F(\mu, y)$. The variable μ is regarded as an index or a parameter, and Eq. (6.42) becomes

$$g(\nu;\mu) = \int k(y,\nu;\mu)\, F(y;\mu)\mathrm{d}y. \tag{6.44}$$

The 2-D beam profile can be reconstructed by arraying the y profile for each x position because the μ space directly corresponds to the x space without the integration ($x = \mu$); the electron-beam-width effect in the x direction does not appeared.

The simplified response function $k(y, \nu; \mu)$ is constructed with the response function measurement results. In this approximated profile reconstruction method, the spatial resolution of the beam profile reconstruction in the x direction can be determined arbitrarily because the integral of the principle equation with respect to x axis is absent. As for the y direction, the spatial resolution is the same as the exact method. Therefore, the simplified response function is defined with the measured 4-D response function $\widetilde{T}_{4\mathrm{D}}(\mu, \nu; x, y)$ as

$$k(y, \nu; \mu_0) = \int_{\mu_0 - \Delta x/2}^{\mu_0 + \Delta x/2} \widetilde{T}_{4\mathrm{D}}(\mu, \nu; \mu_0, y)\, \mathrm{d}\mu \tag{6.45}$$

where Δx is the spatial resolution of the profile reconstruction in the x direction and $x = \mu_0$ is the center position of the electron beam. The reconstruction resolution in the x direction is defined as 1.0 mm, and the y direction is defined as 1.0 mm as same as the reconstruction condition described in Chapter 6.2.

The single-integral equation Eq. (6.44) was solved with the Nelder-Mead method, and the basis function of the y profile is defined as the Fourier series expansion:

$$F(y; \boldsymbol{a}(\mu), \boldsymbol{b}(\mu)) = \frac{a_0(\mu)}{2} + \sum_{k=1}^{10} \left\{ a_k(\mu) \cos\left(k \frac{\pi y}{L}\right) + b_k(\mu) \sin\left(k \frac{\pi y}{L}\right) \right\} \tag{6.46}$$

where $\boldsymbol{a}, \boldsymbol{b}$ are the optimization parameters. The optimization process was terminated with $T_h = 10^{-3}$.

Figure 6.17 shows the reconstructed 2-D beam profile, and Figure 6.18 shows the projected profiles as compared with the ones measured with the wire-scanner monitor. The residual of the profile reconstruction was 7% on average for all y profiles. The 2-D profile is interpolated to be smooth. The x profile is improved as compared with the one reconstructed by the exact method described in Chapter 6.2. Thus, the error in the reconstructed beam profile shown in Fig. 6.15 thinner than the wire-scanner monitor is caused by the electron beam width thicker than the reconstruction spatial resolution. Although the reconstructed profile includes the error due to ignoring the all point-spread effects, this approximation method can improve the beam profile reconstructed with the exact method in case that the thick electron beam is utilized to measure the response function.

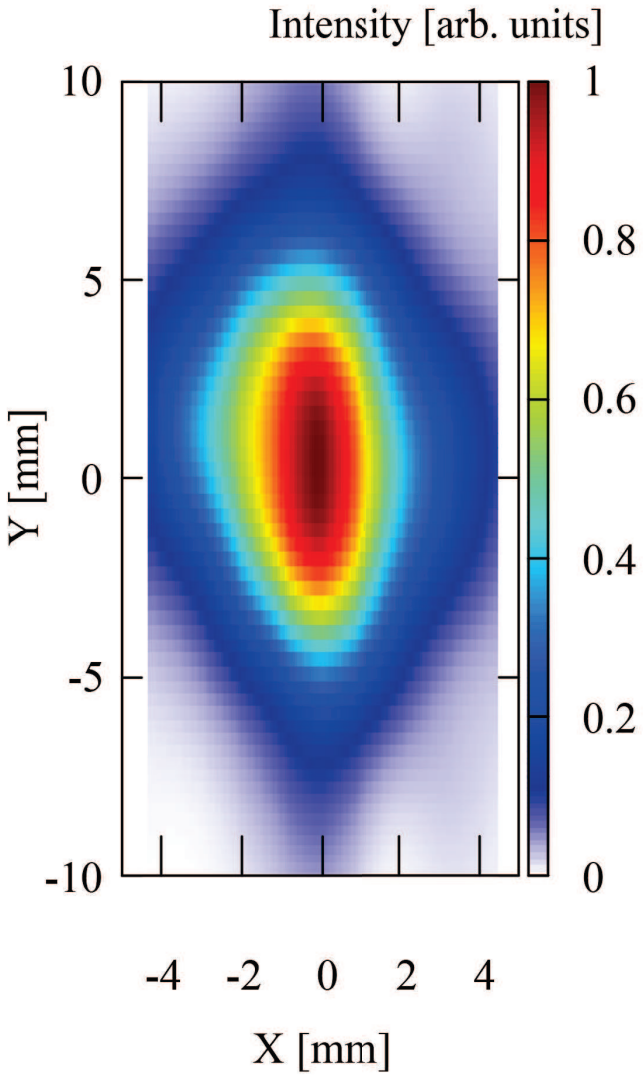

Figure 6.17: The reconstructed 2-D beam profile with the approximated method.

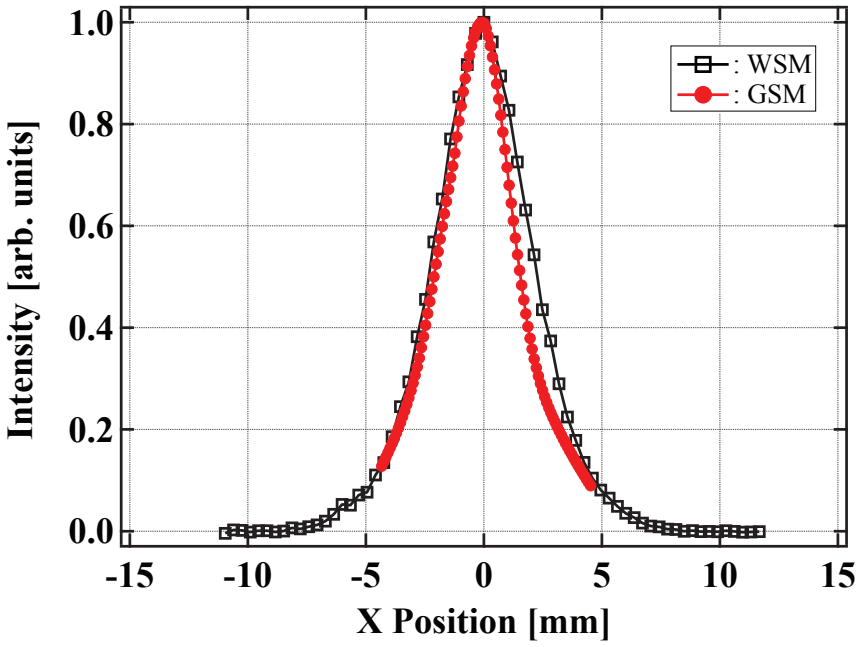

(a)

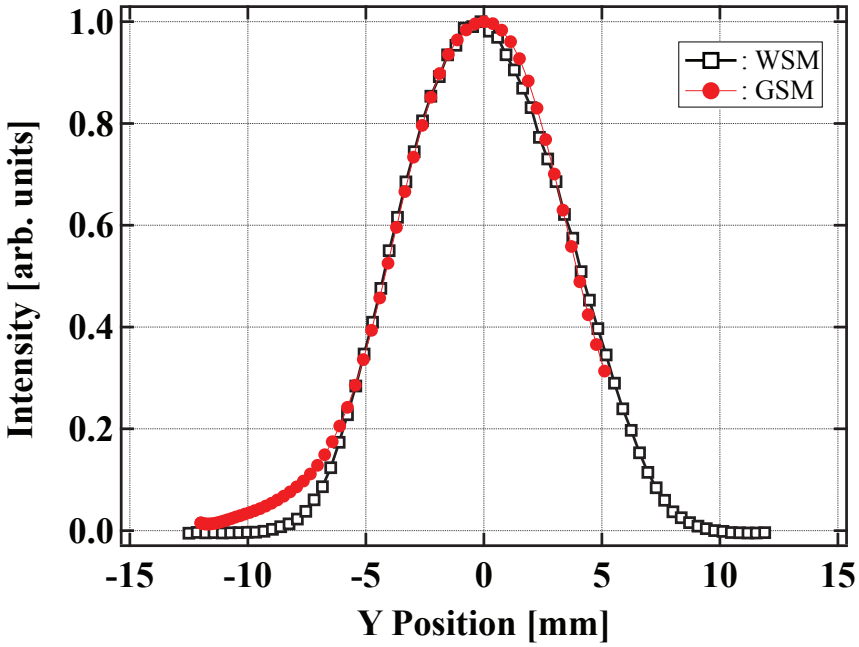

(b)

Figure 6.18: The projected beam profiles in (a) the x direction and (b) the y direction as compared with the ones measured with the wire-scanner monitor.

While the above improvement approximates the exact method, there are two choices to reduce the error in the beam profile reconstructed by the exact method without the approximation: improving the electron beam source and reconstructing the true response function. Since the error is caused by use of the thick electron beam, the thinner electron beam can reduce the error in both x and y profiles. As the other way, the true response function $T_{4D}(\mu, \nu; x, y)$ can be reconstructed with the equation of the response-function-measurement principle Eq (6.38) from the measured response function $\widetilde{T}_{4D}(\mu, \nu; x, y)$:

$$\widetilde{T}_{4D}(\mu, \nu; x_0, y_0) = \int\int T_{4D}(\mu, \nu; x, y)\, F_{pen}(x - x_0, y - y_0)\, \mathrm{d}x\, \mathrm{d}y. \tag{6.38}$$

Because this integral equation can be regarded as a convolution for the variables (x_0, y_0, x, y) with the parameters (μ, ν), the 2-D Fourier transform simplifies the integral equation as follows:

$$\widehat{\widetilde{T}}_{4D}(\xi, \zeta; \mu, \nu) = \widehat{T}_{4D}(\xi, \zeta; \mu, \nu)\, \widehat{F}_{pen}(\xi, \zeta) \tag{6.47}$$

$$\widehat{T}_{4D}(\xi, \zeta; \mu, \nu) = \frac{\widehat{\widetilde{T}}_{4D}(\xi, \zeta; \mu, \nu)}{\widehat{F}_{pen}(\xi, \zeta)}. \tag{6.48}$$

Thus, if the 2-D electron beam profile is given, the correct response function with the measurement accuracy of the electron-beam profile can be obtained independently of the electron beam profile, and the exact reconstruction method becomes easier to be utilized. In addition, this improve method has a possibility to reconstruct the 5-D response function if the z dependance of the electron beam profile is also given:

$$\widetilde{T}_{4D}(\mu, \nu; x_0, y_0) = \int T(\mu, \nu; x, y, z)\, F_{pen}(x - x_0, y - y_0; z)\, \mathrm{d}^3x. \tag{6.38}$$

6.3 Conclusion

In this Chapter, the high-intensity beam profile reconstruction was demonstrated with the two methods based on the integral equation describing the profile measurement principle of the gas sheet monitor. Although the simplified method causes the error in the profile shape due to ignoring the response function, the beam profile is easily and immediately reconstructed because of the direct analysis from the captured image data. The method is useful for a beam operation or a beam commissioning due to the possibility of a real-time analysis. The exact method solves the integral equation with the measured response function. While the method takes a long time of iteration calculation, such as several hours, to reconstruct a beam profile, the reconstructed profile may correspond to the real profile within the range of the measurement errors of both the high-intensity beam profile measurement and the response function measurement. The method is useful for a high-intensity-beam dynamics study due to the accuracy. In the present case, the systematic error on the response function measurement due to the electron beam playing a role of the measurement probe caused the big error. The approximation ignoring the point-spread effects improved the accuracy of the profile reconstruction, and it was verified that the exact method can reconstruct the beam profile. To improve the accuracy of the beam profile reconstruction based on the exact method without the approximation, the electron beam source satisfying the requirement clarified in Section 6.2.3 should be utilized or a more accurate response function should be reconstructed with the electron beam profile.

One important thing is that the simplified method can be utilized only when the response function except the gas density distribution is approximately uniform. Figure 6.19 shows Fig. 6.4 with the reconstructed profiles using the simplified method from the image captured with the damaged image intensifier. The amplification-efficiency spatial distribution of the image intensifier changed due to strong room light in the J-PARC beam measurement experiment. Although this method is supposed to reconstruct a profile thicker than the real profile, the non-uniform amplification efficiency distribution makes the reconstructed beam profile thinner. On the other hand, the exact method can reconstruct the beam profile independent of the measurement system conditions if the response function is measured. Thus, the two kinds of the reconstruction method should be chosen considering the measurement purpose and the conditions of the measurement system arrangement.

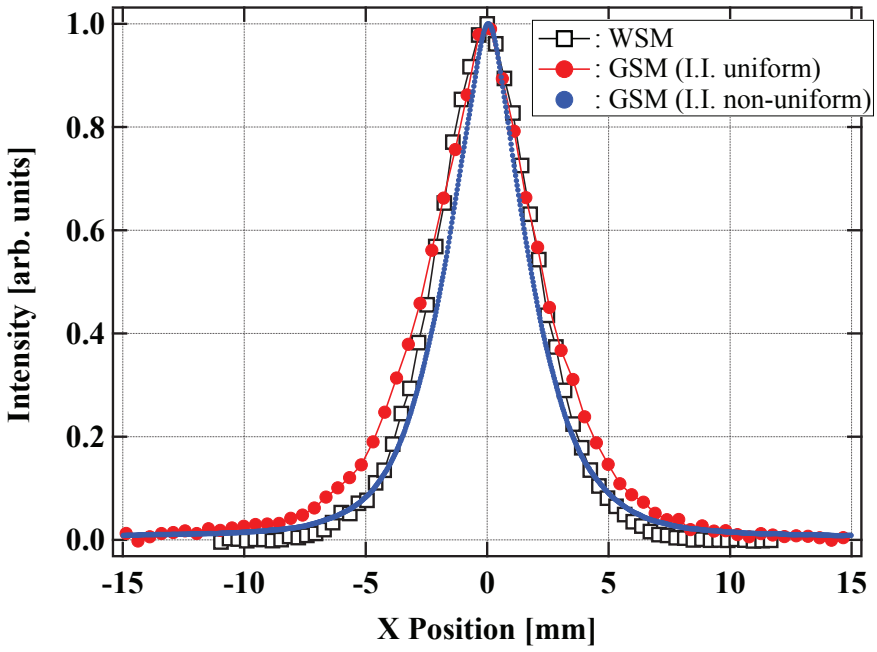

(a)

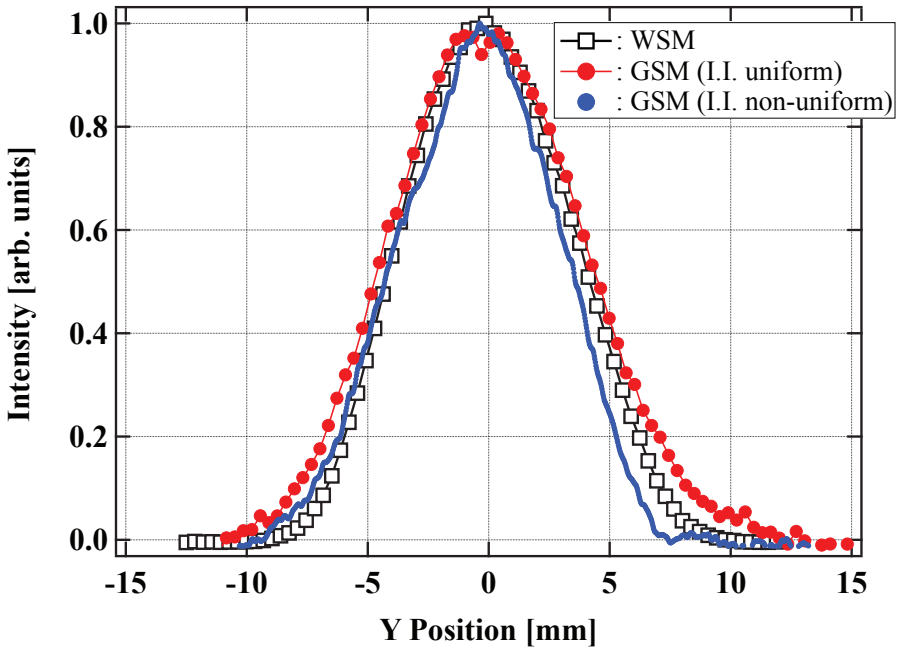

(b)

Figure 6.19: The reconstructed profiles using the simplified method from the image captured with the damaged image intensifier: the blue plots. The other plots are the same as Fig. 6.4.

References

[45] B. N. Sheehan and Y. Saad, "Higher order orthogonal iteration of tensors (hooi) and its relation to pca and glram", SDM (2007) 10.1137/1.9781611972771.32.

[46] Y. Liu, F. Shang, W. Fan, J. Cheng, and H. Cheng, "Generalized higher-order orthogonal iteration for tensor decomposition and completion", **27**, edited by Z. Ghahramani, M. Welling, C. Cortes, N. Lawrence, and K. Q. Weinberger (2014).

[47] J. A. Nelder and R. Mead, "A simplex method for function minimization", Computer Journal **7**, 308313 (1965).

Chapter 7

Influence of Gas Sheet Injection on Beam

The gas sheet monitor is one of the non-destructive beam profile monitors based on beam-gas interaction. While the monitor using a residual gas is almost non-destructive, the gas-injection type monitor like the gas sheet monitor may have an influence on the beam due to interaction with the extra gas. The main processes of interaction between an H^- beam and nitrogen gas are considered as

$$H^- + N_2 \rightarrow H^- + (N_2{}^+)^*/N_2{}^+ + e^- \tag{7.1}$$

$$H^- + N_2 \rightarrow H^0 + (N_2{}^+)^*/N_2{}^+ + 2e^- \tag{7.2}$$

$$H^- + N_2{}^+ \rightarrow H^- + (N_2{}^+)^* \tag{7.3}$$

$$H^- + N_2{}^+ \rightarrow H^0 + (N_2{}^+)^*/N_2{}^+ + e^-. \tag{7.4}$$

A part of the negative hydrogen ion beam particles is stripped of its electron in the process of Eqs. (7.2), (7.4). These processes destruct the H^- beam and should be evaluated. The processes of Eqs. (7.3), (7.4) indicate that the beam interacts with the produced nitrogen ions. The electromagnetic interaction as well as the scattering due to elastic collisions may affect the phase space distribution of the beam. In this chapter, the destructiveness of the gas sheet monitor due to the gas sheet injection is evaluated from the perspectives of the beam charge stripping and the change of the phase space distribution.

7.1 Beam charge stripping

7.1.1 Measurement method of beam current

The RFQ test stand shown in Fig. 7.1 is equipped with the current transformers (CTs) and the bending magnet, and the separated H^- beam current with the bending magnet can be measured. The current reduction was quantified by comparing the signal intensity of the CT against the gas sheet flux because the gas inlet pressure or the gas injection flux is not linearly proportional to the gas pressure at each position due to the transition of the gas flow model in the sheet generator. The beam current measured with the upstream CT is define as $I_{\mathrm{CT1}}(Q_{\mathrm{sheet}})$, and the one measured with the downstream CT is defined as $I_{\mathrm{CT2}}(Q_{\mathrm{sheet}})$. Since the beam current fluctuates, the beam current reduction is defined as follows:

$$1 - \frac{I_{\mathrm{CT2}}(Q_{\mathrm{sheet}})/I_{\mathrm{CT1}}(Q_{\mathrm{sheet}})}{I_{\mathrm{CT2}}(0)/I_{\mathrm{CT1}}(0)}. \tag{7.5}$$

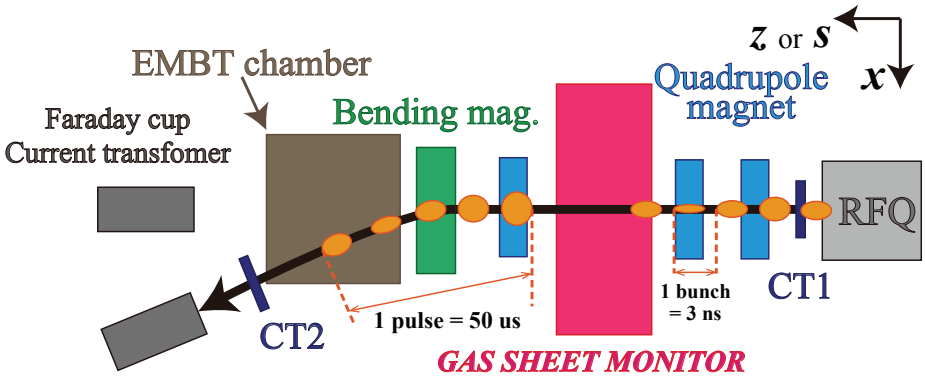

Figure 7.1: The locations of the current transformers, the bending magnet, and the gas sheet monitor.

7.1.2 Experimental result

Figure 7.2 shows the current reduction against the gas sheet flux. The charge stripping due to the gas sheet injection exists, and the amount of the current reduction is linearly proportional to the gas sheet flux.

The amount of the current reduction is estimated theoretically. The charge stripping processes are described as Eq. (7.2) and Eq. (7.4). The latter process caused by the

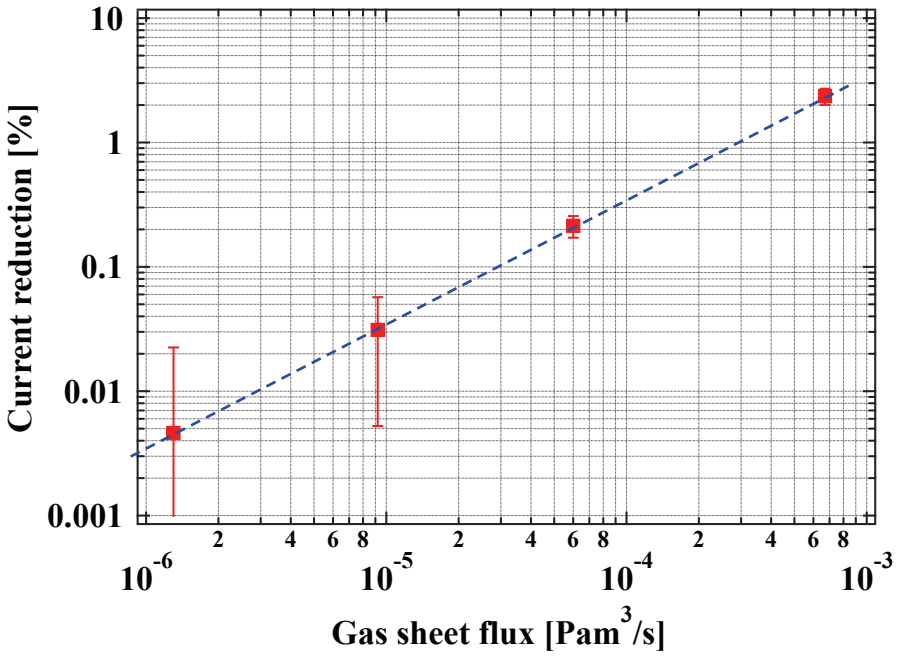

Figure 7.2: The characteristic of the current reduction against the gas sheet flux. The blue broken line is the linear fitting line of the measured plots. The error bar describes the standard deviation.

produced nitrogen ions is considered to be negligible since the ion density is enough lower than the density of the introduced nitrogen gas molecules as follows. The nitrogen ion density produced by a beam bunch, the ionization cross section, the gas density, the beam current density, the charge of the beam particles, and the acceleration frequency are described as n_{ion}, σ_{ion}, n_g, j, q, and f_{RF}, respectively. The ion density can be described as

$$n_{\mathrm{ion}} = \sigma_{\mathrm{ion}}\, n_g\, \frac{j}{q}\, \frac{1}{f_{\mathrm{RF}}}. \tag{7.6}$$

The ionization cross section is assumed as 6×10^{-21} m^2 for a 3 MeV proton beam impact on nitrogen gas [48]. The current density is defined as the peak density of a 60 mA Gaussian distribution beam of $\sigma = 2.5$ mm, and the RFQ frequency is 324 MHz. The ion density normalized by the gas density is calculated as $n_{\mathrm{ion}}/n_g = 2.2 \times 10^{-7}$. Even if the all ions produced in 50 μs of the beam pulse including about 16,000 bunches survive, the ratio becomes only 3.5×10^{-3}. Therefore, the electron stripping process due to the nitrogen ions described as Eq. (7.4) is negligible. To calculate the process of Eq. (7.2), the H^0 line density production rate, the electron stripping cross section, and the beam current are described as λ_{H^0}, σ_{es}, and I, respectively. The line density rate

of the H^0 production can be written as

$$\lambda_{H^0} = \sigma_{es}\, n_g\, I/q, \tag{7.7}$$

$$\Rightarrow R_{es} = \frac{\lambda_{H^0}\, l}{I/q} = \sigma_{es}\, n_g\, l \tag{7.8}$$

where l is the beam flight length along the beam axis in the gas density of n_g and R_{es} is the current reduction ratio due to the electron stripping. The factor $n_g\, l$ requires the gas density spatial distribution along the beam axis. Figure 7.3 shows the schematic diagram of the gas density distribution estimated from the gas pressure gauges and the density calibration result described in Chapter 4.4 against the gas-sheet-generator inlet pressure of 1 kPa corresponding to the gas sheet flux of 6.7×10^{-4} Pa m^3/s. In the beam pipe connecting the RFQ to the gas sheet monitor and the pipe connecting the gas sheet monitor to the MEBT chamber, the gas pressure is assumed to decrease linearly. The electron stripping cross section for 3 MeV H^- beam impact on nitrogen gas is deduced as 2×10^{20} m^2 from the ones for 30 keV, 35 keV, or 1 MeV H^- beam impact on nitrogen gas by the Bethe-Bloch formula [27, 49–51]. The beam current reduction can be calculated as

$$R_{es} = \sigma_{es} \sum n_g\, l \tag{7.9}$$

$$= 0.75\% \tag{7.10}$$

This estimated value agrees with the experimental value of 2.36% with the factor of 3. From these results, the current reduction due to the gas injection can be estimated and is to be one of the index to determine the amount of the gas injection.

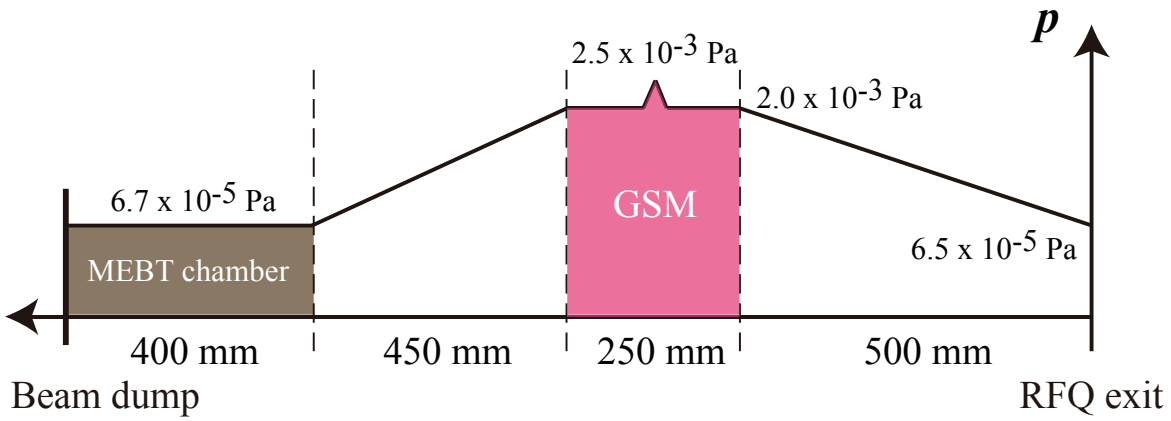

Figure 7.3: The estimation of the gas density spatial distribution along the beam axis for the gas-sheet-generator inlet pressure of 1 kPa corresponding to the gas sheet flux of 6.7×10^{-4} Pa m^3/s.

7.2 Change of phase space distribution

The 2-D phase space distribution of the beam can be measured with the double-slit-type emittance monitor placed at the MEBT chamber shown in Figs. 5.2, 7.1. The dependance of the phase space distribution against the gas sheet flux was evaluated to investigate the influence of interaction between the beam and the produced plasma and the influence of the scattering.

Figure 7.4 shows the measured 2-D phase space distributions with/without the gas sheet injection. The prime symbol means the derivative with respect to the $s = \beta_L ct$ axis where β_L is the Lorentz factor and c is the speed of light. The condition of the gas sheet injection was the gas sheet flux of 6.7×10^{-4} Pa m^3/s corresponding to the inlet pressure of 1 kPa. The green ellipses describe the 5 times of the root-mean-square (rms) emittances. Table 7.1 shows the Twiss parameters α, β and the rms emittance for the panels in Fig. 7.4 which are the fitting parameters of the ellipse. While there are some differences in the Twiss parameters, the influence of the gas sheet injection cannot be distinguished in the 2-D phase space. Figure 7.5 shows the projected distributions of Fig. 7.4. Each projected distribution is normalized by its area corresponding to the beam current because the beam current reduces due to the gas sheet injection. The influence of the gas sheet injection can be recognized, and the beam-gas interaction changes the distributions to be thin in both the spatial and velocity spaces, particularly in the y-y' space. Figure 7.6 shows the characteristics of the rms emittance against the gas sheet flux. While the emittance in the x direction does not change, the emittance in the y direction decreases at the flux more than 5.8×10^{-5} Pa m^3/s corresponding to the inlet pressure of 100 Pa. The decrease of the emittance corresponding to improvement of the beam quality can be explained by the space charge neutralization effect [52–60]. The beam bunches repeatedly create the nitrogen ions on the beam line, and the ions are integrated around the center of the beam axis by the H^- beam potential as shown in Fig. 7.7. When the potential constructed by the ions are the same as the one produced by the beam particles, the potentials cancel each other. Therefore, the space charge force inducing the emittance growth vanishes, and the emittance does not grow. In the present case, the emittance is considered not to grow in the x-x' space and to grow in the y-y' space when the gas sheet is not injected.

The strength of the space charge neutralization effect (S.C.N.) is estimated as the ratio of the produced ion density to the beam particle density with consideration of the

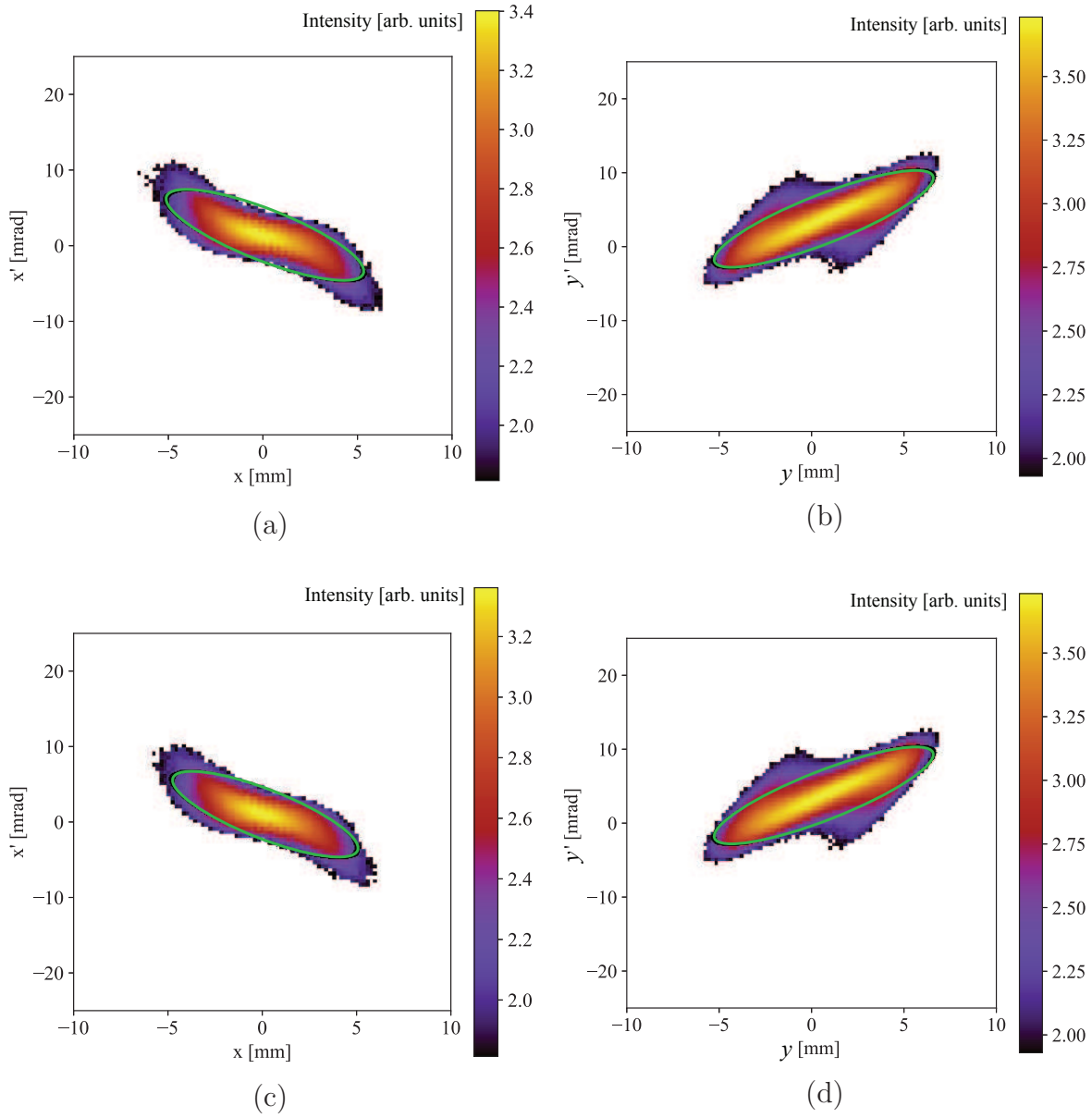

Figure 7.4: The 2-D phase space measured with the double-slit-type emittance monitors: (a)(b) x-x' space and y-y' space without gas sheet injection and (c)(d) x-x' space and y-y' space with gas sheet injection at the gas sheet flux of 6.7×10^{-4} Pa m^3/s corresponding to the inlet pressure of 1 kPa.

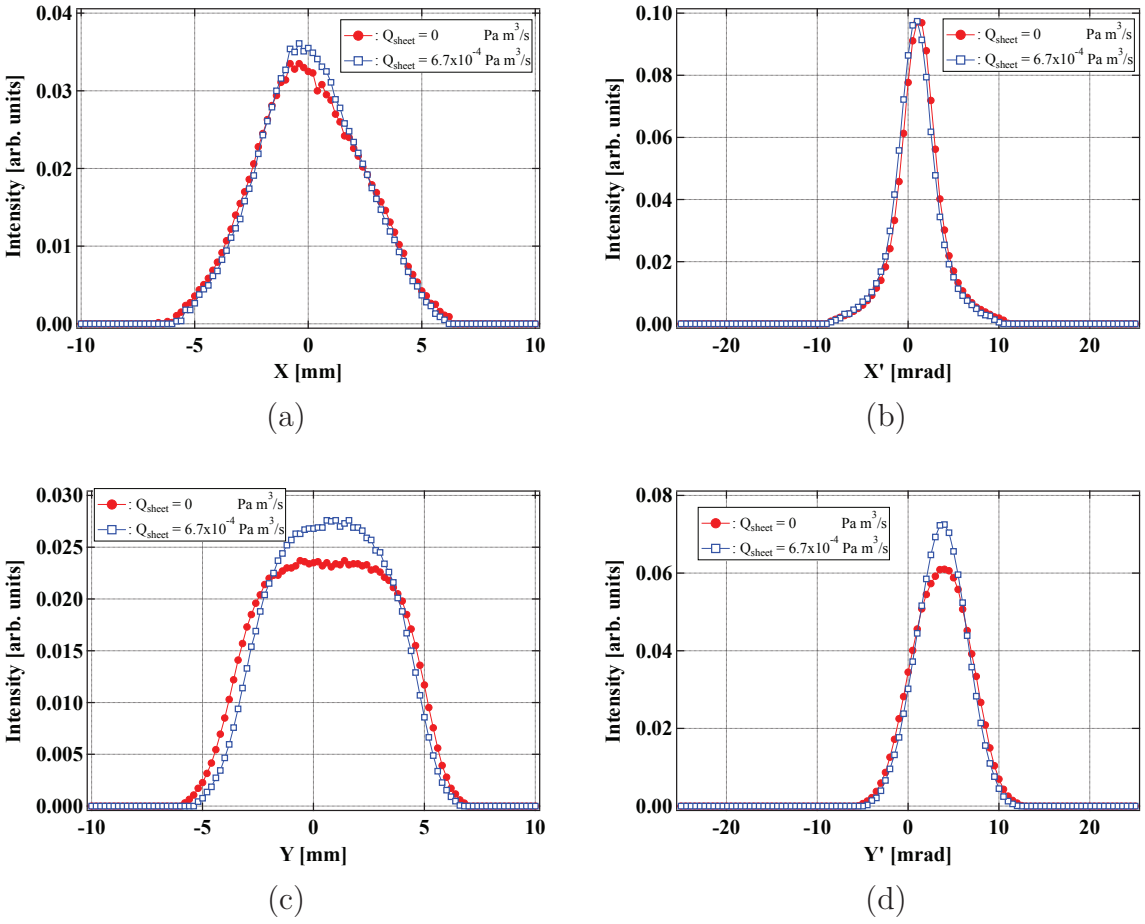

Figure 7.5: The projected distributions of Fig. 7.4 along (a) x direction, (b) x' direction, (c) y direction, and (d) y' direction.

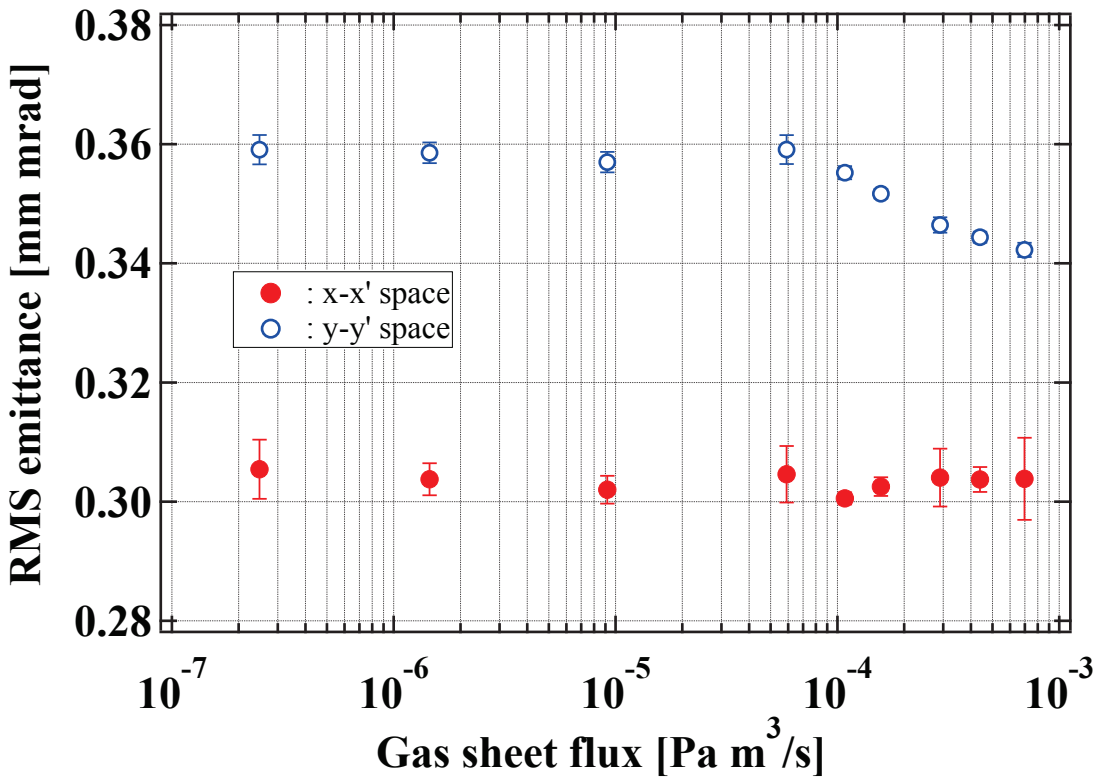

Figure 7.6: The characteristics of the rms emittance against the gas sheet flux. The error bar describes the standard deviation.

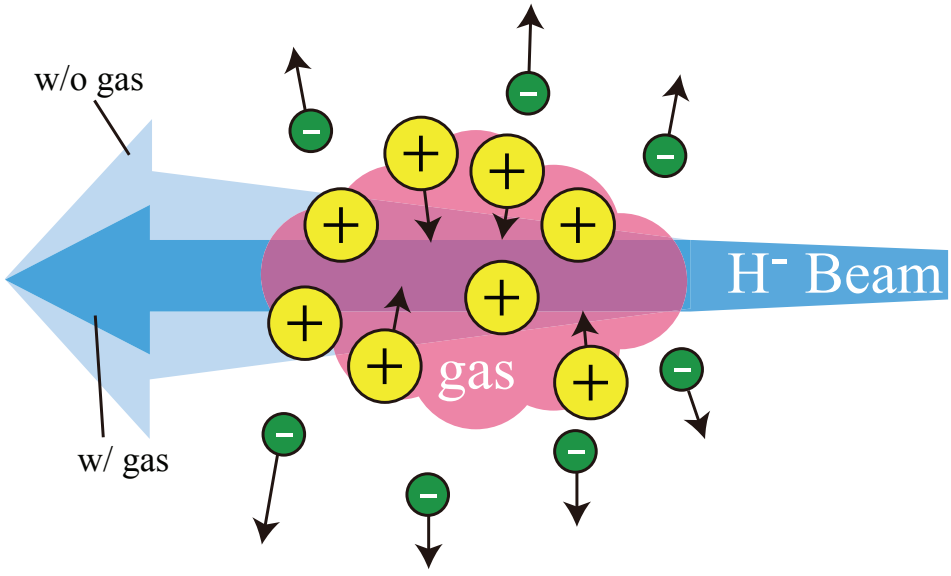

Figure 7.7: A schematic diagram of the space-charge neutralization effect.

Table 7.1: The Twiss parameters of the phase space measurement.

	x-x' space		y-y' space	
	w/o gas	w/ gas	w/o gas	w/ gas
Twiss α [-]	1.29	1.24	-1.47	-1.13
Twiss β [mm/mrad]	1.42	1.35	1.57	1.33
Emittance [mm mrad]	0.305	0.304	0.359	0.342

valence Z. From Eq. 7.6, S.C.N. can be described as

$$\text{S.C.N.} = \frac{Z_{\text{ion}} n_{\text{ion}}}{Z_{\text{beam}} n_{\text{beam}}} = \sigma_{\text{ion}}\, n_g\, \frac{Z_{\text{ion}}}{Z_{\text{beam}}} \frac{\beta_L\, c}{f_{\text{RF}}}. \tag{7.11}$$

In the present situation, $Z_{\text{ion}} = Z_{\text{beam}} = 1$ and $\beta_L = 0.08$, and S.C.N. for a single beam bunch can be written as

$$\text{S.C.N.}|_{\text{1bunch}} = 4.32 \times 10^{-22}\, n_g. \tag{7.12}$$

In the 50 μs beam pulse including about 1.6×10^4 bunches, S.C.N. becomes

$$\text{S.C.N.}|_{\text{1pulse}} = 6.91 \times 10^{-18}\, n_g. \tag{7.13}$$

When the gas pressure is 10^{-7} Pa like the base pressure of the beam line, S.C.N. is estimated as 1.7×10^{-4} and is negligible. For the gas pressure of 10^{-3} Pa which is the gas sheet peak pressure, S.C.N. is estimated as 1.67. Although the produced ions decrease against time and the density of the ions is considered not to exceed the density of the beam due to the ion's space charge force in actual, the space charge neutralization may occur with the 10^{-3} Pa gas sheet.

To verify that the emittance growth occurs in the y-y' space and does not occur in the x-x' space, the beam phase space development along the beam traveling direction were simulated with the IMPACT code which is one of the particle-in-cell simulation codes [61–63]. The initial condition of the simulation is given as the 2-D phase space distribution measured with the emittance monitor without the gas sheet injection. Figure 7.8 shows the simulated beam envelope trajectories and the emittance developments. The beam envelope trajectories simulated with the envelope simulation described in Chapter 5 agrees well with the ones simulated with the IMPACT code. While the emittance in the x direction does not grow, the emittance in the y direction grows around $s = 0.5$ m where the gas sheet monitor is placed. The reason of the result

is that the emittance growth occurs where the beam size is big. Since the beam size in the x direction is small as compared with the y direction, the difference between the x and y directions appears. The emittance at the RFQ exit is estimated as 0.34 mm mrad in the PIC simulation, and the measured emittance with the gas sheet of the maximum flux agrees well with it; the gas sheet injection mitigates the emittance growth in the y-y' space. Thus, the measurement result of the emittance against the gas sheet flux can be explained with the space charge neutralization effect. This result implies that the beam profile measurement with the gas sheet monitor does not always have an adverse influence on the beam. Since the space charge neutralization occurs when the profile is measured with the produced photons without any electrodes, a new advantage of the photon-detection-based profile measurement was found.

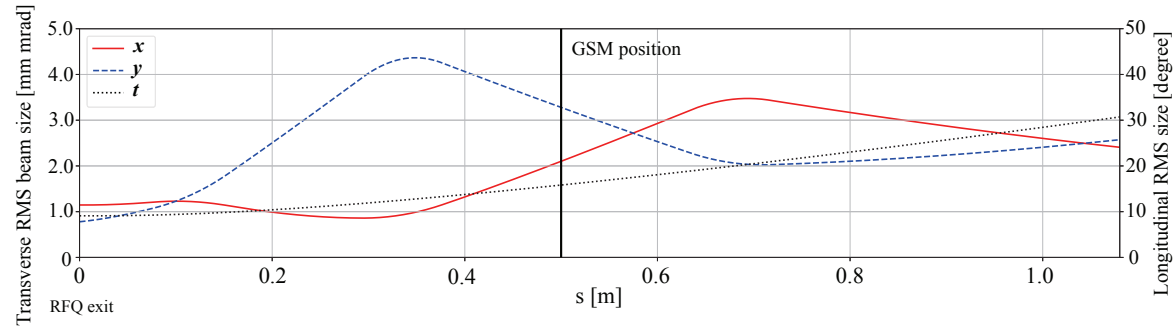

(a)

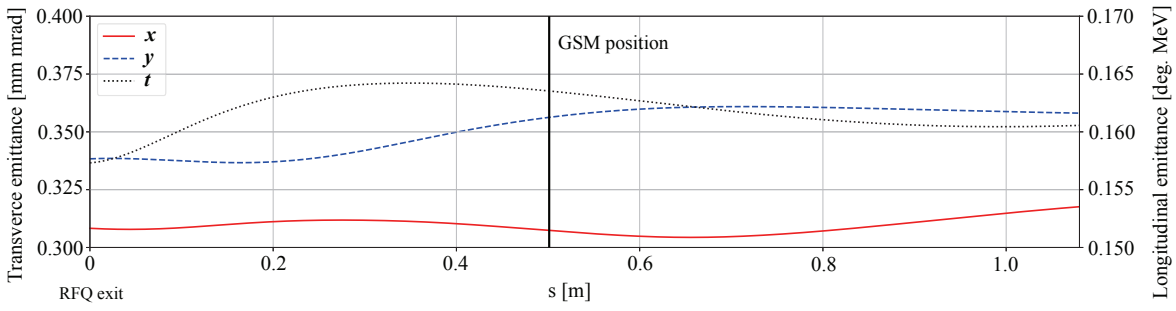

(b)

Figure 7.8: (a) The simulated beam envelope trajectories and (b) the simulated emittance developments along s axis with the IMPACT code. The position $s = 0$ is the RFQ exit and $s = 0.5$ is the gas sheet monitor's position.

References

[27] F. Bloch, "Bremsvermögen von Atomen mit Mehreren Elektronen", Zeitschrift fü Physik **81**, 363–376 (1933).

[48] M. U. Bug, E. Gargioni, H. Nettelbeck, W. Y. Baek, G. Hilgers, A. B. Rosenfeld, and H. Rabus, "Ionizaion cross section data of nitrogen, methane, and propane for light ions and electrons and their suitability for use in track structure simulation", Phys. Rev. E **88**, 043308 (2013).

[49] H. Tawara, "Some Electron Detachment Data for H^- Ions in Collisions with Electrons, Ions, Atoms and Molecules", Research Report NIFS-DATA Series **ISSN 0915–6364** (1990).

[50] D. Raparia, J. Alessi, G. Atoian, and A. Zelenski, "Charge neutralized low energy beam transport at Brookhaven 200 Mev linac", Rev. Sci. Instrum. **87**, 02B935 (2016).

[51] S. K. Allison, "Experimental Results on Charge-Changing Collisions of Hydrogen and Helium Atoms and Ions at Kinetic Energies above 0.2 kev", Rev. Mod. Phys. **30**, 1137–1168 (1958).

[52] J. Sherman, E. Pitcher, R. Stevens, and P. Allison, "H^- beam neutralization measurements in a solenoidal beam transport system", AIP Conference Proceedings **287**, 686–694 (1992).

[53] S. V. Dudin, A. V. Zykov, and V. I. Farenik, "Low-energy ion beam space-charge neutralization", Review of Scientific Instruments **65**, 1451–1453 (1994).

[54] R. Ferdinand, J. Sherman, R. Jr, and T. Zaugg, "Space-charge neutralization measurement of a 75-keV, 130-mA hydrogen-ion beam", **3**, 2723–2725 vol.3 (1997).

[55] A. B. Ismail, R. Duperrier, D. Uriot, and N. Pichoff, "Space charge neutralization and its dynamic effects", in *Proceedings of HB2006*, (Tsukuba, Japa, 2006), WEAX03.

[56] M. Chung, L. Prost, and V. Shiltsev, in *Proceedings of PAC2013*, (Pasadena, CA, USA, 2013), TUOBB1.

[57] A. Misra, A. Goswami, P. S. Babu, S. Srivastava, and V. S. Pandit., "Studies on space charge neutralization and emittance measurement of beam from microwave ion source", Review of Scientific Instruments **86**, 113301 (2015).

[58] S. Artikova, A. Takagi, T. Shibata, and K. Ikegami, in *Proceedings of the International Particle Accelerator Conference IPAC2016*, (Busan, Korea, 2016), MOPOR035.

[59] S. X. Peng, A. L. Zhang, H. T. Ren, T. Zhang, J. F. Zhang, Y. Xu, J. M. Wen, W. B. Wu, Z. Y. Guo, and J. E. Chen, "Study on space charge compensation of low energy high intensity ion beam in Peking university", in *Proceedings of HB2016*, (Malmö, Sweden, 2016), WEPM6Y01.

[60] L. Prost, J. P. Carneiro, and A. Shemyakin, "Low emittance growth in a low energy beam transport line with un-neutralized section", Phys. Rev. Accel. Beams **21**, 020101 (2018).

[61] J. Qiang, R. D. Ryne, S. Habib, and V. Decyk, "An Object-Oriented Parallel Particle-in-Cell Code for Beam Dynamics Simulation in Linear Accelerators", Journal of Computational Physics **163**, 434–451 (2000).

[62] J. Qiang, "IMPACT-T User Document Beta Version 2.0", LBNL-62326 (2018).

[63] *IMPACT-Z*, `https://amac.lbl.gov/~jiqiang/IMPACT/`.

Chapter 8

Application of GSM: Time-Evolution Measurement of Beam Profile

In Chapters 4-7, the effectiveness of the developed gas sheet monitor was demonstrated. In this chapter, the gas sheet monitor is applied to investigate the time evolution of a beam profile by utilizing the possibility of the 2-D profile measurement and the linearity in signal intensity against a beam pulse length. The signal intensity measured with the wire-scanner monitor which is the ordinary profile monitor depends on a pulse length because the wire warms up by the heat load and the detection sensitivity affected by the secondary electron emission coefficient changes in a beam pulse [6].

8.1 Motivation to measure time evolution of beam profile

In a high-intensity or high-luminosity particle accelerator, the beam loading effect inducing a beam instability is a significant problem [64–67]. When the beam is accelerated in a cavity such as an RFQ, the beam induces an electromagnetic field on the cavity wall (vane) as shown in Fig. 8.1. The wakefield weakens the acceleration electric field of the cavity, and the beam is not accelerated as designed. Since the cavity structure is designed by considering the increment of the beam velocity in the cavity, the beam becomes unstable. To cancel the wakefield, the feed-back and feed-forward controls are employed. The feed-back control system makes the intensity of the electric field

to be a reference intensity. The feed-forward control system adds an electric field of table data prepared in advance and needs to be optimized for the time structure of the beam. Since the feed-back control cannot compensate the wakefield immediately and it is not easy to optimize the feed-forward control for each beam bunch, understanding the beam instability due to the beam loading effect is important. The influence of the beam loading effect on the beam profile is investigated with the gas sheet monitor.

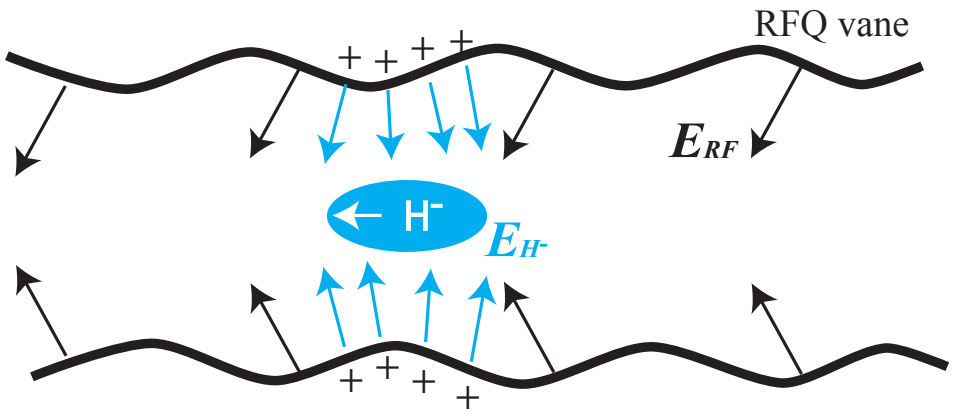

Figure 8.1: A beam induces an electromagnetic field on the cavity vane, and the wakefield weakens the acceleration electric field. The beam is not accelerated as designed, and the beam becomes unstable: the beam loading effect.

8.2 Measurement result

To investigate the time evolution of the beam profile, the exact reconstruction method with the approximation ignoring the point-spread effects described in Chapter 6.2.5 was employed and the basis function was more simplified because a lot of profiles should be reconstructed. The basis function of the y profile is defined as a Gaussian:

$$F(y;\boldsymbol{p}(\mu)) = p_0(\mu)\exp\left(-\frac{(y-p_1(\mu))^2}{2p_2(\mu)}\right) + p_4(\mu) \tag{8.1}$$

where p_1, p_2, p_3, p_4 are the optimization parameters. The optimization process was terminated with $T_h = 10^{-3}$.

Figure 8.2 shows the time evolution of the two-dimensional beam profile in 50 μs of the beam-pules length with/without the feed-forward control. The time-evolution measurement was realized by 1 μs image-intensifier gate width and changing the gate delay timing. Each profile was measured by 200 s CCD camera exposure time and the 15-frame averaging. The gas-sheet-generator inlet pressure was 100 Pa. The residual of the profile reconstruction analysis and the standard deviation on the measurements of both the beam profile and the response function are ranged from 8.4% to 12% in total. The beam profile changes depending on the time, and the feed-forward control affects the beam profile, particularly in 5-20 μs. To discuss these results more quantitatively, the variations of the center-of-mass positions of the beam, the root mean square (RMS) values of the beam profile, and the beam current against time with/without the feed-forward control are shown in Fig. 8.3. The center-of-mass position is calculated from the reconstructed profile, and the beam current is estimated by integrating the intensity of the beam profile in the x-y plane. The RMS values in the x and y directions with the feed-forward control change in the first 10 μs and are almost constant after the 10 μs while the RMS values without the feed-forward control change in the first 30 μs; the feed-forward control system compensates the beam loading effect. Since the beam sizes with/without the feed-forward control agree after the first 30 μs, the feed-back control takes 30 μs to make the beam stable. The beam center positions are also affected by the feed-forward control, and the position in x direction becomes stable with the feed-forward control. On the other hand, the beam current does not affected by the feed-forward control. These results imply that the beam loading effect directly changes the beam profile not via a current reduction. The profile change in the first 10 μs is considered to be induced by some reasons: the feed-forward control which is not

well optimized for the entire beam pulse length, the change of the space-charge force including the space-charge neutralization effect, and the change of the condition in the ion source due to the high-current beam extraction.

In conclusion, it is clarified that the gas sheet monitor can measure the time-evolution of the beam profile, the beam position, and the beam current, and the beam-loading effect has an influence on the beam profile. The gas sheet monitor will serve to measure the beam profile for understanding the details of the instability due to the beam-loading effect.

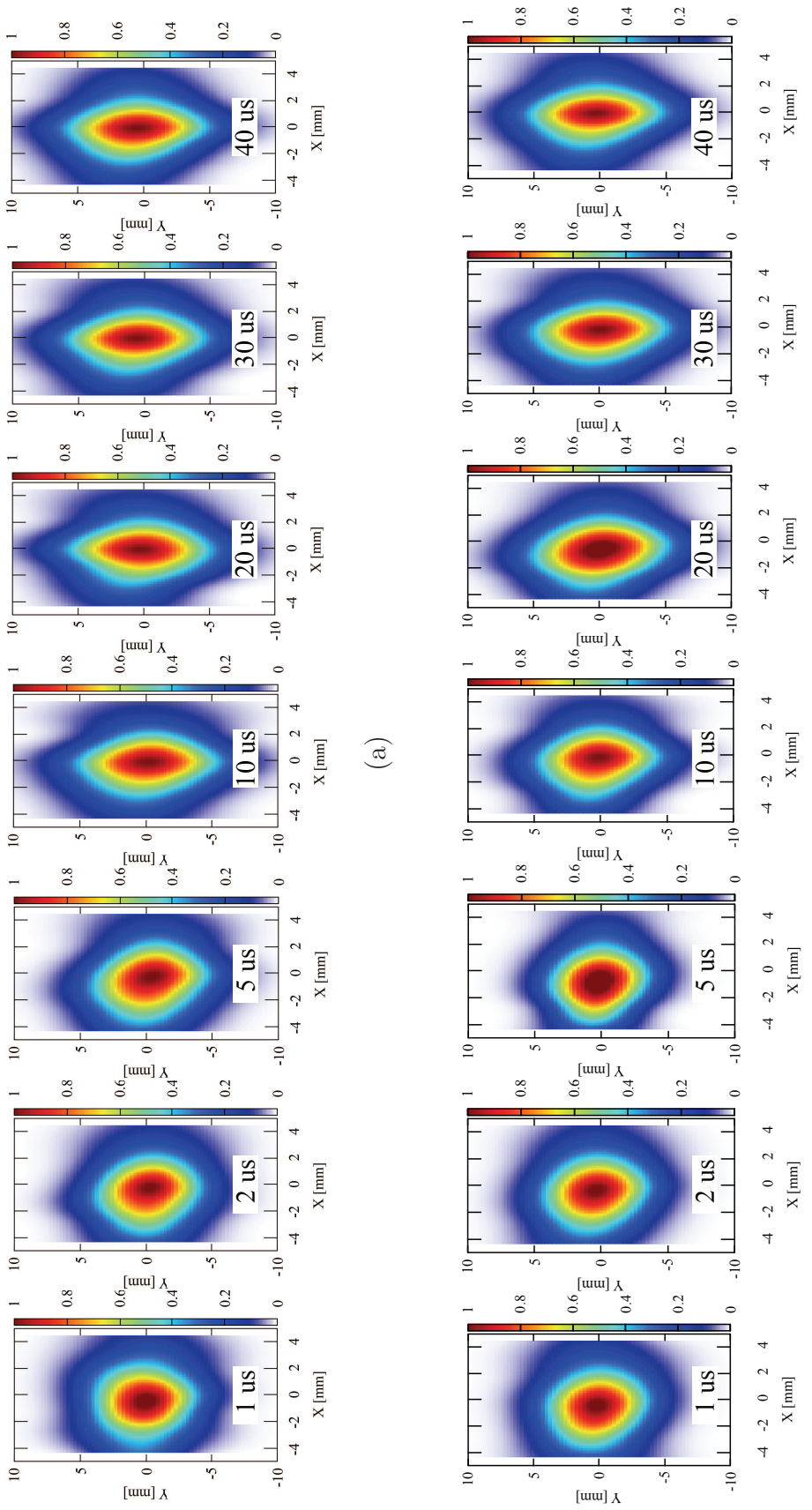

Figure 8.2: The time evolution of the 2-D beam profile (a) with the feed-forward control of the RFQ and (b) without the feed-forward control.

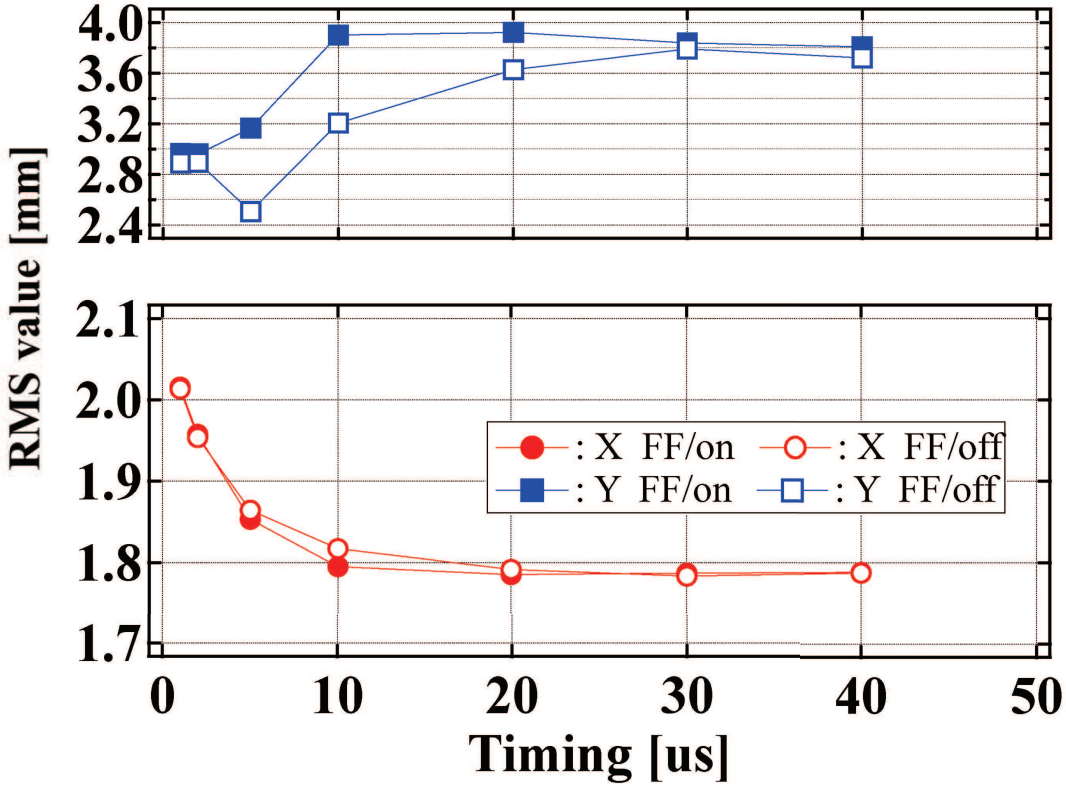
RMS value [mm]
4.0
3.6
3.2
2.8
2.4
2.1
2.0
1.9
1.8
1.7
: X FF/on
: X FF/off
: Y FF/on
: Y FF/off
0
10
20
30
40
50
Timing [us]

(a)

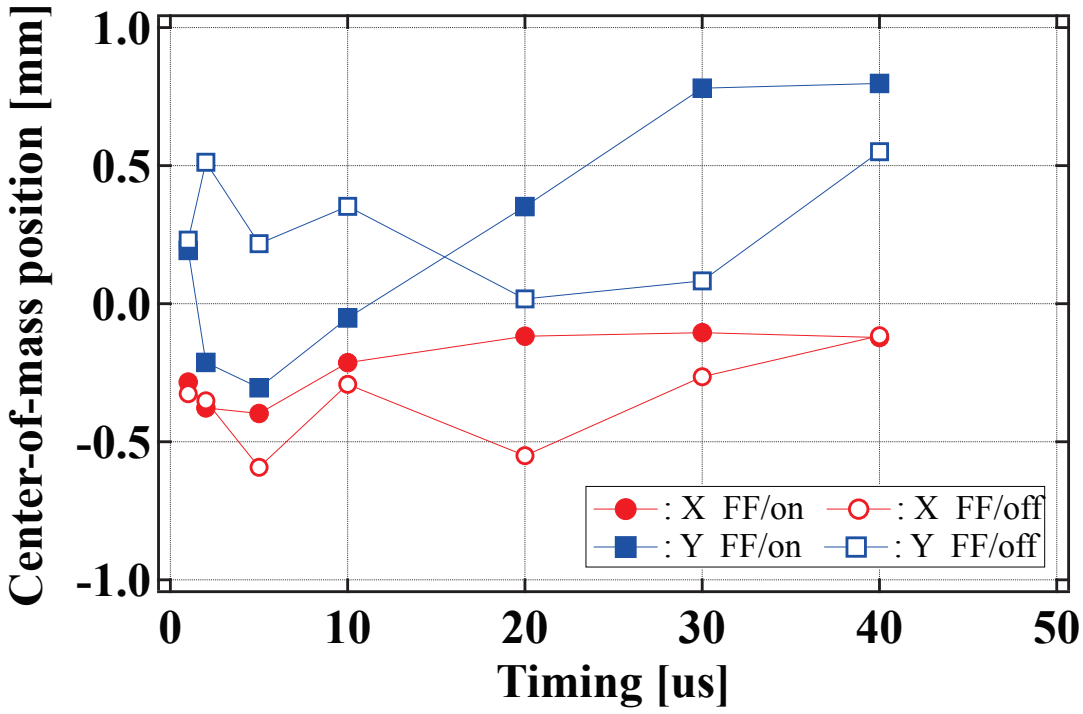
Center-of-mass position [mm]
1.0
0.5
0.0
-0.5
-1.0
: X FF/on
: X FF/off
: Y FF/on
: Y FF/off
0
10
20
30
40
50
Timing [us]

(b)

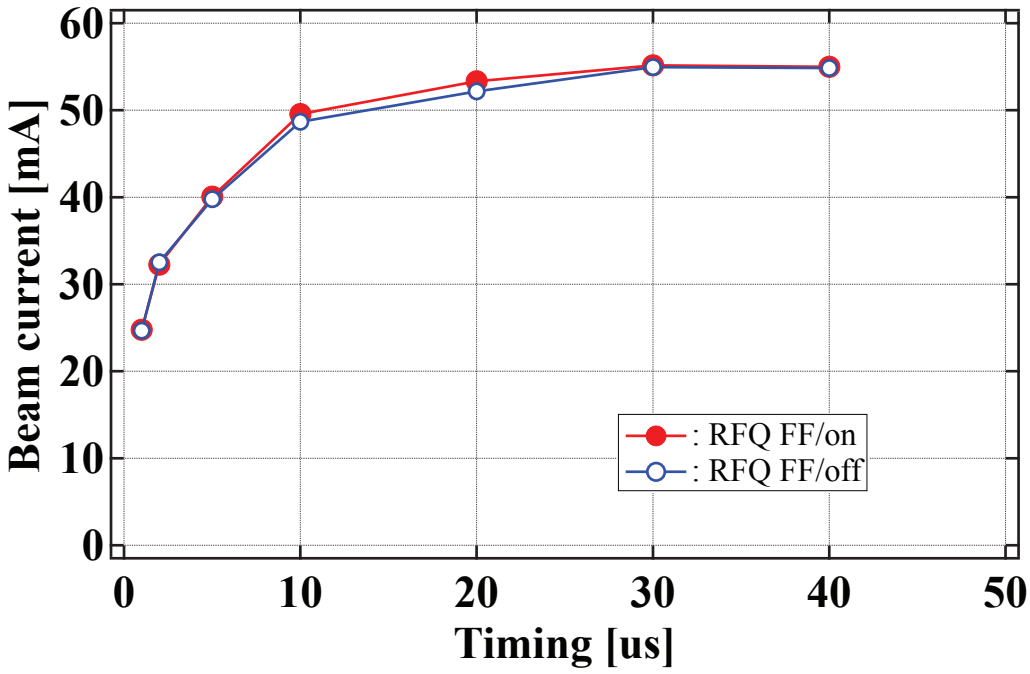

(c)

Figure 8.3: The time evolution of (a) the root-mean-square values of the x and y projected profiles, (b) the center-of-mass positions in X-Y plane, and (c) the beam currents with/without the feed-forward control.

References

[6] A. Miura, K. Hasegawa, T. Miyao, T. Maruta, Y. Liu, and K. Horioka, "Beam profile monitor for intense, negative hydrogen-ion beams in the J-PARC Linac", Journal of the Korean Physical Society **69**, 1005–1013 (2016).

[64] F. Tamura, C. Ohmori, M. Yamamoto, M. Yoshii, A. Schnase, M. Nomura, M. Toda, T. Shimada, K. Hasegawa, and K. Hara, "Commissioning of beam loading compensation system in the J-PARC MR", in *Proceedings of the International Particle Accelerator Conference IPAC2013*, (Shanghai, China, 2013), WEPB16.

[65] M. Kuriki, T. Kakita, S. Kashiwagi, K. Negishi, T. Okugi, T. Omori, M. Satoh, Y. Seimiya, J. Urakawa, K. Yokoya, and T. Takahashi, "Electron Driven ILC Positron Source with a Low Gradient Capture Linac", Proc. of Linear Accelerator Conference (LINAC'16), East Lansing, MI, USA, 25-30 September 2016, TUPRC008 (2017).

[66] S. Li, Z. Fang, K. Futatsukawa, F. Qiu, Y. Fukui, S. Shinozaki, and Y. Sato, "Iterative learning control-based adaptive beam loading compensation implementations in the J-PARC LINAC", Nuclear Instruments and Methods in Physics Research Section A: Accelerators, Spectrometers, Detectors and Associated Equipment **945**, 162612 (2019).

[67] S. Igarashi, K. Satou, C. Ohmori, Y. Arakaki, M. Furusawa, K. Hara, K. Hasegawa, Y. Hashimoto, Y. Hori, H. Hotchi, K. Ishii, K. Kadowaki, N. Kamikubota, T. Kimura, A. Kobayashi, T. Koseki, C. Kubota, Y. Kurimoto, N. Matsumoto, K. Miura, Y. Morita, S. Murasugi, R. Muto, F. Naito, T. Nakamura, K. Niki, M. Nomura, K. Ohmi, M. Okada, K. Okamura, T. Oogoe, A. Orii, K. Sato, Y. Sato, Y. Sato, T. Shibata, T. Shimada, M. Shimamoto, T. Shimogawa, M. Shirakata, T. Sugimoto, Y. Sugiyama, J. Takano, Y. Takiyama, F. Tamura, M. Tejima, M. Tomizawa, T. Toyama, M. Uota, S. Yamada, M. Yamamoto, N. Yamamoto, E. Yanaoka, and M. Yoshii, "Accelerator design for 1.3-MW beam power operation of the J-PARC Main Ring", Progress of Theoretical and Experimental Physics **2021** (2021) 10.1093/ptep/ptab011.

Chapter 9

Conclusion

This dissertation describes development of the non-destructive beam profile monitor using a gas sheet, evaluation of the gas sheet monitor, reconstruction of the beam profile from the obtained data with the gas sheet monitor, influence of the gas sheet injection on the beam, and applied profile measurement. The conclusion of each chapter is presented as follows.

Chapter 1 described the issues of the present beam profile monitor system. The wire-scanning type destructive beam profile monitor cannot be utilized for a high-intensity, low-energy beam because the energy deposition from the beam breaks the wire. To solve the issue, non-destructive beam profile monitors based on beam-gas interaction have been developed in many institutes. However, a proper analysis method to reconstruct a beam profile from the obtained data has not been well established. The non-destructiveness of the gas-injection-type monitor also has not been well investigated in the previous studies. To establish the non-destructive beam profile diagnostic method by clarifying them, the gas sheet monitor has been developed and tested with the J-PARC RFQ test stand high-intensity, low energy H^- beam.

Chapter 2 described the principles of the gas sheet formation and the beam profile measurement with the gas sheet monitor. The gas sheet formation method was presented based on the Boltzmann (or Kinetic) equation. To form a gas sheet, creation of a collisionless condition and shaping a velocity-distribution function were the key points. This study realized them based on vacuum engineering or rarefied gas dynamics. There are two important characteristics in rarefied gas dynamics; the collisionless condition is satisfied from the definition of the rarefied gas dynamics and the reflection angle on a wall is determined by being subject to the cosine law. According to the Boltzmann equation with the collisionless condition, change of the velocity-distribution function

was realized by reflection on a wall or passing through a slit.

As for the principle of the beam profile measurement, the process from photon signal production to construct an image was clarified and formulated. The signal conversion process includes the three kinds of the point-spread effects due to the motion of excited molecules, the out-of-focus effect of the optical lens, and the spatial resolution reduction in the image intensifier. These effects can be described by change of coordinate with integrals. The correlation between the beam profile and the luminous intensity distribution of the obtained image on the CCD camera was devised as a triple-integral equation with the response function describing the gas sheet monitor.

Chapter 3 described design of the gas sheet monitor, particularly the gas sheet generator. To design the gas sheet generator, the Boltzmann equation optimized for molecular flow region was solved by a Monte-Carlo simulation code with the boundary condition of the cosine law. The simulation results indicated that a thin and wide conduit was effective to create a thin gas sheet. The gas sheet monitor was designed to be installed into the J-PARC 3 MeV H^- beam line of the RFQ test stand which is suitable to demonstrate the effectiveness of a non-destructive monitor. From the spatial restriction of the beam line, the conduit width was determined as 50 mm. The length and the thickness were determined as 100 mm and 0.1 mm according to the simulation results. The gas density distribution estimation indicated that the pump having a pumping speed of 1000 ℓ/s was needed to reduce the background gas pressure. In addition, to make a higher contrast between the peak density and the background density, the cover chamber with the slit and the pump was designed. The cover chamber reduced the gas flux injected into the beam line by 72% in the simulation. To test the developed gas sheet generator including the cover chamber and the vacuum systems, the characteristics of the gas pressures, the gas fluxes, and the conductance against the generator inlet pressure were measured. While the measured injection gas flux agreed well with the simulation, the gas flux ratio of the flux evacuated at the cover chamber to the injection flux differed from the estimated one and had the dependance on the inlet pressure. The conductance had the strong dependance on the wide range of the inlet pressure. From these results, it was clarified that the intermolecular collisions is not negligible for the developed generator in the operational pressure range and the important parameter to determine the collisionless region is the conduit length.

Chapter 4 described the method and the results of the response function measurement to reconstruct a beam profile. The response function measurement method by applying a delta-function-like pencil beam into the gas sheet monitor was devised

based on the integral equation describing the profile measurement principle. The response function was measured by scanning the position of the 3 keV electron beam at the off-line setup. In addition, the gas density spatial distribution along the thickness direction was measured by applying the response function measurement method. The gas density distribution became broad against increase of the generator inlet pressure, and it was consistent with the conductance measurement described in Chapter 3.

Chapter 5 described the 3 MeV, 60 mA H^- beam profile measurement at the J-PARC RFQ test stand. The beam-induced photon signal was successfully obtained with the developed gas sheet monitor. The gas sheet monitor has the two parameters for profile measurement: the inlet gas pressure and the averaging time. The beam profiles were measured at the inlet pressure range from 0.1 Pa to 1 kPa. At 1 kPa injection, the beam profile can be recognized from the image captured with only 1 pulse of 50 μs. On the basis of these results, the gas sheet monitor has wide range parameters and can be utilized for the profile measurement of various purposes: a constant monitoring with 0.1 Pa injection or a pulse-by-pulse measurement with 1 kPa injection which cannot be realized with a wire-scanner monitor.

Chapter 6 described the two methods to reconstruct the beam profile from the obtained 2-D image: the simplified method and the exact method. The simplified method assumes the response function as the ideal gas sheet described as a delta function, and the integral equation can be simplified as just the change of coordinate. The error in the reconstructed profile due to ignoring the response function was evaluated, and it indicated that the reconstructed profile is 24% broader than the real beam profile in the y direction. The H^- beam profile was reconstructed and compared with the one measured by the wire-scanner monitor. The difference in the y direction between them was consistent with the estimation, and the difference in the x direction indicated that the point-spread effects cannot be ignored. On the other hand, the exact method takes the response function measured in Chapter 4 into account and solves the integral equation to reconstruct the beam profile. In this exact reconstruction method, the accuracy of the response function measurement affects the reconstructed profile. The error estimation based on assumptions of analytical functions indicated that a thick electron beam makes the reconstructed profile thin as compared with the real one. The reconstructed profile against the high-intensity H^- beam measurement was thinner than the profile measured with the wire-scanner monitor in the x directions as expected. Since the error is caused by utilizing the wrong point-spread effects, the approximation ignoring the point-spread effects was performed. The approximation improved the error

and reconstructed the profile consistent with the one obtained with the wire-scanner monitor. In the y direction, they almost agreed because the error caused by the thick electron beam is small and the error canceled out with the expansion effect due to the restriction of the response function measurement area. Thus, it was demonstrated that the two kinds of the profile reconstruction method can give a beam profile within the possible error range. The methods to improve the reconstruction accuracy without the approximation were also proposed and will be described as the future works at the end of this chapter.

Chapter 7 described the destructiveness evaluation of the gas sheet monitor. The gas sheet monitor is one of non-destructive monitors but the gas sheet injection may affect the beam due to interaction with the extra gas. To evaluate the destructiveness, the electron stripping ratio of the H^- beam and change of the phase space distribution were measured. The electron stripping ratio defined as a beam current reduction linearly increased against a rise in the gas sheet flux. This result was consistent with the theoretical estimation based on the electron stripping cross section. As for change of the phase space distribution, the gas sheet injection decreased the beam emittance. The emittance reduction means an improvement of the beam quality and was explained by the space-charge neutralization effect. Thus, the gas sheet injection does not always have an adverse influence on the beam, and a new advantage of the photon-detection-based profile measurement was found.

Chapter 8 described the applied beam profile measurement with the gas sheet monitor. The time evolution of the beam profile was measured to investigate the beam-loading effect which is the significant problem making the beam unstable in a high-intensity particle accelerator. It was clarified that the gas sheet monitor can measure the time evolution of the beam profile in a beam pulse and the beam-loading effect affects the beam profile and makes the beam profile unstable.

In conclusion, this study contributes to establish the non-destructive beam profile diagnostic method by demonstrations that the gas sheet monitor designed based on rarefied gas dynamics can measure a high-intensity beam profile with beam-induced photons, the two kinds of the proper analysis methods and the response function measurement method can reconstruct the profile from the obtained image, and the gas sheet injection reduces the beam current and mitigates the beam emittance growth. The gas sheet monitor will serve as a non-destructive beam profile monitor for a future high intensity particle accelerator.

Lastly, the three future works are described as follows. The first one is gas sheet

generator improvement. The gas sheet generator was designed based on rarefied gas dynamics, but the experimental results indicated that the effect of the intermolecular collisions is not negligible in the main gas pressure region to be utilized for the gas sheet monitor. The gas sheet spatial distribution was broad as compared with the gas flow simulation. The gas sheet thickness induces the error in the reconstructed profile with the simplified method. Therefore, a new gas sheet generator should be designed through taking into account of the intermolecular collisions, or a sheet generator having a wide fully-collisionless pressure region which depends on the conduit length should be developed.

As for the profile reconstruction accuracy, the gas sheet thickness affects the accuracy of profile reconstruction with the simplified method, and the electron beam affects the one with the exact method. The improvement of the gas sheet is discussed above. To improve the accuracy of the exact reconstruction method, an electron beam source producing an enough thin beam which satisfies the condition clarified in Chapter 6 should be developed. As another plan, solving the principle equation of the response function measurement and reconstructing the accurate response function are the best way to establish the profile analysis method because this plan realizes the accurate reconstruction independent of the electron beam profile.

The detail mechanism of beam-gas interaction should be clarified to understanding and improving the gas sheet monitor. As describe in Chapter 7, the gas sheet monitor reduced the beam emittance through beam-gas interaction; the gas sheet monitor can be equipped with the beam cooling function. This function can be realized only when the profile is detected with photons, and will be a strong advantage of the gas sheet monitor as compared with the other profile monitors.

Acknowledgement

First and foremost, I would like to express my gratitude to my advisor Prof. Motoi Wada for his excellent support. He taught me the interest of the plasma physics and its experiments. He always understood my situation and gave me pertinent comments and suggestions. When the experiments did not go well, he encouraged me. I would also like to thank Prof. Toshiro Kasuya for the valuable advices. He also taught me the interest of the theoretical and numerical plasma physics, especially space plasma. The reason I entered Plasma Physics Laboratory was to study space plasma physics, and the motivation still exists.

I am grateful to Prof. Mamiko Sasao of Tohoku University, Dr. Hitoshi Yamaoka of RIKEN SPring-8 center, Dr. Nozomi Tanaka of Osaka University, and Dr. Kengo Moribayashi of National Institute for Quantum Science and Technology for the valuable discussions. I would like to give my thank to Dr. Yuji Shimabukuro, who invited me to the doctoral course, Keisuke Hida, Yuki Hosomi, Kenta Imamura, Nobufumi Nishina, and all the members of Plasma Physics Laboratory for worthwhile casual discussions.

I would like to thank Dr. Michikazu Kinsho, Dr. Junichiro Kamiya, and Dr. Norio Ogiwara for giving this interesting study theme. I would also like to thank Dr. Kazami Yamamoto and all the members of Accelerator division of J-PARC center for giving not only the various advices and comments but also the machine time of J-PARC beam line and the RFQ test stand beam line which are the excellent accelerators. I appreciates the student research fellowship system and the financial support of Japan Atomic Energy Agency.

I would like to thank Motoki Chimura of Tohoku University for giving the PIC simulation analysis of the beam dynamics.

Lastly my deepest gratitude goes to my mother and father for the support and encouragement for 27 years.

Publications

Papers

1. I. Yamada, N. Ogiwara, Y. Hikichi, J. Kamiya, and M. Kinsho, "Development of a Gas Distribution Measuring System for a Two-dimensional Beam Profile Monitor with a Sheet-Shaped Gas", *Proceedings of 15th Annual Meeting of Particle Accelerator Society of Japan, Aug. 7-10, Nagaoka, Japan*, **THOO11**, (2018).

2. I. Yamada, N. Ogiwara, Y. Hikichi, J. Kamiya, and M. Kinsho, "Development of a Gas Distribution Measuring System for 2-D Beam Profile Monitor", *Journal of Vacuum and Surface Science*, **62**, 7(2019). doi: 10.1380/vss.62.400.

3. I. Yamada, N. Ogiwara, Y. Hikichi, J. Kamiya, and M. Kinsho, "Development of a Gas Distribution Measuring System for a Gas Sheet Beam Profile Monitor", *Proceedings of the International Particle Accelerator Conference 2019, Melbourne, Australia*, **WEPEG041**, (2019). doi: 10.18429/JACoW-IPAC2019-WEPGW041.

4. N. Ogiwara, Y. Hori, I. Yamada, Y. Hikichi, J. Kamiya, and M. Kinsho, "Development of a Dense Gas Sheet Target for a 2D Beam Profile Monitor", *Proceedings of the International Particle Accelerator Conference 2019, Melbourne, Australia*, **WEPEG037**, (2019). doi: 10.18429/JACoW-IPAC2019-WEPGW037.

5. J. Kamiya, K. Okabe, M. Kinsho, K. Moriya, I. Yamada, N. Ogiwara, Y. Hikichi, and K. Wada, "Performance Verification of 2-D Transverse Beam Profile Monitor using Gas Sheet at J-PARC LINAC", *Journal of Physics: Conference Series*, **1350**, 012149(2019). doi: 10.1088/1742-6596/1350/1/012149.

6. I. Yamada, J. Kamiya, M. Kinsho, and M. Wada, "Measurement of Relative Sensitivity Distribution for Gas Sheet Beam Profile Monitor", *Proceedings of 17th Annual Meeting of Particle Accelerator Society of Japan, Sep. 2-4, 2020, Online*, **THOO11**, (2020).

7. I. Yamada, M. Wada, K. Moriya, J. Kamiya, P. K. Saha, and M. Kinsho, "High-intensity beam profile measurement using a gas sheet monitor by beam induced fluorescence detection", *Physical Review Accelerators and Beams*, **24**, 042801(2021). doi: 10.1103/PhysRevAccelBeams.24.042801.

8. I. Yamada, M. Wada, K. Moriya, J. Kamiya, and M. Kinsho, "Measurement and reconstruction of a beam profile using a gas sheet monitor by beam-induced fluorescence detection in J-PARC", *Proceedings of 10th International Beam Instrumentation Conference, Sep. 13-17, Online*, **TUOA04**, (2021). doi: 10.18429/JACoW-IBIC2021-TUOA04.

9. I. Yamada, M. Wada, J. Kamiya, and M. Kinsho, "Non-destructive beam spatial profile measurement using a gas sheet monitor for a high-intensity ion beam", *Journal of Physics: Conference Series*, **accepted** (2021).

International conferences and workshops

1. I. Yamada, N. Ogiwara, Y. Hikichi, J. Kamiya, and M. Kinsho, "Development of a Gas Distribution Measuring System for 2-D Beam Profile Monitor Using a Gas Sheet", International workshop on non-invasive beam profile monitors for hadron machines and its related techniques: 3rd IPM workshop, Ibaraki, Japan, Sep. 2018.

2. I. Yamada, N. Ogiwara, Y. Hikichi, J. Kamiya, and M. Kinsho, "Development of a Gas Distribution Measuring System for 2-D Beam Profile Monitor" 10th International Particle Accelerator Conference, Melbourne, Australia, May 2019, WEPEG041.

3. J. Kamiya, K. Okabe, M. Kinsho, K. Moriya, I. Yamada, N. Ogiwara, Y. Hikichi, and K. Wada, "Performance Verification of 2-D Transverse Beam Profile Monitor using Gas Sheet at J-PARC LINAC", 10th International Particle Accelerator Conference, Melbourne, Australia, May 2019, WEPEG032.

4. N. Ogiwara, Y. Hori, I. Yamada, Y. Hikichi, J. Kamiya, and M. Kinsho, "Development of a Dense Gas Sheet Target for a 2D Beam Profile Monitor", 10th International Particle Accelerator Conference, Melbourne, Australia, May 2019, WEPEG037.

5. I. Yamada, M. Wada, K. Moriya, J. Kamiya, and M. Kinsho, “Measurement and reconstruction of a beam profile using a gas sheet monitor by beam-induced fluorescence detection in J-PARC”, 10th International Beam Instrumentation Conference, Online, TUOA04, Sep. 2021.

6. I. Yamada, M. Wada, J. Kamiya, and M. Kinsho, “Non-destructive beam spatial profile measurement using a gas sheet monitor for a high-intensity ion beam”, 19th International Conference on Ion Sources, #048, Online, Sep. 20-24, 2021.
   => Student Poster Award

7. I. Yamada, M. Wada, J. Kamiya, and M. Kinsho, ”Non-destructive 2-D beam profile measurement using a gas sheet by fluorescence detection”, The 7th IFMIF workshop: beam diagnostics and beam controls, online, Invited oral, Mar. 2022.

Domestic conferences and workshops

1. I. Yamada, N. Ogiwara, Y. Hikichi, J. Kamiya, and M. Kinsho, “Development of a Gas Distribution Measurement System for a Two-dimensional Beam Profile Monitor with a Sheet-Shaped Gas”, Annual Meeting of Particle Accelerator Society of Japan, Aug. 7-10, 2018, Nagaoka, Japan, THOO11.

2. I. Yamada, N. Ogiwara, Y. Hikichi, J. Kamiya, and M. Kinsho, “Development of a Gas Distribution Measuring System for 2-D Beam Profile Monitor”, Annual Meeting of The Japan Society of Vacuum and Surface Science 2018, Nov. 19-21, 2018, Kobe, Japan, 2Cp05S.

3. I. Yamada, N. Ogiwara, Y. Hikichi, J. Kamiya, M. Kinsho, and M. Wada, “Development of a Gas Distribution Measuring System for 2-D Beam Profile Monitor”, Annual Meeting of Young Researchers Association of the Japan Beam Physics Club, Nov. 22, 2018, Chiba, Japan.
   => Presentation Award

4. I. Yamada, N. Ogiwara, Y. Hikichi, J. Kamiya, and M. Kinsho, “Development of a Gas Distribution Measuring System for Gas Sheet Profile Monitor”, The Physical Society of Japan 2019 Annual (74th) Meeting, Mar. 14-17, 2019, Fukuoka, Japan, 16pG107-10.

5. I. Yamada, N. Ogiwara, Y. Hikichi, J. Kamiya, M. Kinsho, and M. Wada, “Development of a Non-destructive Beam Profile Monitor for a High Intensity Ion Beam”, The 80th the Japan Society of Applied Physics Autumn Meeting, Sep. 18-21, 2019, Sapporo, Japan, 17a14D-5.

6. I. Yamada, N. Ogiwara, J. Kamiya, and M. Kinsho, “Gas Density Distribution Measurement for a Non-invasive Beam Profile Monitor”, The Physical Society of Japan 2020 Annual (75th) Meeting, Mar. 14-17, 2020, Online, 16pG107-10.

7. I. Yamada, J. Kamiya, M. Kinsho, and M. Wada, “Measurement of Relative Sensitivity Distribution for Gas Sheet Beam Profile Monitor”, 17th Annual Meeting of Particle Accelerator Society of Japan, Sep. 2-4, 2020, Online, THOO11.

8. I. Yamada, ”Beam profile measurement using a sheet-shaped gas”, Meeting of The Kanto Chapter of the Japan Society of Vacuum and Surface Science, Apr. 3, 2021, Online, Invited oral.

9. I. Yamada, M. Wada, J. Kamiya, and M. Kinsho, “Non-destructive beam profile diagnostic based on beam-induced fluorescence using a gas sheet”, Annual Meeting of the Japan Society of Vacuum and Surface Science 2021, Nov. 3-5, 2021, Online, 1Ep12S.

10. I. Yamada, M. Wada, J. Kamiya, and M. Kinsho, “Non-Destructive High-Intensity-Beam Profile Measurement with a Gas Sheet Monitor”, The Physical Society of Japan 2022 Annual (77th) Meeting, Mar. 15-19, 2022, Online, 15aA124-3.